MASTER

Development and understanding of a plasma-assisted atomic layer deposition process for silicon nitride

Braeken, E.M.J.

Award date:
2013

Technische Universiteit
Eindhoven
University of Technology

Department of Applied Physics
Plasma & Materials Processing

Development and understanding of a plasma-assisted atomic layer deposition process for silicon nitride

E.M.J. Braeken BSc

August 2013 PMP 2013-01

Supervisors:
Dr.ir. H.C.M. Knoops
Dr. S.E. Potts
Prof.dr.ir. W.M.M. Kessels

Abstract

Silicon nitride is a material that is used in a variety of applications, e.g., as a gate spacer, barrier layer or sacrifical layer in microelectronics. Due to the downscaling of semiconductor devices, precise layer thickness control, uniformity, conformality and low deposition temperatures are becoming more important. Plasma-assisted atomic layer deposition (ALD) is a cyclic deposition technique that could meet these requirements.

Therefore, an ALD process for silicon nitride was developed with the metalorganic precursor bis(*t*-butylamino)silane (BTBAS) and a N_2 plasma, since the hydrogen-containing plasmas NH_3 and H_2-N_2 resulted in extremely low growth rates. Saturation curves for this process confirmed the self-limiting behavior characteristic for ALD. The resulting films showed a relatively high carbon content and N/Si ratio. The material properties were optimized by increasing the plasma exposure time, increasing the temperature and decreasing the plasma pressure.

The temperature window that resulted in films with good quality was 200°C-500°C. The refractive index, N/Si ratio and mass density reached values close to those of stoichiometric Si_3N_4 and the carbon and hydrogen contents decreased to ≈ 5 at% each. The uniformity of thickness and refractive index improved with increasing temperature as well. Also, the long-term stability of the films improved and for plasma exposure times ≥ 7.5 seconds, temperatures ≥ 200°C and pressures ≤ 40 mTorr the films showed no signs of oxidation in the two months after they were deposited. ALD behavior was also obtained for a temperature of 100°C, but further optimization of the low-temperature process parameters is needed to improve the material quality under these circumstances.

Quadrupole mass spectrometry and optical emission spectroscopy were employed to provide insight into the reaction mechanism. The main reaction product during the precursor step was the *t*-butylamine ligand of BTBAS and the precursor adsorption on the surface was not limited by steric hindrance. The main reaction products during the plasma step were cyanogen, propane, hydrogen cyanide, ammonia and hydrogen. Since the reaction products in the plasma exposure step contained *t*-butylamine ligand fragments, it was assumed that BTBAS adsorbed monofunctionally during the precursor step by splitting off one *t*-butylamine ligand and that the other *t*-butylamine ligand was removed by the nitrogen plasma.

The effect of hydrogen, when added to the plasma, was investigated to gain insight into the reaction mechanism leading to the reduced GPCs. The hydrogen-containing plasmas were able to remove *t*-butylamine ligands, but poisoned the surface, which limited precursor adsorption in the next cycle, hence reducing the growth. N_2 plasmas could remove the poisoning partly. Three possible reaction mechanisms that could explain the poisoning mechanism have been proposed.

Contents

Chapter 1

Introduction

The focus of this work is on atomic layer deposition (ALD) of silicon nitride. Therefore, the first three sections in this chapter will be used to introduce the applications of silicon nitride and ALD. In the fourth section the project goal and the main research questions will be stated. The last section contains the outline of this work.

1.1 Silicon nitride and its applications

Silicon nitride is a material that is used in a variety of applications, as some examples in figure 1.1 show. In photovoltaics it is used as an antireflection coating and passivation layer, in microelectronics silicon nitride can be used as a gate spacer, barrier layer or sacrificial layer [1–3]. For each application films with different properties are required and these material properties depend on the deposition techniques and conditions.

Due to the downscaling of the 3D structures in semiconductor devices, precise layer thickness control, uniformity and conformality are becoming more and more important. Also, the thermal budget should be reduced. The most common used deposition techniques for silicon nitride (e.g., for gate spacers and encapsulation) are low pressure chemical vapor deposition (LPCVD) and plasma enhanced chemical vapor deposition (PECVD) [4]. LPCVD deposited silicon nitride films need a relatively high deposition temperature ($> 700°C$), although they do result in good conformality, while PECVD films can be deposited at temperatures below 400°C, but generally show poor conformality [4, 5]. Atomic layer deposition (ALD) is a deposition technique that can combine the requirements of very accurate thickness control in 3D structures and a low deposition temperature [4, 6] and will therefore be discussed in more detail in the next section.

Depending on the application, specific requirements of certain material properties can

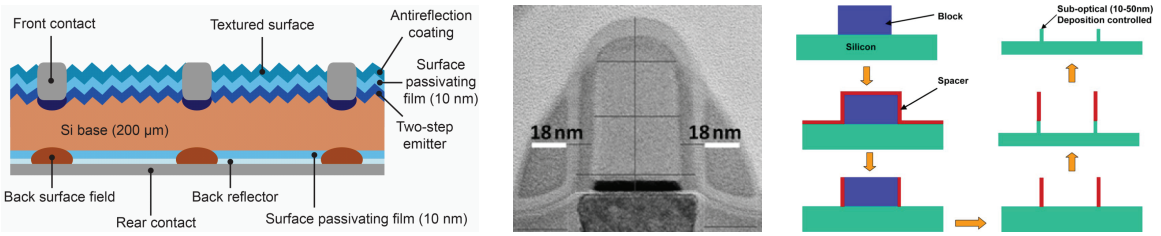

Figure 1.1: Three examples of silicon nitride applications: solar cells (left), gate spacers [4] (center) and as sacrificial spacer layer in spacer defined double patterning [2] (right).

be necessary, for example the ratio between nitrogen and silicon, the refractive index, the maximum impurity content and the mass density. The hydrogen content of the films is also important, since high hydrogen concentrations can degrade the film characteristics and the device performance in microelectronics [7–9], while in solar cells hydrogen can be beneficial by passivating defects [1]. Also, the stability of the deposited films can be an issue. Unstable films can oxidize after deposition, while stable films do not/hardly oxidize after deposition.

1.2 Atomic layer deposition

Atomic layer deposition is a deposition technique that theoretically allows for the deposition of one monolayer per cycle. The key feature of an ALD process is that it consists of two self-limiting half-reactions in one cycle. Each cycle consists of several steps, of which the four most important steps are shown in figure 1.2. During the first half-cycle the precursor is exposed to the surface. It adsorbs on the surface and when all active surface sites are occupied, no more precursor is adsorbed, because it cannot react with itself. After the precursor exposure all remaining precursor molecules and reaction products are removed from the reactor by a purge step. The second half-cycle starts with the reactant exposure. The reactant, which is typically a gas for thermal ALD, replaces or modifies the surface groups. When all surface groups are converted into groups the precursor can adsorb on, the reaction stops, because the reactant cannot react with these modified surface groups. After the reactant exposure, a purge step is used to remove all remaining reactant species and reaction products from the reactor. The surface can then be exposed to the precursor again in the next cycle and these cycles are repeated until the desired film thickness is achieved. Note that the purge steps are necessary to avoid that precursor and reactant species are in the reactor at the same time, which could lead to CVD-like growth.

In plasma-assisted ALD the reactant is a plasma and the merits of plasma-assisted ALD over thermal ALD are the production of more reactive species, improved and controlled material properties, increased choice of precursors and materials, increased GPC, more process versatility and a low thermal budget [6]. The low thermal budget of a plasma-assisted process is due to the fact that a plasma leads to reactive species without requiring thermal equilibrium. Even though the gas temperature is relatively low (300K-500K), the electron temperature can be high (10.000K-50.000K) [6]. The electrons in the tail of the energy distribution can ionize and dissociate the gas-phase molecules, creating reactive species. These reactive species can induce surface reactions, which lead to the deposition of the film.

To ensure the self-limiting behavior of each half-cycle the cycle steps need to be optimized. The growth per cycle (GPC) should be independent of the precursor and reactant dosages. Since saturation is necessary for ALD, the duration of each step must be long enough to achieve this, but the cycle time should be optimized as well to improve throughput. When saturation is achieved, other process parameters can be varied to optimize the film properties (e.g., film composition, refractive index and mass density).

Plasma-assisted ALD can be used to deposit a wide variety of materials, also materials that cannot be deposited with thermal ALD. For many materials, plasma-assisted ALD is a deposition technique that allows for deposition temperatures below the conventional temperature windows provided by thermal ALD or LPCVD. However, the temperature window in which the ALD process exhibits the self-limiting half-reactions can be limited (e.g., due to the decomposition temperature of the precursor). Although plasma-assisted ALD processes generally result in improved material quality, the incorporation of impurities due to non-ideal processing parameters can still be an issue. Therefore, it is important to under-

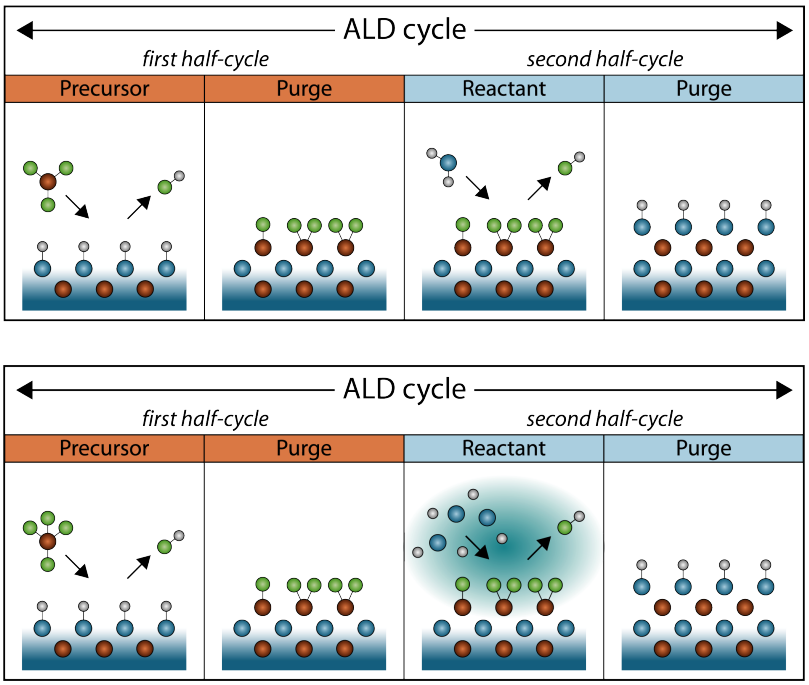

Figure 1.2: A schematic overview of the most important steps in an ALD process. The top figure shows a thermal ALD process and the bottom figure shows a plasma-assisted ALD process.

stand the growth mechanism of the process and the influence of the processing parameters on this mechanism, since variation of processing parameters can be used to tune the material properties.

1.3 Atomic layer deposition of silicon nitride

In the development of a plasma-assisted ALD process the choice of precursor and reactant is important. There are many precursors that can be considered to deposit silicon nitride with ALD, the main types being metal hydride, metal halide and metalorganic precursors. Ammonia, nitrogen or hydrogen-nitrogen can be considered as reactants, either as a gas or as a plasma.

Metal halide precursors ($SiCl_4$, SiH_2Cl_2 or Si_2Cl_6) are mostly reported in the literature and are mainly used in combination with NH_3 gas or plasmas and result in GPCs between 0.9 Å and 2.7 Å [3, 10–13]. The refractive index of these films ranges from 1.6 to 2.01 [3, 10, 12, 13]. The hydrogen content for a film deposited with SiH_2Cl_2 and an NH_3 plasma is 13 at% [11, 13]. A disadvantage of using metal halide precursors is that they can lead to formation of ammonium chloride, which accumulates at/in several reactor parts [5, 14]. Therefore frequent cleaning is required, reducing the available processing time [14].

King reported an ALD process for silane gas and a nitrogen plasma, which resulted in GPCs between 0.25 Å and 2 Å [15]. Plasma exposure times of 60-90 seconds were needed to achieve saturation, leading to relatively long cycle times [15]. The refractive index of the deposited films (1.749) was low compared to the refractive index of stoichiometric Si_3N_4 (2.05) [15, 16]. King reported that the addition of NH_3 to the plasma resulted in a GPC below 0.03 Å and suggested that this is due to the formation of an N−H terminated surface, while SiH_4

adsorption only occurs on nitrogen dangling bonds [15]. This process could be difficult due to the low reactivity of the Si−H bond in silane [17].

Metalorganic precursors do not lead to the formation of ammonium chloride, but the resulting films can contain carbon impurities. ALD processes for metalorganic precursors were reported by Fang *et al.*, but did not result in stable films [18]. In this work the metalorganic precursor bis(*t*-butylamino)silane (BTBAS) was used in combination with an ammonia, nitrogen or hydrogen-nitrogen plasma. The plasma is not only important to remove the precursor ligands remaining on the surface after precursor dosing, but also to prepare the surface for precursor adsorption in the next cycle. Using different plasmas could result in different surface groups, which could be important for silicon nitride growth by ALD.

1.4 Project goal and research questions

As discussed in this chapter, silicon nitride is an interesting material for many applications. Furthermore, thickness control of the sub-nanometer level is becoming more important nowadays and the deposition temperature needs to be reduced to extend the application range of silicon nitride films even further. Therefore, the main goal of this work is *the deposition of high quality silicon nitride with plasma-assisted ALD in a wide temperature window.* To this end, an ALD cycle for silicon nitride was developed in this work and the saturation behavior of this cycle was investigated. To guide the research and provide focus to this work, the following research questions were stated:

- *What is the temperature window in which this ALD process can be used?*
  As stated before, it is important to extend the temperature window for silicon nitride depositions to lower temperatures. At the same time, high temperature applications remain. Therefore, the influence of deposition temperature on the self-limiting behavior and the material properties was investigated.

- *What are the properties of the resulting films and is it possible to control these properties?*
  The influence of the plasma composition and other deposition parameters on the GPC was studied. Films were deposited for varying deposition parameters to investigate whether the material properties could be tuned. The properties studied in this work were the refractive index, film composition, sputter rate, mass density, thickness and refractive index uniformity and stability.

- *What are the reaction products and what are the characteristics of the growth mechanism?*
  Mass spectrometry and optical emission spectroscopy measurements were performed to investigate the reaction products during the process and to provide information about the reaction mechanism.

These questions will be addressed in the following chapters.

1.5 Outline of the thesis

In the next chapter the deposition setup and the diagnostic techniques that were used in this work will be described. The chapters that follow will answer the questions that were stated in the previous section.

Since the temperature window is an important issue for a deposition process, it is important to determine the deposition temperature accurately. Therefore, chapter 3 will address a measurement method for the substrate temperature.

In chapter 4 the development of the plasma-assisted ALD process will be discussed and the material properties will be investigated as a function of several process parameters. The fifth chapter will show systematic experiments to study the growth mechanism of the developed ALD process. Moreover, a growth mechanism will be proposed. In the last chapter the conclusions of this work will be presented.

Chapter 2

Experimental setup and diagnostics

In this chapter a short overview of the experimental setup will be given. The ALD reactor FlexAL2, which is used for the deposition of silicon nitride, will be described in the first section. To provide a better understanding of the ALD process, the second section will explain the various steps in the ALD cycle used in this work. Some diagnostic techniques that were used have already been mentioned in chapter 1. An overview of all the diagnostics used in this work will be given in section 2.3. The basics of these diagnostics and the measurement procedures will be explained.

2.1 The atomic layer deposition tool (FlexAL2)

The deposition of silicon nitride was done in the remote plasma ALD reactor FlexAL2, developed by Oxford Instruments. A schematic of this reactor is shown in figure 2.1. Samples for deposition enter the reactor via a loadlock system. Depositions were done on 2 and 4 inch wafers or pieces thereof. Single side polished wafers could directly be handled by the loadlock system, for double side polished wafers or wafer pieces a carrier wafer had to be used.

The wafer table can be heated up to 500°C, while the maximum wall temperature is 150°C. When the heater in the wafer table is set to a temperature $\geq$ 150°C, the wall temperature is set to 150°C. For heater temperatures below 150°C, the temperature of the walls is set to the same value as the heater temperature.

The temperature of the BTBAS bubbler is set to 50°C and the precursor is introduced by the vapor draw method, where argon can be used as a carrier gas. The temperature of the lines was set to 70°C to avoid precursor condensation in the lines. The precursor was injected below the plasma source.

On top of the reactor chamber the remote plasma source is positioned. The ICP source is controlled by an automatic matching network for an efficient power coupling into the plasma. The input power can be set to a maximum of 600W. In this work the processing gases entered the chamber via the top of the plasma source, but there is also a gas inlet below the plasma source.

The angle of the butterfly valve (above the pumping unit) determines the effective pumping of the reactor. This angle (0°-90°) together with the gas flow determines the pressure in the reactor. To achieve low pressures the valve is opened more than for high pressures. The maximum allowed pressure is 250 mTorr.

There are three *in situ* diagnostics used in this work. The optical windows for spectroscopic ellipsometry are positioned under an angle of 70°. These windows are closed by valves during the deposition to avoid deposition on the windows. The quadrupole mass spec-

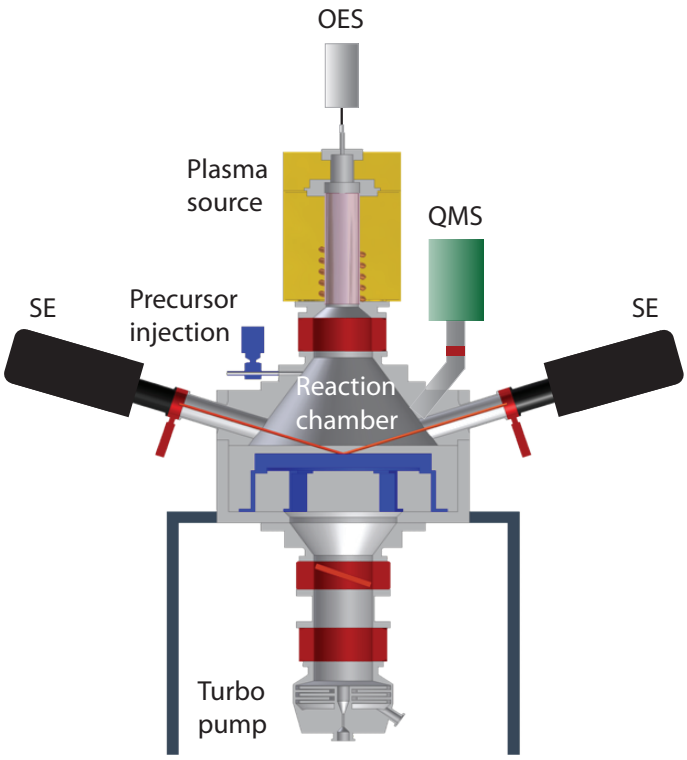

Figure 2.1: A schematic overview of Oxford Instruments' FlexAL2 reactor, showing the main components of the reactor. The valves are depicted in red and the heated substrate holder is shown in blue in the reaction chamber. The ICP source is positioned on top of the reaction chamber, the turbo pump at the bottom of the chamber. The *in situ* diagnostics SE, QMS and OES are depicted as well. The loadlock, precursor pots and precursor delivery lines are not shown.

trometer is also connected to the reaction chamber through a valve and for optical emission spectroscopy a fiber is positioned on top of the plasma source to vertically probe emission from the plasma through a small window.

2.2 The silicon nitride ALD cycle

An ALD process consists of the repetition of a cycle and the basic ALD cycle for silicon nitride in this work consists of seven steps.

1. Pre-dosing: The argon flow through the precursor lines is switched on to clean the precursor delivery lines.
2. Precursor dosing: The bubbler valve is opened and BTBAS is transferred to the reaction chamber. During this step the argon flow is diverted to the exhaust.
3. Reaction step: Because the precursor dosing time is very short, a reaction step is included to allow the precursor to adsorb on the surface. The precursor lines are purged with argon to keep the lines clean. To limit precursor removal from the reactor chamber but allow the removal of reaction products, the butterfly valve is nearly closed by setting the angle to 10°.
4. Precursor purge: The precursor lines are purged with argon and the reaction chamber is pumped down to remove the remaining precursor and reaction products.
5. Pre-plasma: The plasma gases are switched on to guarantee that the flows have stabilized when the plasma is ignited.
6. Plasma: The plasma is ignited.
7. Purge plasma: The reaction chamber is pumped down to remove the remaining plasma species and reaction products.

This cycle is repeated and after a certain number of cycles an SE measurement (see section 2.3.1) is done to determine the thickness of the deposited film. This procedure is repeated until the desired film thickness is deposited.

2.3 Diagnostics

In this section the diagnostic techniques will be described. For each technique a short explanation will be given, followed by the measurement procedure and analysis methods.

2.3.1 Spectroscopic ellipsometry (SE)

Spectroscopic ellipsometry (SE) is a non-invasive optical technique that can be used to obtain information about the film thickness and the optical constants of the film. It measures the change in polarization of a light beam that is reflected off a sample [19].

During an SE measurement the difference in amplitude ratio Ψ and phase difference Δ between the incoming and reflected beam are measured [19, 20], as shown in figure 2.2. Modelling this data correctly can give the thickness and the optical constants (or dielectric function) of the film.

These optical constants can be expressed in terms of the real and imaginary part of the complex refractive index $\tilde{n} = n - ik$, where n is the refractive index and k the extinction coefficient. However, the optical constants can also be expressed in terms of the real (ε_1)

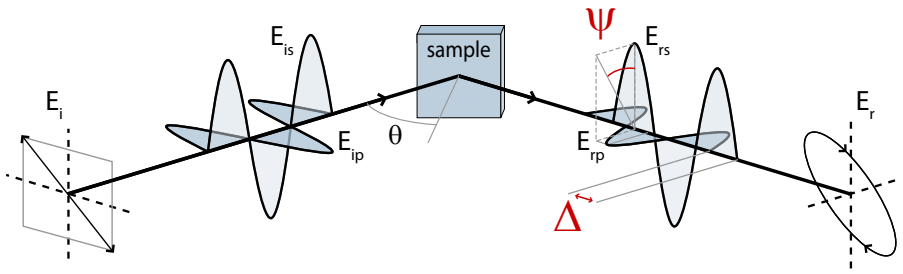

Figure 2.2: The principle of an SE measurement, showing the different orientations of the electric field.

and imaginary (ε_2) part of the complex dielectric function, which are related (to the complex refractive index) via $\varepsilon_1 = n^2 - k^2$ and $\varepsilon_2 = 2nk$. ε_1 and ε_2 must be Kramers-Kronig consistent [20].

The spectrometer used for *in situ* SE measurements was a J.A. Woollam Co., Inc. M-2000F (1.2 eV - 5.0 eV) and the J.A. Woollam Co., Inc. M-2000D spectrometer (1.2 eV - 6.5 eV) was used for *ex situ* SE measurements.

SE measurements

After the sample was loaded into the reaction chamber and the sample temperature had stabilized, the SE was calibrated using a crystalline silicon sample with native oxide on top by employing the model Si Temp JAW (Temp Library) by J.A. Woollam. After the calibration, a single measurement of the substrate was performed and modelled with a temperature dependent model for the silicon substrate. With these data the wafer temperature, the angle offset and the thickness of the native oxide layer were determined. When depositions followed, these values were fixed for the following measurements and the thickness of the deposited layer could be monitored when an additional layer, representing the deposited material, was added to the model. For the temperature tests in chapter 3 the SE measured continuously, while for ALD deposited films the SE was used in a light triggered mode, only allowing measurements when the SE valves were opened, which was always between two ALD cycles to avoid deposition on the optical windows.

The angle of incidence for the *in situ* measurements was 70°. For the *ex situ* SE measurements the angles of incidence were 70°, 75° and 80°. CompleteEase software was used to measure and analyze the data.

Optical modelling and data analysis

An optical model is needed to deduce the dielectric function from the acquired data. As mentioned before, a temperature dependent model of the silicon substrate was used for *in situ* SE measurements to provide the substrate temperature and the thickness of the native oxide. The deposited silicon nitride films were modelled with a Tauc-Lorentz model. This model is used to model the dielectric function of amorphous materials and is a combination of the Tauc joint density of states and the Lorentz model [20, 21]:

$$\varepsilon_2(E) = \begin{cases} \dfrac{AE_0C(E-E_g)^2}{(E^2-E_0^2)^2+C^2E^2} \cdot \dfrac{1}{E} & \text{if } E > E_g \\ 0 & \text{if } E \leq E_g \end{cases} \tag{2.1}$$

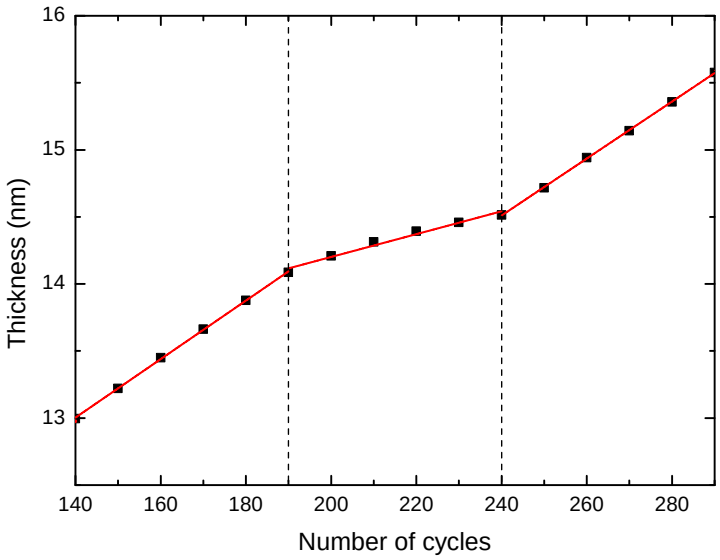

Figure 2.3: An example of linear regression of the thickness data that is obtained by depositing stacked layers with three different deposition conditions (140-190 cycles, 190-240 cycles and 240-290 cycles). The red lines are linear fits of the data points and their slope corresponds to the GPC.

E_g is the bandgap energy, E_0 the peak transition energy and C the broadening term. ε_1 can then be calculated by using the Kramers-Kronig relations and its expression can be found in [22].

The thickness and dielectric function obtained by the modelling are often related, which is undesired as it complicates the unique determination of the real physical values. This correlation increases for decreasing film thickness, which makes it difficult to fit very thin films correctly [19].

In situ SE has the advantage that it can be used to determine the growth per cycle (GPC) for several conditions on one substrate, while *ex situ* diagnostic techniques require a new sample for every condition. *In situ* SE can therefore easily be used to investigate the self-limiting properties of the process by varying a certain parameter (e.g., plasma time, precursor dosing time, purge time) and determining the GPC per condition by linear regression, as shown in figure 2.3. This way a so-called saturation curve can be made, which shows the GPC for the variation of one parameter.

Other advantages of *in situ* SE are that the experiment can be stopped when the film has reached the desired thickness and that it is immediately seen when the process does not run properly due to deviations from the linear relation between thickness and number of cycles.

The optical band gap (E_g) of the material can be deduced from ε_2 by means of a Tauc plot. First, for a material with an indirect band gap, $\sqrt{\varepsilon_2 E^2}$ is plotted as a function of the photon energy [19]. Then, the linear part of this parameter is extrapolated and the intersection with the line $\sqrt{\varepsilon_2 E^2} = 0$ determines the optical band gap [19, 20]. An example is shown in figure 2.4.

Furthermore, the results of SE mapping experiments will be shown. These experiments

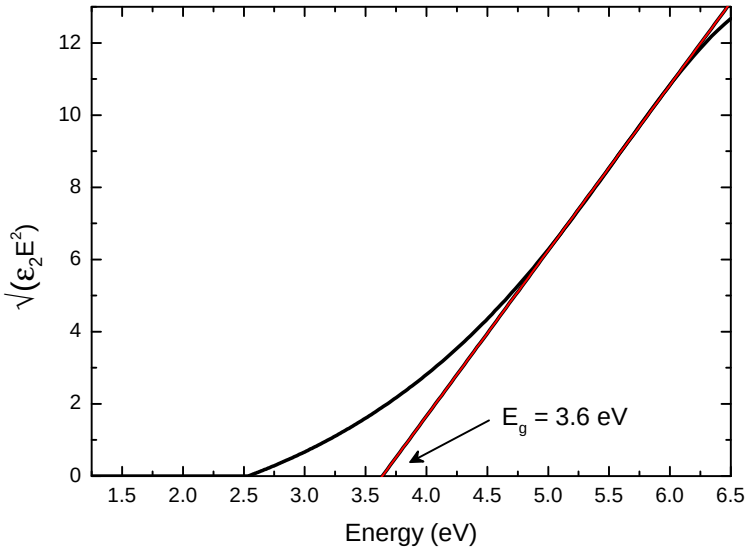

Figure 2.4: An example of how a Tauc plot can be used to determine the optical band gap of a silicon nitride film. The red line shows the extrapolation of the linear part of the parameter $\sqrt{\varepsilon_2 E^2}$.

were used to determine the thickness uniformity and the uniformity of the refractive index across the wafer. Due to the presence of (dust) particles on top of the samples, some small areas could not be fitted properly. Therefore, data points with a modelling error that was more than the average modelling error were not taken into account when the uniformity was calculated.

2.3.2 Quadrupole mass spectrometry (QMS)

Quadrupole mass spectrometry (QMS) is a non-invasive technique, that extracts a small fraction of gas phase species from the reactor. Typically, only stable species are detected with QMS, since radicals in the plasma mostly recombine at surfaces before entering the QMS [23]. These stable gas species are ionized by electron impact ionization which results in ionized parent molecules, but also, depending on the electron energy, in ionized fragments of the parent molecules due to dissociation. The quadrupole mass filter separates these ions according to their mass to charge ratio (m/Z). Most ions will be singly charged and therefore their m/Z value is the same as their mass, but for ions with charge different from one, the mass and m/Z value do not correspond. The detection of the ions that pass through the mass filter occurs in a secondary electron multiplier. The QMS used in this work is a Pfeiffer Vacuum QMS 200 with an electron energy of 70 eV and a m/Z range of 200 atomic mass units.

QMS measurements

In this work, QMS measurements were done to monitor the process and to determine the reaction products. Since each molecule has a typical fragmentation spectrum, which acts as a fingerprint for that molecule, typical m/Z values in these so-called cracking patterns can

be used to follow certain species during the ALD cycle. Many cracking patterns are listed in the NIST database [24] and can be used to identify the parent molecules for the m/Z spectra that are measured. The time resolution depends on the number of m/Z values that are measured in a time-dependent measurement.

To monitor the process, 8 representative m/Z values were measured during the deposition processes: 2, 15, 17, 27, 28, 29, 40 and 58. $m/Z = 58$ is related to the precursor, as will be shown in section 5.1.2, and this signal was used to monitor whether there still was precursor in the bubbler. Determination of the reaction products was done in a separate study and the measurement procedure for this study will be addressed in section 5.1.1.

2.3.3 Optical emission spectroscopy (OES)

With optical emission spectroscopy (OES) the light that is emitted by the plasma is measured. The atoms and molecules in the plasma can be excited by collisions (e.g., with electrons) and the resulting electronically excited states of these species can decay by emission of a photon. The emission lines in an OES spectrum are caused by these photons. Since specific transitions correspond to certain energies, the emission lines can provide information about the atoms and molecules present in the plasma. The spectrometer used in this work was an Ocean Optics USB4000-UV-VIS spectrometer.

OES measurements

There are two types of measurements that can be done with OES. The first one is the measurement of spectra, which provides information in the whole wavelength range of the spectrometer. The second method, which was used in this work, is the measurement of a few specific wavelengths over time. When these wavelengths are chosen carefully, they can provide information about the reaction products and/or surface reactions, as will be shown in chapter 5. OES was used qualitatively to observe relative changes in reaction products in this work.

2.3.4 X-ray photoelectron spectroscopy (XPS)

X-ray photoelectron spectroscopy (XPS) is a technique to determine the relative atomic concentrations in the surface region of a sample. This is done by irradiating a sample with soft monochromatic X-rays in a ultra high vacuum chamber, which results in ejection of electrons from the core levels of the atoms. The kinetic energy of these electrons is measured and can be used to calculate their binding energy. Since each element has a characteristic set of electrons with specific binding energies (corresponding to the electron configuration), a binding energy spectrum can be used to determine which elements are present in the surface region (XPS has a penetration depth of a few nanometers). The peak areas are related to the concentrations. It is also possible to measure a depth profile, which is done by sputtering the sample with argon ions. After each sputter step, the elements of interest can be measured. Hydrogen and helium cannot be detected by XPS, the instrumental detection limit for other elements is 0.1%.

The chemical shift is the change in binding energy due to a change in chemical bonding of the atom. Because the binding energy of the ejected electrons depends on the chemical environment of the atoms, these energies can be used to determine the chemical state of the elements in the sample. Therefore, deconvolution of each peak results in separate peaks that provide information about the different chemical states of the atom. The binding energies

determined by deconvolution can be compared to binding energies listed in the NIST X-ray Photoelectron Spectroscopy database [25].

A Thermo Scientific K-Alpha spectrometer with an Al Kα monochromator X-ray source (hν = 1486.6 eV) was used in this work.

XPS measurements

Ex situ XPS measurements were performed to determine the composition of the films and to investigate the chemical state of the elements silicon, nitrogen, carbon and oxygen. This was done by measuring the depth profiles of the deposited films. The concentrations were calculated by dividing the XPS signal by a sensitivity factor (specific for each element). These sensitivity factors were loaded from a database in the software and the accuracy of these factors is within 1%, depending on the calibration material used. In this work, the concentrations were determined in the bulk film, while the interfaces (i.e., the surface and the interface with the native oxide) were neglected.

As a result of sputtering, the stoichiometry of the film can be changed due to preferential sputtering of some elements and the chemical state of the element can be changed. Oxygen in the background of the XPS chamber penetrates into the film after sputtering and the effect in the measurements can be minimized by measuring oxygen as the first element after each sputter step.

Due to the combination of the uncertainty in the sensitivity factors and the effect of sputtering, it is difficult to obtain accurate absolute values for the calculated concentrations. However, the observed trends are representative since the aforementioned uncertainties result only in systematic errors. A comparison with other diagnostic techniques is required to determine how accurate the absolute values are. Also, since hydrogen cannot be detected, the calculated percentages are higher than the actual concentrations, but they can be corrected when the hydrogen content is known from other diagnostics.

The peak position of the binding energy depends on the chemical environment of the element. To determine the chemical state of the elements, the peaks were deconvoluted and the resulting peak positions were compared to the binding energies in the NIST X-ray Photoelectron Spectroscopy database [25]. The chemical shifts were observed for changing compositions due to the difference in electronegativity of the elements in the films (oxygen has the highest electronegativity, followed by nitrogen, carbon and silicon). The higher the electronegativity of the environment, the higher the binding energy. The areas of the deconvoluted peaks were used to determine the relative amounts of chemical bonds for each element.

2.3.5 Rutherford backscattering spectrometry (RBS) and elastic recoil detection (ERD)

Rutherford backscattering spectrometry (RBS) and elastic recoil detection (ERD) measurements are *ex situ* ion-beam-assisted techniques, used to determine the composition and mass density of the films [26]. Furthermore, the number of adsorbed atoms per unit area per cycle could be calculated as well. For RBS a beam of 1.85 MeV helium ions is directed at a sample and after reflection off the sample the energy of the ions is measured [26]. This energy is reduced compared to the incident energy due to the stopping power of the material. The energy lost in the collision with an atom depends on the ratio of the helium ion mass to the mass of the atom. In ERD the helium ion beam hits the surface of the sample at a grazing angle, resulting in recoiled hydrogen atoms (in a forward direction) [26]. To prevent the

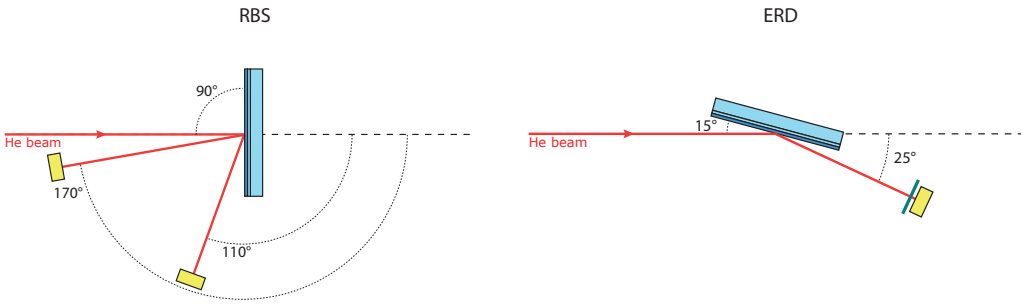

Figure 2.5: The RBS and ERD measurement configurations, showing the angles of incidence and reflectance for which the energy of the reflected helium ions and the recoiled hydrogen atoms were measured.

detection of scattered helium ions a stopper foil is used, which stops the helium ions, while the recoiled hydrogen atoms can pass [26].

RBS and ERD measurements and simulations

The experiments and the simulations were performed by AccTec B.V. The angle of incidence of the ion beam for RBS was 90°. Silicon and nitrogen contents were determined by RBS, with an angle of reflection of 170°, while the angle of reflection for carbon and oxygen was 110°, as shown in figure 2.5. The hydrogen content was determined by ERD, with an angle of incidence of 15° and an angle of reflection of 25°. Simulations were used to determine the concentrations of the elements.

The quality of the model determines the accuracy of the concentrations. The first model assumed that the film had the same composition across the whole thickness and that there was no native oxide between the wafer and the film. However, the simulations with this model resulted in a difference between the simulated and measured ion energies, suggesting that oxygen and carbon were accumulated at the surface and that a native oxide was present. Incorporation of a native oxide layer in the model resulted in a better correspondence between experiment and simulation, but still there was a difference due to the accumulation at the surface. When the oxygen and carbon accumulations at the surface were also taken into account, the correspondence between simulation and experiment improved, but resulted in a zero carbon concentration in the bulk of the film, while XPS data showed a (small) carbon content in the film. Therefore, the model with a native oxide layer but without accumulated oxygen and carbon at the surface was used. This could result in a slight overestimation of the carbon content in the film.

Chapter 3

Temperature measurement and control

One of the goals of this work was the deposition of silicon nitride in a wide temperature window. Therefore it was important to determine the temperature of the samples accurately. This determination was done by SE measurements with a temperature dependent substrate model, as will be discussed in the following two sections. There were several parameters that influenced the substrate temperature. The influence of one of them, the helium backflow in the ICP-CVD system, is addressed in section 3.3. An important question was of course whether the measured SE temperature corresponded to the actual sample temperature and this question will be answered in section 3.3 as well. The information obtained on the ICP-CVD system was used to determine the sample temperature and the influence of the chamber pressure and gas flows on the wafer temperature in FlexAL2, as will be shown in section 3.4. The accuracy of the measured SE temperature is also discussed in this section. The last section of this chapter addresses the possibility to control the temperature by using SE measurements.

3.1 Substrate temperature basics

The temperature of the sample depends on various parameters, as is illustrated in figure 3.1. Depending on the thermal contact between the wafer table and the sample, the sample temperature (T_{sample}) can be any temperature between the temperature of the walls (T_{wall}) and the temperature of the wafer table (T_{table}). The wafer table temperature is the same as the setpoint temperature (T_{set}), which has been determined by thermocouple measurements. Thus, $T_{wall} < T_{sample} < T_{table} = T_{set}$.

There are three heat transfer mechanisms: radiation, conduction and convection. In the absence of gases in the reactor, convection does not play a role. The heat flux due to radiation can be described by

$$Q_{rad} = \epsilon \sigma T^4, \tag{3.1}$$

where Q_{rad} is the heat flux (W/m^2), ϵ the emissivity, σ the constant of Stefan-Boltzmann ($5.67 \cdot 10^{-8}$ W m^{-2} K^{-4}) and T the temperature of the radiating object in Kelvin. Each object radiates, the wafer thus receives a heat flux from the wafer table and the walls, but also emits radiation itself. The emissivity is the efficiency with which an object emits radiation compared to a black body [27] and it depends on the material, the surface roughness, doping levels and the temperature [27, 28]. The absorptivity of a material is the fraction of the incident

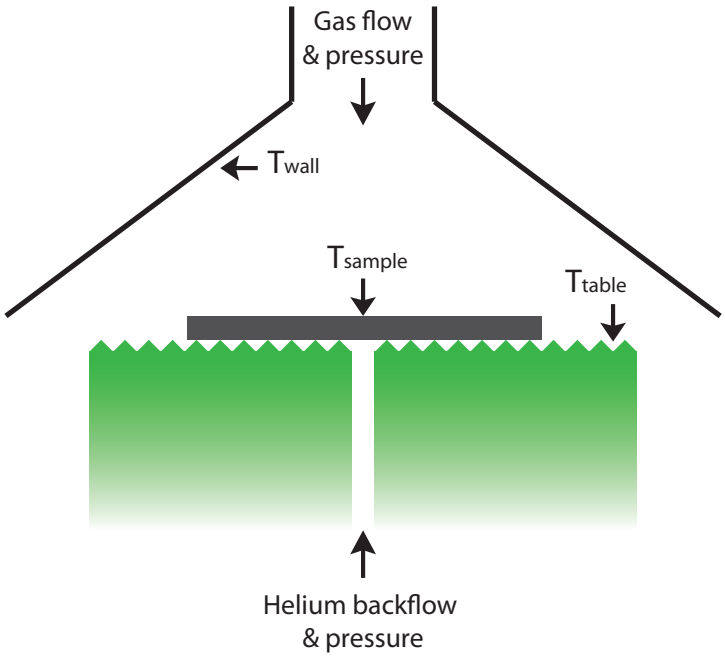

Figure 3.1: A schematic overview of a reactor chamber, indicating the parameters that influence the sample temperature.

radiation that is absorbed. The emissivity is sometimes assumed to be equal to the absorptivity [28]. Lightly doped silicon has a very low emissivity for temperatures below 300°C [28, 29], the radiation loss at these temperatures is thus negligible. Above this temperature the emissivity increases due to an increase of the free-carrier concentration towards its maximum value of ≈ 0.7 [27–29]. The emissivity also increases for increasing surface roughness [27].

The heat flux due to conduction can be defined as

$$Q_{cond} = \lambda \frac{T_{hot} - T_{cold}}{x}, \tag{3.2}$$

with λ the thermal conductivity (W m^{-1} K^{-1}) of the conducting material and x the distance between the hot and cold surface. From figure 3.1 it is clear that, since the wafer lies on top of the table, x is very small for the thermal contact between wafer and table, while x is relatively large between the wafer and the reactor walls. The thermal contact between the wafer and the wafer table is therefore the most important contribution to Q_{cond}. λ depends on the temperature and gas types in the reactor. When there is no gas in the reactor, the thermal contact is determined by the thermal conductivity of the wafer table and the contact area between the wafer and the wafer table.

The thermal contact between the sample and the wafer table depends on the roughness of the wafer table and the wafer, but also on the presence of gases in the reactor and the pressure of these gases. Depending on the roughness of the wafer and the table, the contact between these two can be limited to several points, while the presence of a gas increases the contact area by the formation of a very thin gas film between the wafer and the table. In the ALD literature, experiments are mostly performed at relatively high pressures (1 Torr), where the difference between T_{set} and T_{sample} will be small. However, for low pressures the thermal contact can be less and the heat loss from the top of the sample (although small) can lead to a relatively low sample temperature compared to the setpoint temperature.

The temperature is not measured with a thermocouple, because it can be difficult to achieve a good thermal contact when the thermocouple is glued onto the wafer and with a thermocouple attached, wafer handling is less straightforward. Instead, the temperature is determined by *in situ* SE, which is an optical, contactless and non-invasive technique. This diagnostic does not influence the thermal contact.

In order to get accurate results with SE, the calibration is very important. For an increasing temperature the calibration starts to drift due to expansion of the reactor parts, which causes an increasing misalignment. It is therefore important to calibrate the SE every time the reactor temperature is changed. When this setpoint temperature is increased, the temperature of the wafer table and the sample increase gradually. After the setpoint temperature is reached, the wafer needs some time to reach a stable temperature.

3.2 The dielectric function of the silicon substrate

A temperature dependent SE model is used to measure the sample temperature. The model consists of the material files of the temperature dependent silicon substrate (Si Temp JAW (Temp Library) by J.A. Woollam) and its native oxide on top (NTVE_JAW) [30]. The optical constants resulting from this model are plotted in figure 3.2 for temperatures between 0°C and 500°C. The shape of these curves is determined by the band structure of silicon. ε_2 is related to the absorption of the material and it shows a peak around 3.4 eV, which corresponds to two nearly degenerate direct band gap transitions of silicon [31, 32]. However, silicon is an indirect band gap material, which explains why there is already absorption below 3.4 eV. In this range the absorption occurs due to interaction with phonons, which are needed in indirect transitions for the conservation of momentum. The indirect band gap is approximately 1.1 eV [31, 33]. Other direct band gap transitions occur around 4.3 eV, explaining the peak in ε_2 at that position [32, 34].

The temperature of the substrate influences the shape of the optical constants, which is caused by thermal expansion and the electron-phonon interaction [32]. The higher the temperature the more phonons become involved in the absorption process [31]. For an increasing temperature the direct band gaps move towards lower photon energies [31–33] and the absorption features broaden [31, 32].

3.3 Helium backflow

A helium backflow can illustrate the importance of the thermal contact between the wafer table and the substrate. The influence of the helium backflow on the substrate temperature was investigated on an ICP-CVD system (Oxford Instruments PlasmalabSystem100 (ICP 180)), because FlexAL2, the ALD system, had no helium backflow installed. In the ICP-CVD system the substrate was clamped onto the wafer table, which was not the case for FlexAL2. The temperature of the walls in the ICP-CVD system was 40°C.

A helium backflow was used to enhance the thermal contact between the substrate and the wafer table, because helium has a high thermal conductivity [35]. The high thermal conductivity (λ = 146.0 mW m^{-1} K^{-1} at 273.15K [36]) is important for the minimization of the temperature difference between the wafer table and the sample. Even though hydrogen has a higher thermal conductivity than helium, helium is preferred above hydrogen. This is due to the high ionization potential of helium (24.6 eV). Hydrogen can be dissociated and has a relatively low ionization potential of 13.6 eV. Therefore, very small amounts of hydrogen can already influence the plasma chemistry [35].

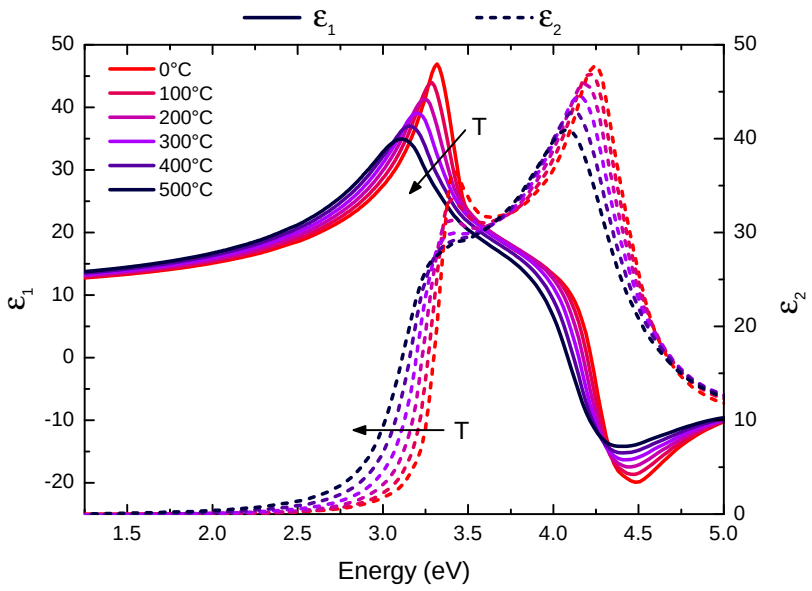

Figure 3.2: The optical constants of the silicon substrate for different temperatures according to the temperature dependent SE model by J.A. Woollam.

The ICP-CVD system is equipped with helium backflow and the amount of helium that flows through the channel is controlled by setting the helium pressure in the gas line, for which the standard value is set to 5 Torr. The effect of the helium backflow on the substrate temperature was measured for a setpoint temperature of 200°C and 390°C (the maximum operating temperature of the system is 400°C). Because the emissivity and absorptivity are relatively small at these temperatures, heat transfer will mainly be governed by conduction.

Figure 3.3 shows that the substrate temperature increased when the helium backflow was turned on; as expected, the helium enhanced the thermal contact between the wafer table and the substrate. When the helium backflow was turned off again, the temperature decreased to the same value it had before the helium flow was activated, showing that the effect of the helium on the temperature was reversible. When there was no helium backflow, the wafer table heated the wafer via radiation and thermal conduction through small contact points (due to the surface roughness). After a certain time an equilibrium situation was obtained. By enabling the helium backflow an additional heat transfer mechanism was switched on: thermal conduction via the thin helium gas film between the sample and the wafer table. This resulted in a new equilibrium situation with an increased thermal contact between the wafer and the wafer table, leading to a higher sample temperature. When the helium flow was turned off again, the 'old' equilibrium situation applied, since the additional heat transfer mechanism due to the helium gas was switched off again and the sample temperature returned to its original value.

Figure 3.4 shows the temperature increase for a wafer that was inserted into the reaction chamber, which was set to a temperature of 200°C. Again, the wafer temperature was closer to the setpoint temperature when the helium backflow was used and the final temperature was also reached faster than without helium backflow.

In figures 3.3 and 3.4 the setpoint temperature (indicated by the dashed lines) was not reached. For 390°C the difference between the setpoint temperature and the wafer tempera-

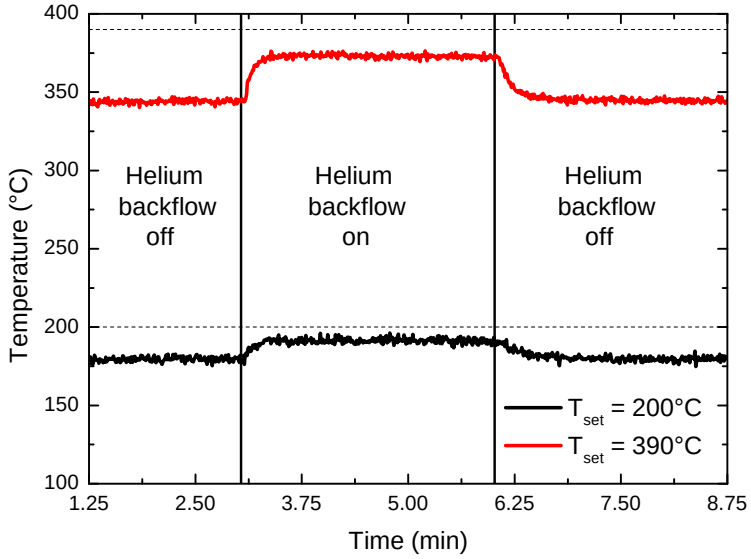

Figure 3.3: The reversible effect of the helium backflow on the measured SE temperature for a setpoint temperature of 200°C and 390°C. The dashed lines indicate the setpoint temperatures.

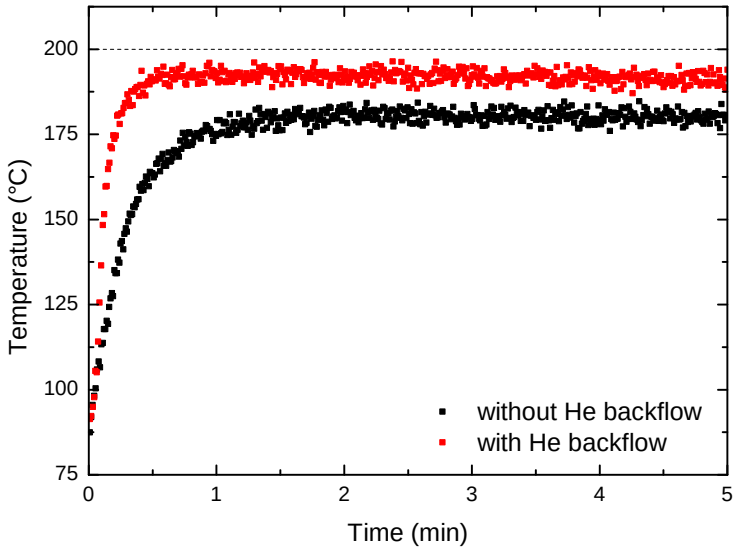

Figure 3.4: The temperature development for a wafer that was heated to a setpoint temperature of 200°C with and without helium backflow. The dashed line indicates the setpoint temperature.

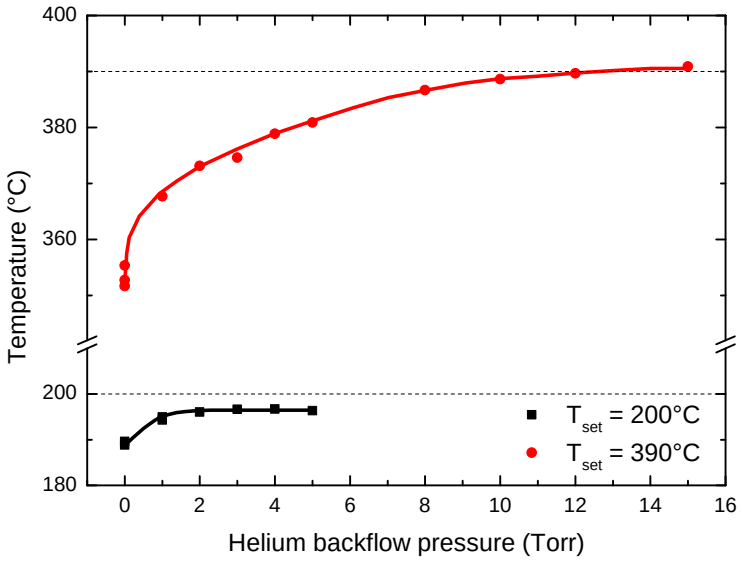

Figure 3.5: The effect of an increasing helium pressure on the measured sample temperature for a setpoint temperature of 200°C and 390°C. The black and red line serve as guides to the eye. The dashed lines indicate the setpoint temperatures.

ture was larger than for 200°C, as shown in figure 3.3. This might be due to an insufficient flow of helium at a standard helium pressure of 5 Torr. In order to test this, the helium pressure was varied for both setpoint temperatures and figure 3.5 shows the effects on the temperature. For an increasing helium pressure the difference between the setpoint temperature and the sample temperature reduced. For a setpoint temperature of 200°C a helium pressure of 2-3 Torr was sufficient for the wafer to reach a stable temperature, while for a setpoint temperature of 390°C a helium pressure of 15 Torr was required for the wafer to reach 390°C. The thermal conductivity of helium increases for increasing temperature, which explains why at a setpoint temperature of 200°C this temperature was not reached, while the setpoint temperature of 390°C could be reached with a sufficiently high helium pressure [36].

An increase in helium pressure corresponds to an increase in helium flow, which might influence the plasma characteristics, since the helium flows into the chamber and dilutes the plasma. The amount of helium that flowed into the chamber as a function of the helium pressure is shown in figure 3.6 and the resulting effects on the chamber pressure are noted in table 3.1. Processing flows can range between 10 sccm and 100 sccm. The helium flow could thus be a significant fraction of these processing flows for high helium pressures, which must be considered when increasing the thermal contact between the wafer table and the sample. The effect on the chamber pressure was in most cases negligible, since the processing pressures were often two or three orders of magnitude higher than the pressure effect of the helium backflow.

The results on the helium backflow show that the measured sample temperature increased when the thermal contact between the substrate and the wafer table was increased and that the thermal contact depended on the applied helium pressure. The setpoint temperature could be reached for high temperatures, while for lower temperatures the thermal conductivity

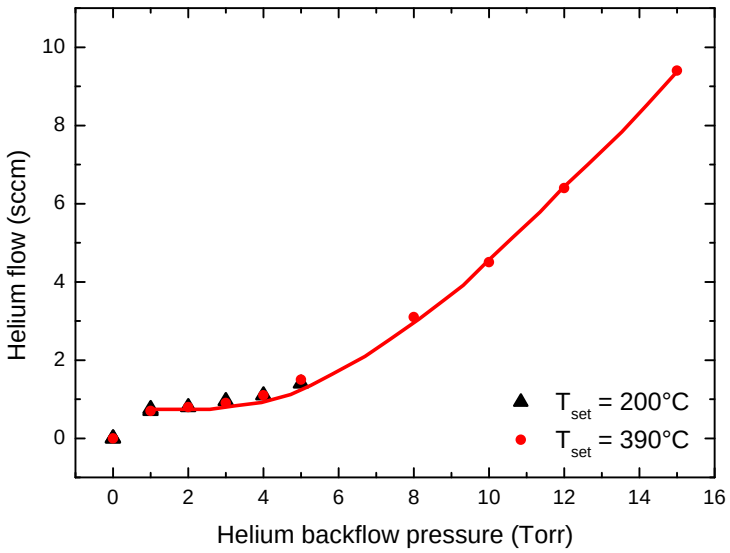

Figure 3.6: The helium flow as a function of the helium pressure. The red line serves as a guide to the eye.

Table 3.1: The influence of the helium pressure on the chamber pressure.

Helium pressure (Torr)	Chamber pressure (mTorr)
0-5	0 ±0.1
8	0.1
10	0.1
12	0.2
15	0.3

of helium was not sufficient to reach the setpoint temperature. These observations confirm that *in situ* SE can be used to measure the temperature of the sample accurately.

3.4 Temperature measurement on FlexAL2

At FlexAL2 the first temperature measurements performed with *in situ* SE resulted in temperatures lower than the setpoint temperature and the difference between these temperatures increased for increasing setpoint temperature. Therefore, the temperature of the wafer table was measured with a thermocouple as a function of the setpoint temperature to see whether the heater was working properly. Since the wafer table temperature and the setpoint temperature corresponded to each other, the low measured sample temperature was most likely due to a decreased thermal contact compared to the ICP-CVD system. As mentioned before, the FlexAL2 has no helium backflow and the wafers are not clamped onto the wafer table, which might explain the reduced thermal contact.

To verify that the low measured temperatures were not due to systematic errors in the SE measurements/modelling, the wafer temperature was measured with a thermocouple, while at the same time *in situ* SE measurements were performed. This was done for a pressure of 0 mTorr and a pressure of 200 mTorr because the gas pressure (during processing) might influence the thermal contact. The results are shown in figure 3.7. The error in the thermocouple measurements was ± 1°C, while the noise in the SE measurements increased from ± 3°C to ± 9°C for setpoint temperatures from 200°C to 400°C. The measured thermocouple and SE temperatures showed the same trends and the difference between these two were ascribed to the systematic error in the SE measurement, which also increased with temperature. The measured temperature deviated from the setpoint temperature (T_{table}) for both thermocouple and SE for setpoint temperatures of 200°C and higher. The difference between the measured temperature and the setpoint temperatures increased for increasing setpoint temperature.

There was also a difference between the measured temperatures for the different pressures: at the same setpoint temperature the measured temperature was higher for a pressure of 200 mTorr than for 0 mTorr. The difference between the measured temperature at 200 mTorr and the measured temperature at 0 mTorr increased for increasing setpoint temperatures as well. As expected, this indicates that the sample temperature depended on the gas pressure, which influenced the thermal contact between the wafer and the wafer table. Since this thermal contact was poor, even for a pressure of 200 mTorr, the temperature of the chamber walls played an important role, because of the large area of these walls compared to the area of the heater. The wall temperature was set to its maximum allowed value of 150°C for $T_{set} \geq 150$°C, explaining why the difference between the substrate and wafer table temperature increased for increasing setpoint temperature.

A calibration is needed to know the sample temperature that corresponds to a certain setpoint temperature at a certain pressure. Table 3.2 can be used as a guideline for the relationship between the setpoint temperature and the sample temperature. **The temperatures mentioned in the following chapters are the setpoint temperatures unless stated otherwise.**

A question that arised was whether the type and amount of gas flow influenced the thermal contact. Therefore, the sample temperature was measured at a setpoint temperature of 500°C (the maximum setpoint temperature for FlexAL2) for various combinations of gas flow and pressure for three different gases: N_2, Ar and H_2. The results are shown in table 3.3. For all three gases the sample temperature increased for increasing pressure, while the influence of the gas flow was not significant. The sample temperature never reached the setpoint temperature

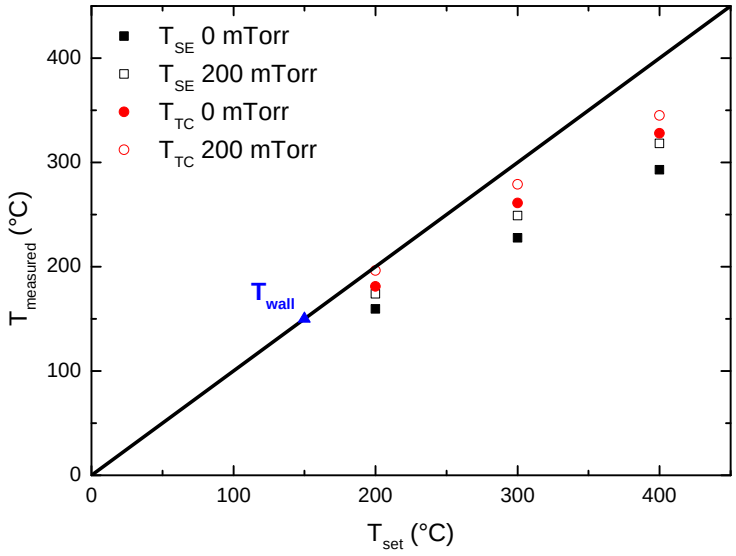

Figure 3.7: The measured thermocouple and SE temperature (T_{TC} and T_{SE}) as a function of setpoint temperature for a pressure of 0 and 200 mTorr. H_2 gas was used for the measurements at 200 mTorr. The black line corresponds to $T_{measured} = T_{set}$. T_{wall} was set to 150°C.

Table 3.2: A guideline for the relation between the sample temperature (measured with *in situ* SE) and the setpoint temperature for a pressure of 0 mTorr. For a plasma process with a pressure of 40 mTorr and a gas flow of 100 sccm N_2 (as mainly used in the next chapters) the sample temperature is approximately 25°C to 40°C higher.

T_{set} (°C)	T_{sample} (°C)
100	85
200	155
300	210
400	275
500	355

Table 3.3: The influence of N_2, Ar and H_2 gas on the sample temperature for different pressures and flow rates at a setpoint temperature of 500°C.

Gas flow	Pressure	Temperature (°C)		
(sccm)	(mTorr)	N_2	Ar	H_2
0	0	316	319	317
50	20	329	328	325
100	20	329	328	330
100	100	360	354	359
100	240	384	374	386
200	240	-	375	-

of 500°C, but, depending on the gas type and pressure, was 115°C to 185°C lower than the setpoint temperature. The thermal conductivity at a temperature of 600K is 309.1 mW m^{-1} K^{-1} for hydrogen, 44.8 mW m^{-1} K^{-1} for nitrogen and 30.3 mW m^{-1} K^{-1} for argon [37]. As expected from these values, the hydrogen and nitrogen gas gave the best thermal contact, argon the poorest. Note that, although the trend fits, the exact differences in the resulting temperatures cannot be explained by the thermal conductivities. The thermal contact did not only depend on the gas pressure, but also on which gas was used. The influence of the gas' thermal conductivity on the temperature difference between the setpoint temperature and the wafer temperature showed the contribution of thermal conduction to the heat transfer. Although the emissivity of the wafer was low for these temperatures, the radiation of the wafer was still significant, since the temperature of the wafer did not reach temperatures of 400°C or higher for improved thermal contact between the wafer table and the wafer.

The observation that both the pressure and gas type determined the sample temperature was a reason to investigate the sample temperature during a regular process. In figure 3.8 the SE temperature and thickness of the native oxide are plotted for regular processes, but the valve of the BTBAS bubbler was closed to avoid silicon nitride film growth. For the 'gas' processes mentioned in figure 3.8 the plasma power was set to 0W, while for the 'plasma' processes the power was 600W. Each process consisted of 20 cycles. The temperature increased when both processes were run. After the process had ended, the substrate temperature decreased slowly again. For a 'gas' only process (1A, 2A and 3A in figure 3.8), the temperature always decreased back to initial temperature, while for the first 'plasma' process the temperature after the process was about 15°C higher than before (1B in figure 3.8). Since the stable temperature after the 'plasma' processes 2B and 3B was the same as the temperature before the processes were started, it is likely that the first plasma changed the native oxide layer, probably by nitridation. This influenced the optical constants of the top material, leading to an incorrect temperature. The 'plasma' test was also done for 100 cycles and this experiment showed that the temperature stabilized after approximately 20 cycles and only changed again when the process was ended. The difference between the maximum and minimum value of the sample temperature at a setpoint temperature of 200°C was between 15°C and 20°C (2B and 3B in figure 3.8). One consequence of this is that the sample temperature dropped when an SE measurement was done, but since these only lasted for 25 seconds the temperature drop was negligible (less than 5°C for a setpoint temperature of 200°C) and the temperature stabilized in less than 10 cycles after each measurement. The fact that the temperature was affected for both types of processes indicated that the process temperature depended on the presence of a gas flow and not on the plasma power.

The thickness of the native oxide, however, was only influenced by the plasma (1B, 2B

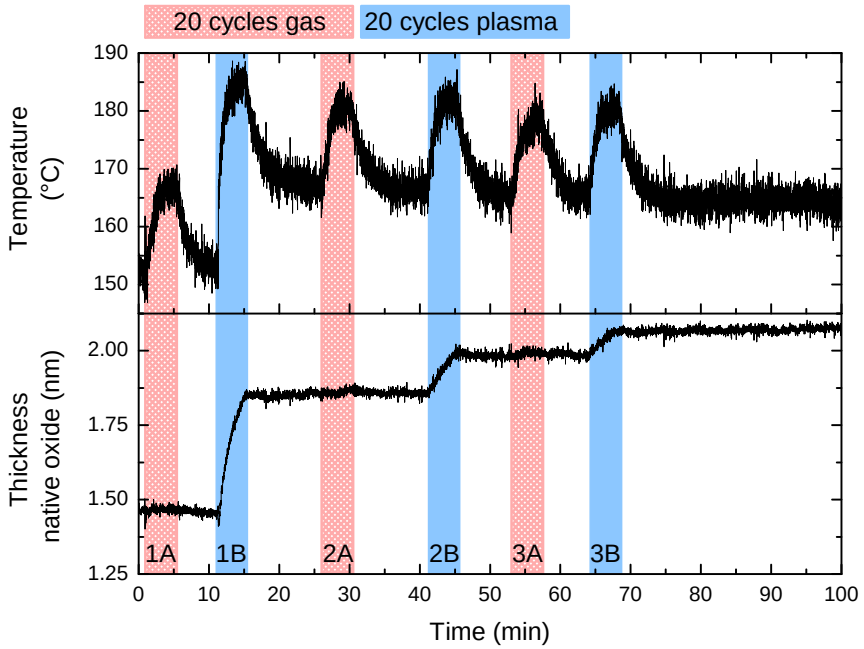

Figure 3.8: The influence of a N_2 plasma and the N_2 gas flow on the measured SE temperature and native oxide thickness for a setpoint temperature of 200°C. Each process consisted of 20 cycles.

and 3B in figure 3.8) and not by the gas flow (1A, 2A and 3A). The thickness increased with each plasma process, but each process resulted in less thickness increase than the one before. The thickness increase of the native oxide layer can be explained by nitridation of the native oxide and the underlying silicon wafer [38]. Even for wafers from which the native oxide layer was removed, these oxynitride layers existed, due to nitridation by the N_2 plasma and oxidation in the reactor due to background species and high temperatures. The oxidation and nitridation of the silicon wafer and the native oxide on top might influence the initial growth and the measurement of this initial growth.

3.5 Temperature control

The SE measurements gave an accurate value of the sample temperature and could therefore also be used for temperature control. When, for instance, a carrier wafer was used to bring the sample into the chamber, the wafer temperature was further reduced compared to the case without a carrier wafer. The setpoint temperature could then be increased, while the wafer temperature was monitored with SE until it reached the desired value. When the temperature was stable again, the SE could be calibrated and after that, the SE could be used to measure the film properties during the deposition process, which then ran at the same wafer temperature as when there would be no carrier wafer.

Chapter 4

Atomic layer deposition of silicon nitride: growth & material properties

In this chapter the development of the ALD process for silicon nitride with the metalorganic precursor bis(tertiary-butylamino)silane (BTBAS) will be discussed. As a first test for the precursor, experiments were done to deposit silicon dioxide as this material is generally easier to deposit by ALD than silicon nitride. The process showed the saturation behavior that is expected for an ALD process and the growth per cycle (GPC) was close to the values reported for ALD of SiO_2 using BTBAS [18]. The results for the SiO_2 process can be found in appendix A. Further improvement of this process might be possible, but this was outside the scope of this work.

After the test with SiO_2 the deposition of silicon nitride was investigated. There are several steps in an ALD cycle that can be optimized to obtain saturation behavior and a reasonable cycle time and GPC, which will be discussed in the first section. Since it was expected that the plasma properties and the deposition temperature are important for the growth and material properties, section 4.2 will address the properties of the deposited films as a function of three deposition parameters; plasma exposure time, deposition temperature and plasma pressure. A short summary of the results and a comparison with other deposition techniques will be given in the last section of this chapter.

4.1 Optimization of the deposition process

For a plasma-assisted ALD process, minimization of the cycle time, while ensuring saturation, means optimization of the precursor dose, the precursor purge, the plasma and the plasma purge steps. This can be achieved by measuring the saturation curves for these four steps. Additionally, the plasma exposure parameters were optimized to get the highest GPC. These optimization experiments were done by the deposition of stacked layers on a substrate and the thickness was measured by *in situ* SE, as was explained in section 2.3.1. The resulting step times and plasma exposure parameters were used to establish a 'standard' recipe for which a film was deposited on a separate wafer to investigate the film properties with *ex situ* diagnostics.

Table 4.1: The deposition conditions for the determination of the saturation curves.

Deposition parameter	Condition A	Condition B
Temperature (°C)	350	varied
BTBAS dosing time (ms)	200	200
Precursor purge time (s)	1	1
Plasma exposure time (s)	5	3
N_2 plasma flow (sccm)	50	100
Plasma pressure (mTorr)	25	40
Plasma power (W)	600	600
Plasma purge time (s)	1	1

4.1.1 Saturation curves

Saturation curves can be used to investigate the ALD behavior. They show the growth per cycle (GPC) as a function of the step time and it can be concluded that saturation occurs when the GPC becomes independent of the step time. The saturation behavior can also be temperature dependent and was therefore investigated at several temperatures.

Obtaining the saturation curves is an iterative process, because the length of each step can influence the length of another step. After starting with one set of deposition conditions, optimization of some parameters led to a new set of deposition conditions and these new conditions were used to measure saturation curves at different temperatures. Therefore, there were two sets of deposition conditions for the saturation curves in figure 4.1. The used conditions are listed in table 4.1. For these processes, the argon flow was used as a carrier gas during the precursor dosing and the butterfly valve of the reactor was closed during the reaction step.

Figure 4.1a shows the saturation curves for the precursor dosing at three different setpoint temperatures. The GPC showed a reasonable saturation for increasing precursor dose times, although a small CVD component was observed for long dose times at higher temperatures. This might be avoided by using longer precursor purge times at these dosages. When the temperature was increased the GPC decreased.

The saturation curve for the precursor purge time is shown in figure 4.1b for a setpoint temperature of 350°C. The GPC saturated for purge times of 0.75 seconds and longer.

Figure 4.1c shows the GPC for varying plasma exposure times for a N_2 plasma. The GPC saturated for plasma exposure times above 1.5 seconds. For longer plasma exposure times the GPC seemed to decrease a little. In figure 4.1d the saturation curves for N_2 plasma exposure times at setpoint temperatures between 100°C and 500°C are shown. For temperatures between 150°C and 350°C the GPC first saturated and then decreased again for longer plasma exposures. This effect is investigated in more detail in section 4.2.1.

The GPC is plotted as a function of plasma purge time in figure 4.1e. Saturation occurred for plasma purge times longer than 0.5 seconds.

The process with the N_2 plasma showed the saturation behavior that is required for an ALD process; the two half-reactions were self-limiting. King reported a silicon nitride ALD process with alternating exposures of SiH_4 gas and a N_2 plasma, resulting in a GPC between 0.25 Å and 2 Å [15]. When NH_3 was added to the N_2 plasma, the GPC was reduced to less than 0.03 Å [15]. This is surprising, since NH_3 plasmas do result in growth when metal halide precursors are used [11, 13]. When the N_2 plasma was replaced by an NH_3 or H_2-N_2 plasma in this work the GPCs were approximately 20% and 10% of the GPC for a N_2 plasma of 5

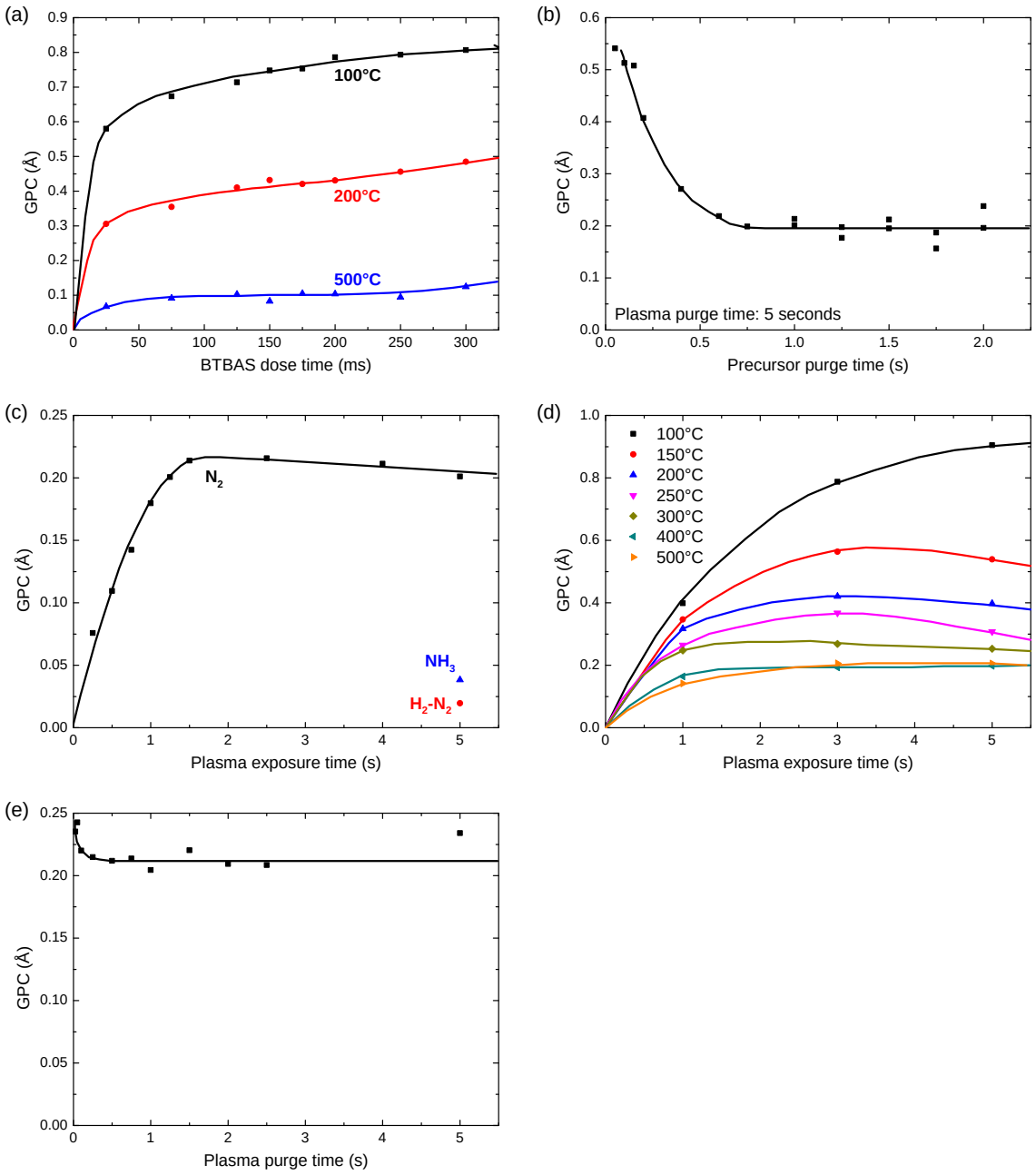

Figure 4.1: The saturation curves for the silicon nitride process, showing the variation of (a) the precursor dosing time (condition B), (b) the precursor purge time (condition A), (c) the plasma exposure time (condition A), (d) the plasma exposure time for various temperatures (condition B) and (e) the plasma purge time (condition A). For all graphs the plasma is a nitrogen plasma, but in (c) the GPC for depositions with NH_3 and H_2-N_2 plasmas is plotted as well. The temperature was 350°C, unless stated otherwise, and note that the plasma purge time in (b) was 5 seconds instead of 1 second. All lines serve as a guide to the eye.

seconds, as shown in figure 4.1c. Therefore, the process investigation was continued with a N_2 plasma. An explanation for the reduction in GPC for hydrogen-containing plasmas will be addressed in section 5.3.

For the standard recipe, that will be shown in section 4.1.3, the step times determined from the saturation curves were 5 seconds for the N_2 plasma exposure time and 1 second for both purge times (see table 4.2). The purge times were chosen longer than necessary for saturation to avoid CVD-like growth at other temperatures. The plasma exposure time was chosen longer because the saturation curve at low temperatures did not show saturation for a plasma exposure time of 1.5 seconds. For the following experiments a precursor dosing time of 200 ms was chosen, because for longer dosing times longer purge times were required.

4.1.2 Plasma exposure parameters

After determination of the duration of the process steps, the plasma conditions were optimized further. This was done at a temperature of 350°C and because the GPC saturated for plasma exposure times of 1.5 seconds at 350°C, these experiments were performed with this plasma exposure time to shorten the deposition time. For all other parameters condition A in table 4.1 applied.

Figure 4.2a shows the GPC as a function of the N_2 plasma flow rate. There was only a slightly higher GPC for N_2 flow rates between 40 and 50 sccm (standard cm^3/min). However, for the standard recipe a N_2 flow rate of 100 sccm was chosen, which was the maximum flow that was allowed by the N_2 mass flow controller. This was done because the higher the flow rate, the more the butterfly valve of the reactor was opened. The more the butterfly valve was opened, the shorter the residence time, because particles were pumped away faster, limiting redeposition of reaction products (i.e., reaction products can interact with the plasma, resulting in the formation of new species that can deposit on the surface again [23]).

The influence of the plasma pressure is shown in figure 4.2b. Pressures between 40 mTorr and 55 mTorr resulted in the highest GPC and therefore 40 mTorr was chosen to be the standard plasma pressure. In section 4.2.3 it will be shown that the film quality improved for lower pressures, which implies that a pressure below 40 mTorr would be a better choice. However, the lower the pressure, the higher the energy of the ions impinging on the surface. Thus a plasma pressure of 40 mTorr could be a good compromise when the ion energy is an issue.

Figure 4.2c shows an increasing GPC for an increasing plasma power. Therefore, the maximum plasma power allowed on the system, 600 W, was chosen for the standard recipe.

4.1.3 Standard recipe

The deposition parameters of the standard process are listed in table 4.2. The deposition temperature was 200°C, because a compromise was made between high GPC and short cycle time. The lower the temperature, the higher the GPC. However, at a temperature of 200°C there was still saturation for a plasma exposure time of 5 seconds, which was not the case for a temperature of 100°C. The BTBAS dosing time was reduced to 150 ms, because optimization of the dosing step and the consecutive reaction step resulted in more efficient use of the precursor (by diverting the argon flow to the exhaust during precursor dosing and setting the angle of the butterfly valve to 10° in the reaction step).

Depositing 1100 cycles with this recipe resulted in a GPC of 0.33 Å and a film with a refractive index of 1.76 (at 2 eV). Figure 4.3 shows the XPS depth profile of this film. The N/Si ratio was 1.87, while that for stoichiometric Si_3N_4 is 1.33. The high N/Si ratio is

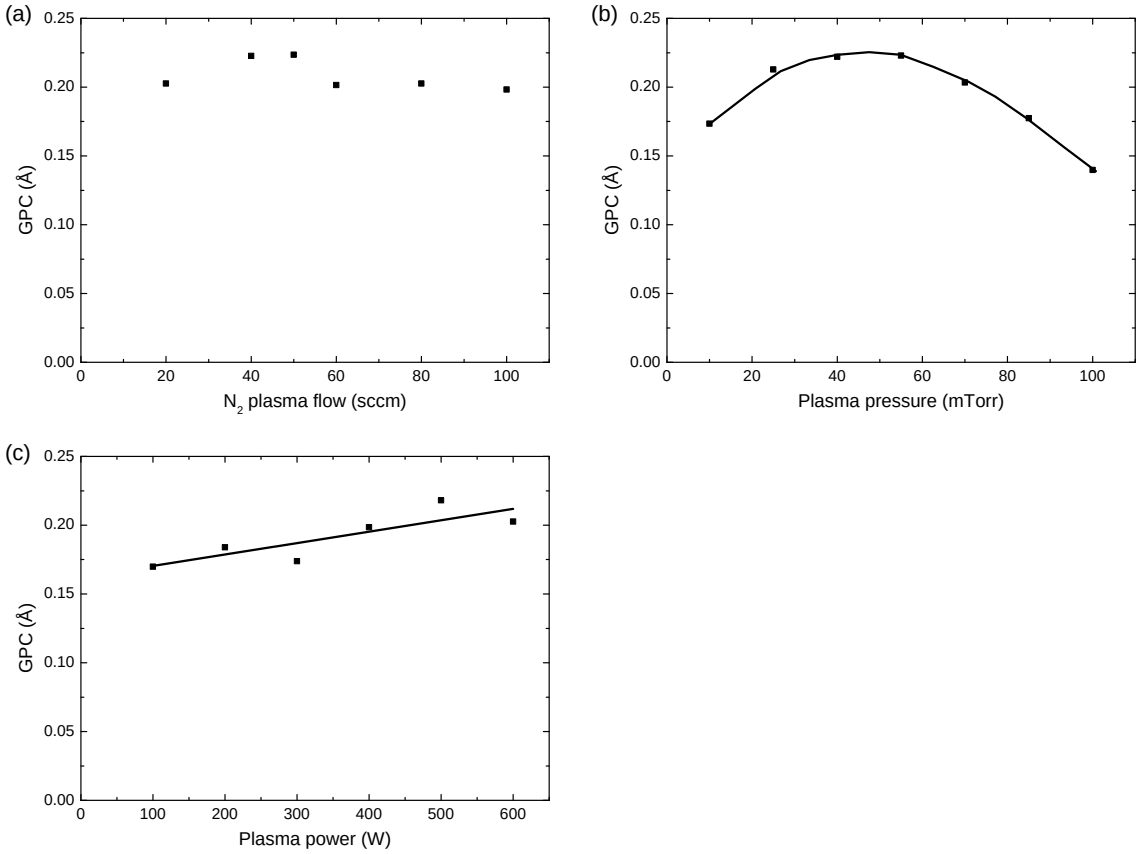

Figure 4.2: The GPC as a function of (a) the N_2 plasma flow, (b) the plasma pressure and (c) the plasma power. Depostion condition A applied, except for the plasma exposure time, which was set to 1.5 seconds. All lines serve as a guide to the eye.

Table 4.2: The deposition parameters for the standard recipe. These conditions were used throughout the rest of this work unless mentioned otherwise.

Deposition parameter	Standard condition
Temperature (°C)	200
BTBAS dosing time (ms)	150
Precursor purge time (s)	1
Plasma exposure time (s)	5
N_2 plasma flow (sccm)	100
Plasma pressure (mTorr)	40
Plasma power (W)	600
Plasma purge time (s)	1

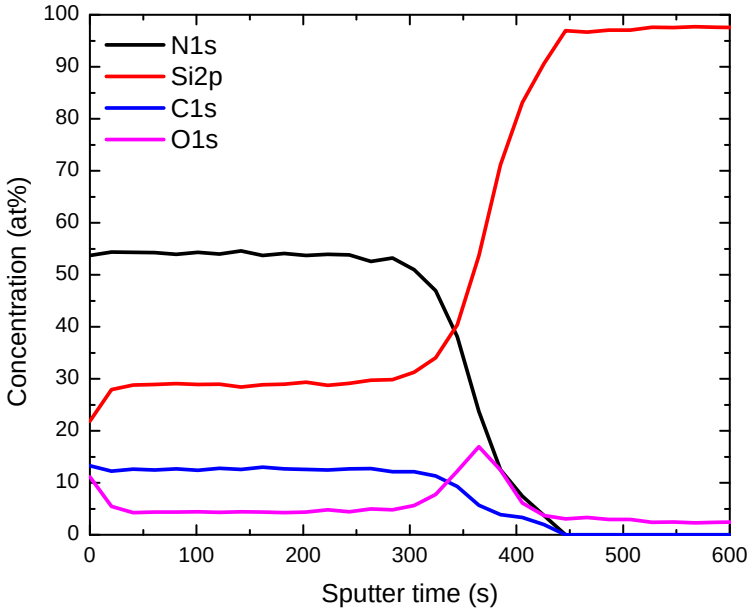

Figure 4.3: The XPS depth profile for a film deposited with the standard recipe. The film was sputtered within approximately 300 seconds, after which the native oxide and the substrate were sputtered.

remarkable, because for silicon nitride deposited with PECVD it is not possible to obtain N/Si ratios higher than 1.4, but the high ratio will be confirmed by RBS measurements later in this work. The carbon and oxygen contents were approximately 12.6 at% and 4.4 at% respectively. However, as explained in section 2.3.4, sputtering could lead to penetration of oxygen, resulting in a measured oxygen content that was higher than the actual oxygen content in the film. Since XPS resulted in a non-zero oxygen content in the substrate (which should not contain any oxygen), the oxygen content of the film was probably less than the 4.4 at% shown in figure 4.3.

4.1.4 Initial growth

Initial growth is an issue for some ALD processes and was therefore studied in this work as well. In the previous chapter it was already mentioned that it was difficult to study the initial growth of the films due to the influence of a plasma on the thickness and composition of the native oxide layer. As soon as the deposition started it was impossible to differentiate between changes in the native oxide layer and thickness of the film.

However, when the film thickness was fitted as a function of the number of deposition cycles a small intercept of approximately 0.4 nm was needed, indicating an enhanced initial growth. When the deposition was done on a wafer that was immersed in a 1% HF solution for one minute to remove the native oxide, this intercept was approximately 2 nm (an example of the data for deposition on an HF-dipped wafer is shown in appendix B). The difference between these intercepts is most probably due to the fact that the wafers with native oxide were treated with a N_2 plasma before the deposition started, which already resulted in a

change in thickness and properties of the native oxide layer, while the HF-dipped wafers were not subject to a plasma treatment and the first cycles might then have resulted in a thickness increase and change of properties due to nitridation.

4.2 Characterization of silicon nitride films

In this section the properties of the deposited films as a function of three deposition parameters will be discussed: plasma exposure time, deposition temperature and plasma pressure. These deposition parameters were varied and for each condition investigated a separate wafer was used to enable *ex situ* measurements of the resulting film. Before the deposition, each wafer was exposed to a N_2 plasma (600 W, 40 mTorr, 100 sccm) for 1 minute as pre-treatment.

The film properties were analyzed with *in situ* and *ex situ* SE, XPS, RBS and ERD. Although the process was monitored with *in situ* SE and the initial growth was investigated with this technique, the GPC was determined by dividing the thickness measured with *ex situ* SE by the total number of deposition cycles. Note that XRD measurements showed that all films were amorphous (data not shown).

4.2.1 Plasma exposure time series

The saturation curves for plasma exposure time at different temperatures (figure 4.1d) showed an increasing GPC for increasing plasma exposure time until the maximum GPC was reached and a decreasing GPC for even longer plasma exposure times. Furthermore, figure 4.3 showed a relatively high carbon content. It was expected that less carbon would be incorporated in the films when longer plasma exposures were used and the lower GPC was due to the carbon removal. To study these effects, a plasma exposure time series was performed. The standard recipe (table 4.2) was used and the plasma exposure time was the only parameter that was varied.

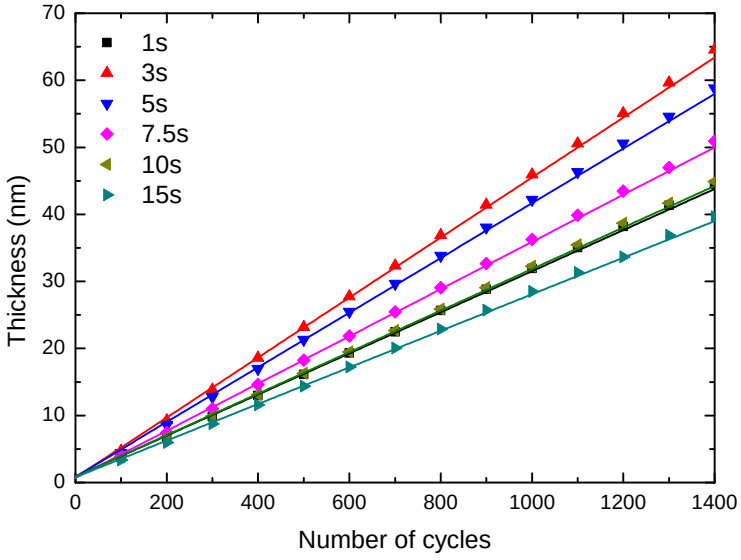

Figure 4.4: The thickness as a function of the number of cycles for varying plasma exposure times measured with *in situ* SE. The lines are linear fits of the data.

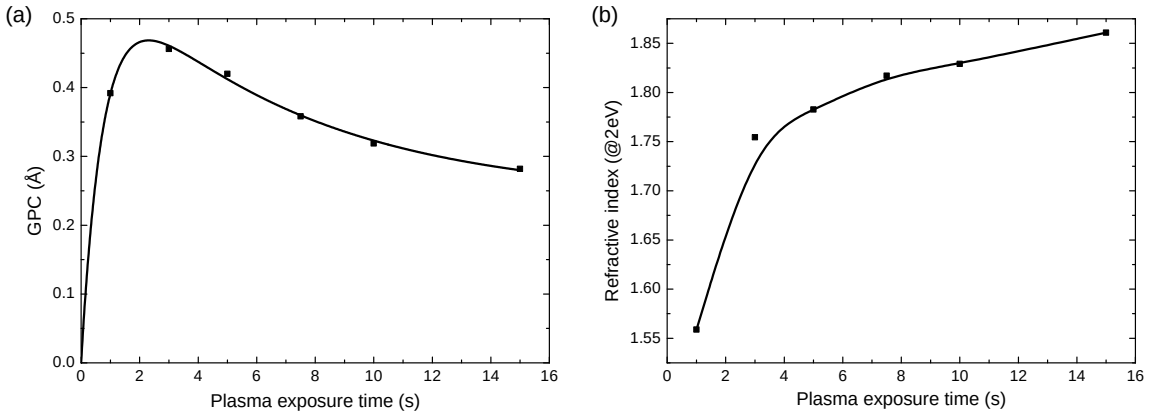

Figure 4.5: (a) The GPC as a function of plasma exposure time. The black line corresponds to the fit GPC $= 0.60 \cdot \left(1 - e^{-t/0.76}\right) + 0.36 \cdot \left(e^{-t/6.76} - 1\right)$ with t the plasma exposure time in seconds. (b) The refractive index (at 2 eV) as a function of plasma exposure time. The black line serves as a guide to the eye.

The *in situ* SE data in figure 4.4 show the thickness as a function of the number of deposition cycles for a variation of plasma exposure time. There was no growth delay, but a small enhancement in the first cycles, as already mentioned in section 4.1.4. The thickness increased linearly with the number of cycles, which is shown by the linear fits.

Figure 4.5a shows the GPC as a function of the plasma exposure time and a fit of the results with two exponents, because the GPC showed two different time scales: one for the increase of the GPC for short plasma exposure times and one for the decrease of GPC for longer exposure times. The GPC increased for plasma times increasing up to approximately 2.3 seconds with a time constant of 0.76 seconds and then decreased with a time constant of 6.76 seconds towards saturation for longer plasma exposure times. This might be due to a modification of the material. Calculated from the fit, the saturated GPC would be 0.24 Å for plasma exposure times of 45 seconds and longer.

The refractive index for these films is plotted in figure 4.5b. For short plasma exposure times the refractive index increased rapidly, for plasma exposure times between 5 and 15 seconds it increased more slowly for increasing plasma exposure time.

Figure 4.6 shows the impurity content of the deposited films. The XPS content was determined from the depth profiles of each film. These profiles can be found in appendix C.1. As expected, the carbon content decreased for longer plasma exposures, while the oxygen content increased a little. For RBS and ERD there is only data for 10 second and 15 second plasmas. The concentrations were not directly comparable to those of XPS because hydrogen was also included in the calculation of the percentages for RBS and ERD. However, the concentrations seemed to follow the same trends. Morin *et al.* reported a decrease in hydrogen content for increasing exposure of PECVD silicon nitride films to N_2 plasmas, which corresponds to the observed hydrogen trend for the ALD films in figure 4.6 [39]. The hydrogen concentration seemed to follow the carbon trend. Even though concentrations were not directly comparable for XPS and RBS, the N/Si ratios were. These ratios are plotted in figure 4.7. The N/Si ratios were relatively high compared to PECVD silicon nitride films that result in N/Si ratios of 1.4 at the maximum, but the XPS ratios were confirmed with RBS. RBS resulted in even higher N/Si ratios than XPS, but the closer the films were to a stoichiometric Si_3N_4 composition, the better the RBS and XPS N/Si ratios corresponded.

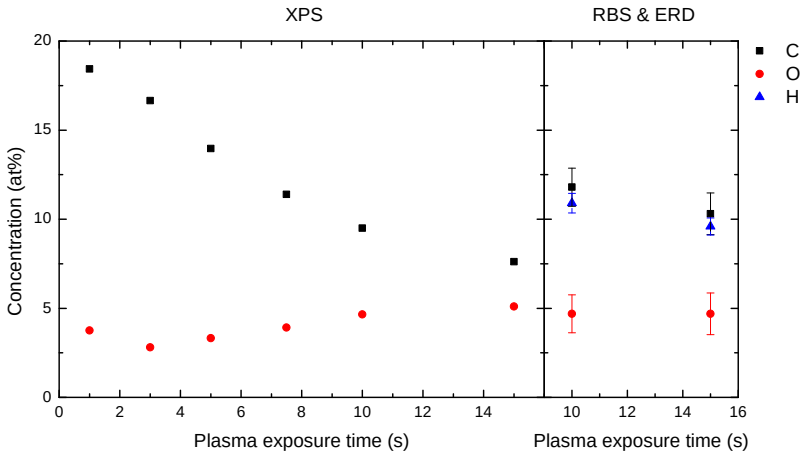

Figure 4.6: The graph on the left shows the carbon and oxygen contents measured with XPS. The graph on the right shows these contents measured with RBS and the hydrogen content determined by ERD. It was difficult to determine the error in the XPS measurements, as explained in section 2.3.4.

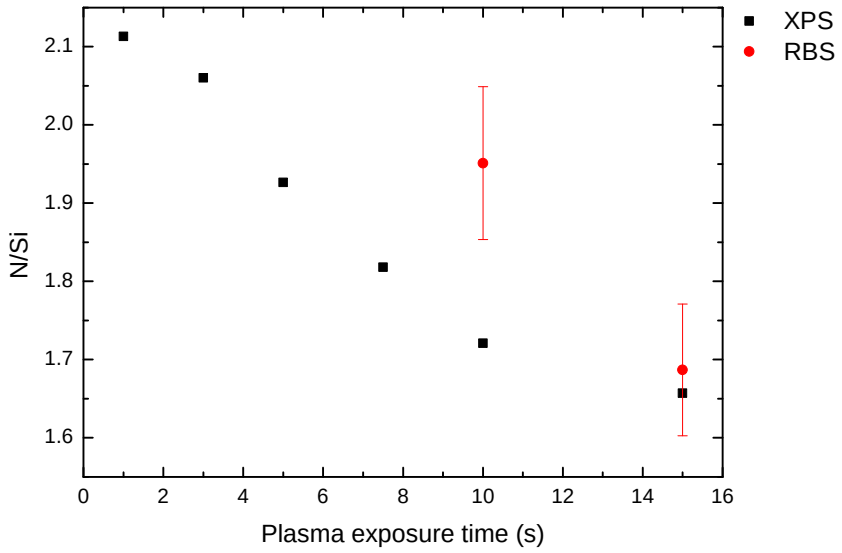

Figure 4.7: The nitrogen over silicon ratios measured with XPS and RBS as a function of the plasma exposure time.

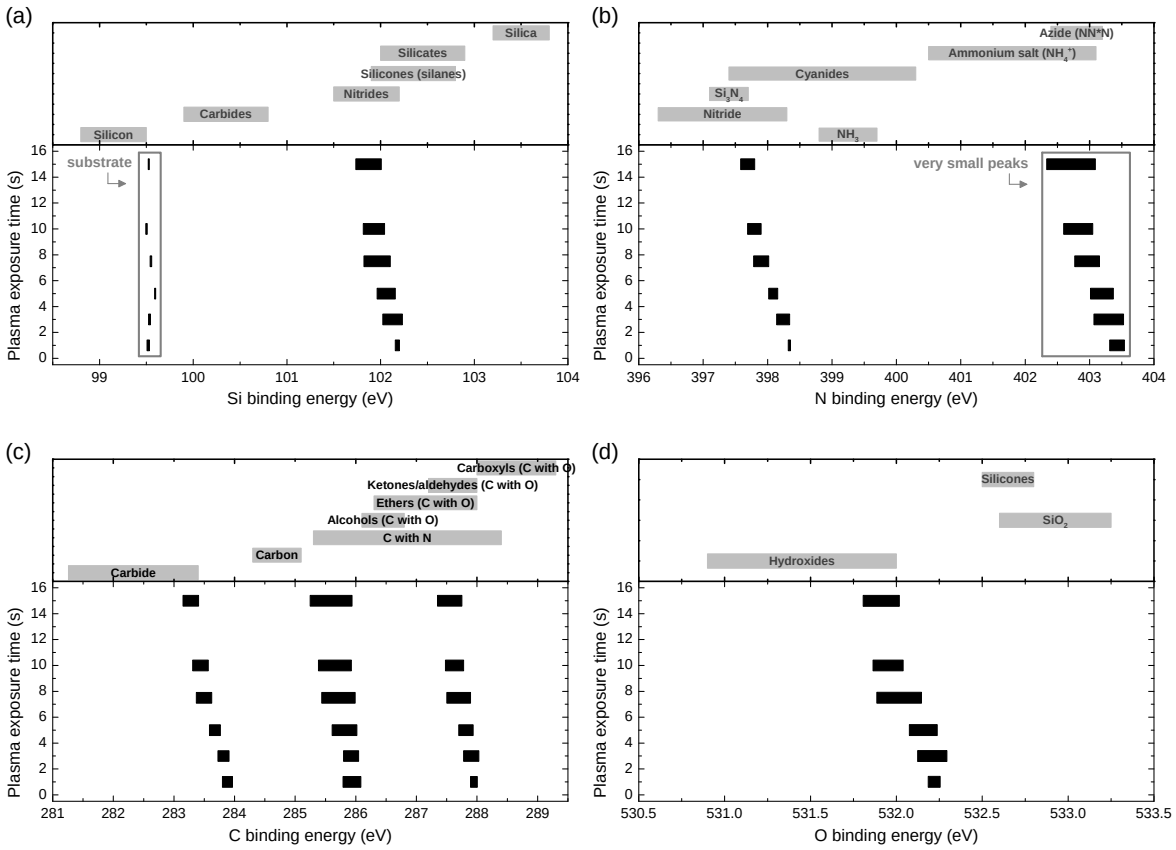

Figure 4.8: The binding energies of the elements (a) silicon, (b) nitrogen, (c) carbon and (d) oxygen and the reference values for the investigated ranges from the NIST X-ray Photoelectron Spectroscopy database [25]. The width of the bars indicates the range in which the binding energy for a specific peak occurs.

The binding energies for the four elements measured with XPS are shown in figure 4.8 and compared to the values of the NIST X-ray Photoelectron Spectroscopy database [25]. The silicon binding energy showed two ranges of interest. The first one for a binding energy around 99.5 eV, corresponding to silicon-silicon bonds in the substrate, the second one, around 102 eV, corresponded to silicon-nitrogen bonds, which could also be observed in the nitrogen binding energy. The number of silicon-nitrogen bonds in the films increased for increasing plasma time (as shown in the areas of the deconvoluted peaks in appendix C.1), which was also shown by Morin *et al.* [39]. The peaks around 403 eV in the nitrogen binding energy had a very low intensity, which made it difficult to determine their position exactly. The carbon in the films was bonded to silicon (carbides), carbon and nitrogen. The binding energies of silicon and nitrogen did not show this possibility, because the amount of carbon incorporated in the films was small. Because of this, the peaks of silicon and nitrogen bonded to carbon were negligible compared to the silicon-nitrogen peaks. The oxygen binding energy showed that the oxygen was bonded in hydroxides. The fact that carbon and oxygen concentrations showed opposite trends (see figure 4.6) made it unlikely that the oxygen was bonded to carbon, even though the $-$COH groups are in the right range of binding energy. The most probable explanation is that oxygen was included in the films due to reactor impurities and impurities in the gases.

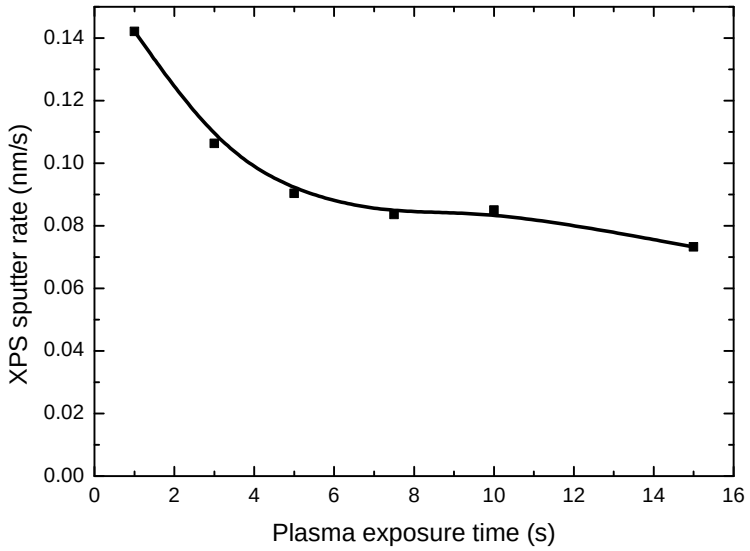

Figure 4.9: The XPS sputter rate as a function of the plasma exposure time. The black line serves as a guide to the eye.

For all elements, the binding energy of each bond shifted towards lower binding energies for longer plasma exposures. The XPS data showed an increase in silicon content and a decrease in carbon content for increasing plasma time. Since silicon is less electronegative than carbon, the environment became less electronegative, explaining the shift towards lower binding energies for longer plasma exposure times. Because the film quality improved for increasing plasma time, a negative shift in binding energies could be taken as an improvement of film quality, as will be shown in section 4.2.2 and 4.2.3.

The XPS sputter rate decreased with increasing plasma exposure time, as is shown in figure 4.9. This could indicate a change of composition and/or a densification of the material. The latter was reported by Morin *et al.* for increasing N_2 plasma treatment times of silicon nitride films [39]. Both effects could also explain the decreasing GPC for increasing plasma exposure time. Figures 4.6 and 4.7 showed a difference in composition between the 10 and 15 second plasmas, while the mass density, as determined by RBS, increased from 2.2 g/cm^3 for a 10 second plasma to 2.4 g/cm^3 for a 15 second plasma, indicating densification of the film for longer plasma exposure times.

For the following series a plasma exposure time of 10 seconds was chosen as a compromise between the duration of the deposition process and the properties of the films.

4.2.2 Temperature series

One of the goals of this work was the deposition of silicon nitride in a wide temperature window. In order to investigate the material properties for various temperatures a temperature series was deposited. The temperature was varied between 100°C and 500°C. It is important to remember that the temperatures mentioned are the setpoint temperatures, which can deviate significantly from the actual wafer temperature, as shown in chapter 3. Also, at room temperature depositions were performed in a related project [40]. These depositions also

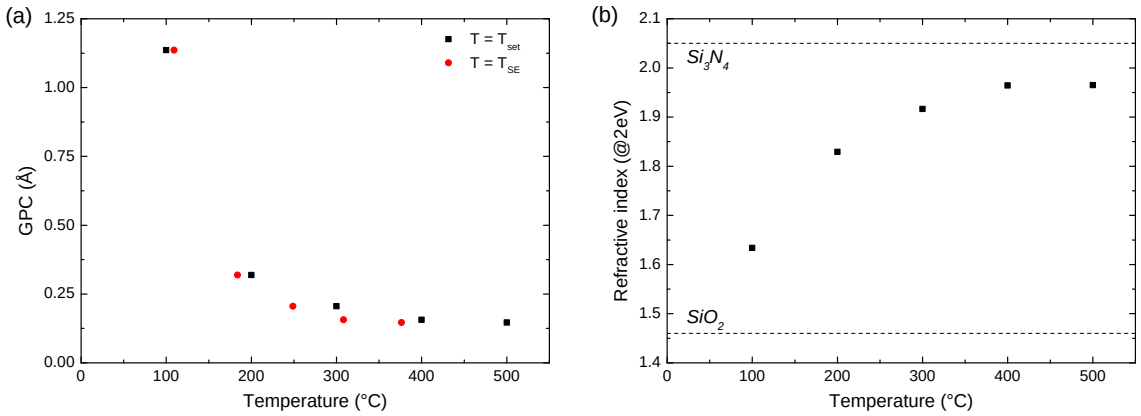

Figure 4.10: (a) The GPC as a function of the setpoint temperature and the substrate temperature measured with *in situ* SE. (b) The refractive index as a function of the setpoint temperature. The dashed lines indicate the refractive indices of bulk Si_3N_4 and SiO_2 [16].

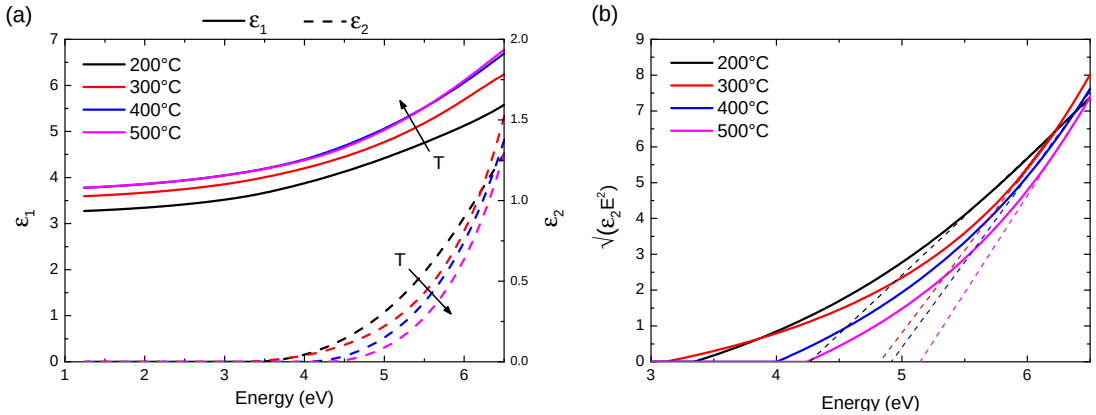

Figure 4.11: The optical constants as a function of photon energy (a) and the corresponding Tauc plots (b) for deposition temperatures between 200°C and 500°C. The dashed lines in (b) indicate the extrapolation of the linear parts of the Tauc plots.

showed the saturation curves that are typical for ALD, but that work is outside the scope of this report and therefore these results will not be shown.

In figure 4.10a the GPC is shown as a function of the temperature. The GPC decreased for increasing temperature for temperatures up to 500°C. Even though the setpoint temperature covered the range between 100°C and 500°C, the actual temperature window was not so wide. The substrate temperatures measured with *in situ* SE after the plasma treatment ranged from 109°C to 376°C. Note that data reported by O'Neill *et al.* suggests that BTBAS decomposes for temperatures above 500°C [41].

The refractive index of the deposited films is shown in figure 4.10b. It increased for increasing temperature and stabilized at a value of 1.96 for temperatures of 400°C and higher. The optical constants and corresponding Tauc plots are shown in figure 4.11. By extrapolation of the linear part of the Tauc plots the band gap could be obtained by determining the intercept with the x-axis, which shows an increasing band gap for increasing deposition temperature. The higher the temperature, the closer the band gap was to that of stoichiometric

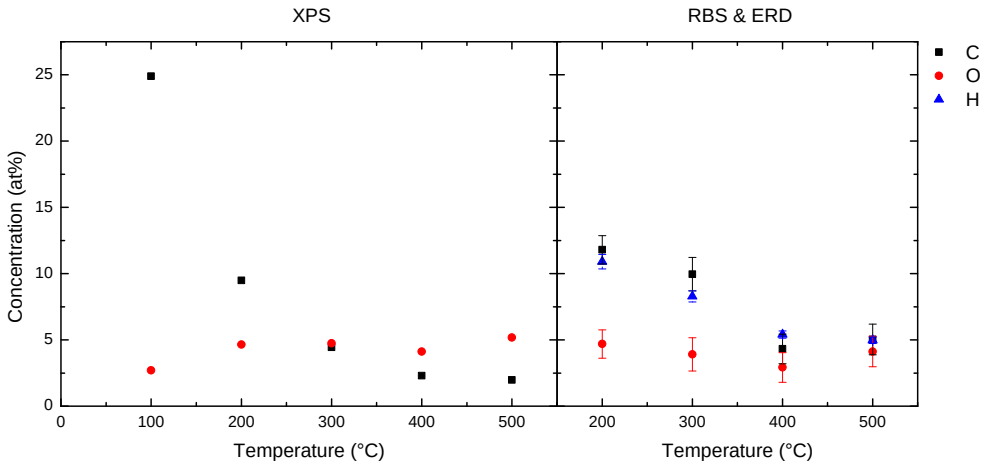

Figure 4.12: The concentration of impurites as a function of temperature measured by XPS (left) and RBS and ERD (right).

Si_3N_4, which is $\sim$5 eV [16].

The XPS depth profiles from which the composition was determined can be found in appendix C.2. The impurity content of the films, as determined by XPS, RBS and ERD, is shown in figure 4.12. For increasing temperatures the carbon and hydrogen content decreased and the oxygen content remained approximately constant. The XPS and RBS and ERD results are not directly comparable, because for RBS and ERD the hydrogen concentration was measured and calculated as well. When the RBS data was recalculated neglecting the presence of hydrogen, the values of RBS could be compared with those of XPS (data not shown). The RBS and XPS concentrations showed the same trends, but the carbon content was higher for the RBS measurements. From the XPS depth profiles (appendix C.2) it is known that there was more carbon at the surface of the film than in the bulk and therefore only the average bulk concentration was plotted in the XPS composition plots, while with RBS modelling the carbon content of the whole film (the accumulated carbon at the surface included) was determined, leading to a higher carbon concentration for RBS. The ratio of nitrogen to silicon is shown in figure 4.13 and shows a decrease towards stoichiometric Si_3N_4 for increasing substrate temperatures. The RBS and XPS values corresponded very well to each other for temperatures of 300°C and higher.

The binding energies of the elements silicon, nitrogen, carbon and oxygen were determined by XPS. A comparison of these values with values from the NIST X-ray Photoelectron Spectroscopy database [25] and the areas of the deconvoluted peaks are shown in appendix C.2. The silicon and nitrogen in the film were mainly bonded in silicon-nitrogen configurations and the oxygen was incorporated due to impurities in the reactor and the gases. For temperatures of 100°C and 200°C the carbon could be bonded to silicon, nitrogen and carbon. For higher temperatures the carbon-carbon peak disappeared, which indicates a better *t*-butylamine ligand removal. The binding energy of nitrogen for the film deposited at 100°C was shifted towards higher binding energy compared to the other temperatures due to a more electronegative environment at 100°C, since there was more carbon and less silicon in the film.

Figure 4.14a shows the sputter rate determined by XPS. It shows a decreasing sputter rate for an increasing temperature, which might indicate a densification of the film and/or a change

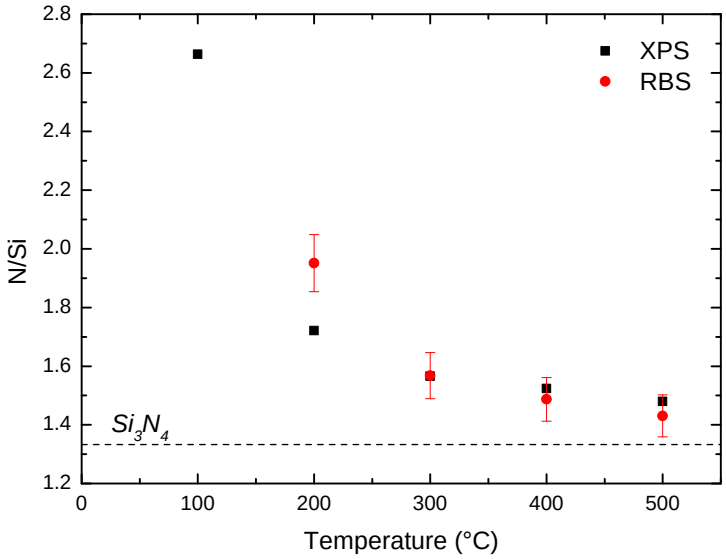

Figure 4.13: The N/Si ratio as a function of temperature for XPS and RBS. There was no RBS data for the deposition at 100°C. The dashed line indicates the N/Si ratio for stoichiometric Si_3N_4.

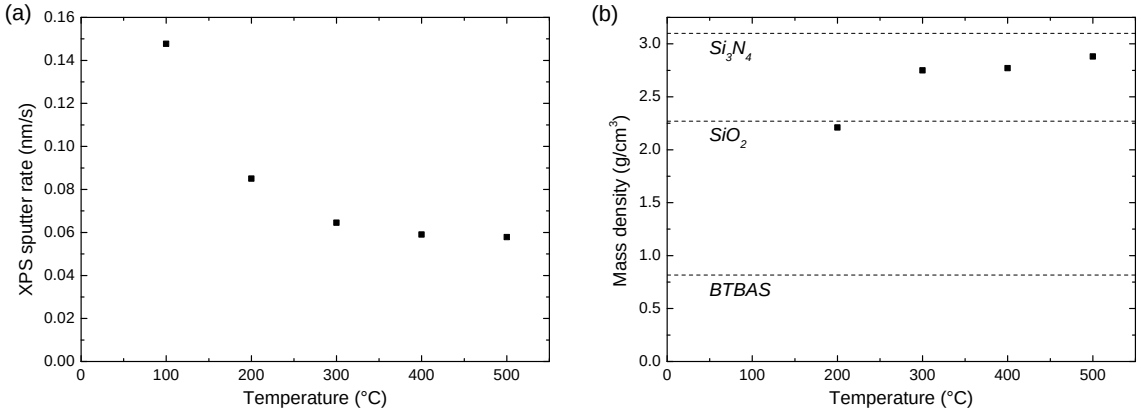

Figure 4.14: The XPS sputter rate (a) and the mass density (b) as a function of temperature. The dotted lines indicate the mass density of bulk stoichiometric Si_3N_4, SiO_2 and BTBAS [16, 42].

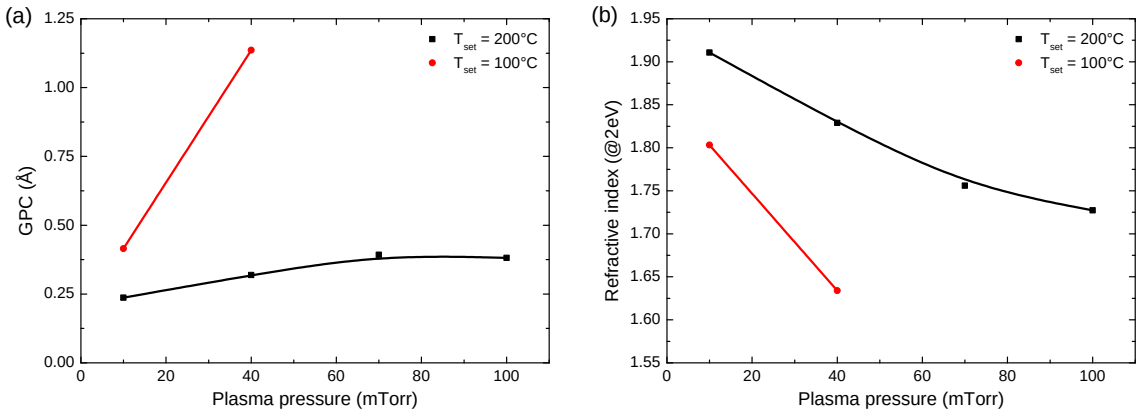

Figure 4.15: The GPC (a) and refractive index (b) as a function of plasma pressure for a temperature of 100°C and 200°C. All lines serve as a guide to the eye.

in composition of the material. Figures 4.12 and 4.13 showed the change in composition and figure 4.14b shows the mass density as a function of temperature as measured with RBS. The mass density increased for increasing temperature towards the mass density of stoichiometric Si_3N_4 (3.1 g/cm^3 [16]), confirming the densification of the material.

4.2.3 Plasma pressure series

For the pressure series the standard condition was used with a plasma exposure time of 10 seconds. The standard plasma pressure chosen before was 40 mTorr, because this resulted in the highest GPC. However, the conditions with the highest GPC not necessarily resulted in the best quality films, as observed for the plasma exposure time series. Therefore the plasma pressure was varied. The material properties of a film deposited at 100°C (higher carbon content compared to 200°C) might also be improved by using a lower plasma pressure, which was investigated for a pressure of 10 mTorr.

Figure 4.15a shows the GPC as a function of plasma pressure for depositions at 100°C and 200°C. The GPC decreased for decreasing plasma pressure for both temperatures, but the change was much larger for a deposition temperature of 100°C.

The refractive index as a function of plasma pressure is plotted in figure 4.15b for both temperatures. It increased for decreasing plasma pressure and again, the largest change was observed for a deposition temperature of 100°C.

The composition of the films was determined by XPS (the depth profiles can be found in appendix C.3) and the impurity content is shown in figure 4.16. The oxygen concentration hardly changed, while the carbon content decreased for decreasing pressure. The N/Si ratio, shown in figure 4.17a, decreased for decreasing plasma pressure. The sputter rate is plotted in figure 4.17b and showed a decrease for decreasing plasma pressure. Again, this could indicate a change in density and/or composition. Figures 4.16 and 4.17a showed the change in composition. The mass densities of these films were not measured and therefore densification could not be confirmed, but it is likely that the films grew denser for decreasing pressure.

The binding energies (see appendix C.3 for a comparison with the NIST X-ray Photoelectron Spectroscopy database [25]) show that silicon and nitrogen were mainly bonded to each other. Some carbon was bonded to silicon and nitrogen as well. The carbon-carbon bond was present for all pressures, except for 10 mTorr at 200°C, which suggests a better

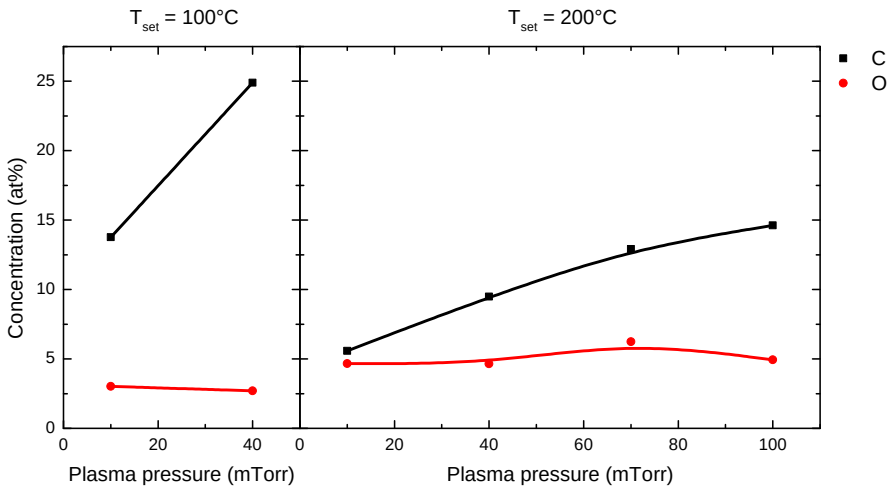

Figure 4.16: The impurity content, measured with XPS, as a function of plasma pressure for a temperature of 100°C and 200°C. All lines serve as a guide to the eye.

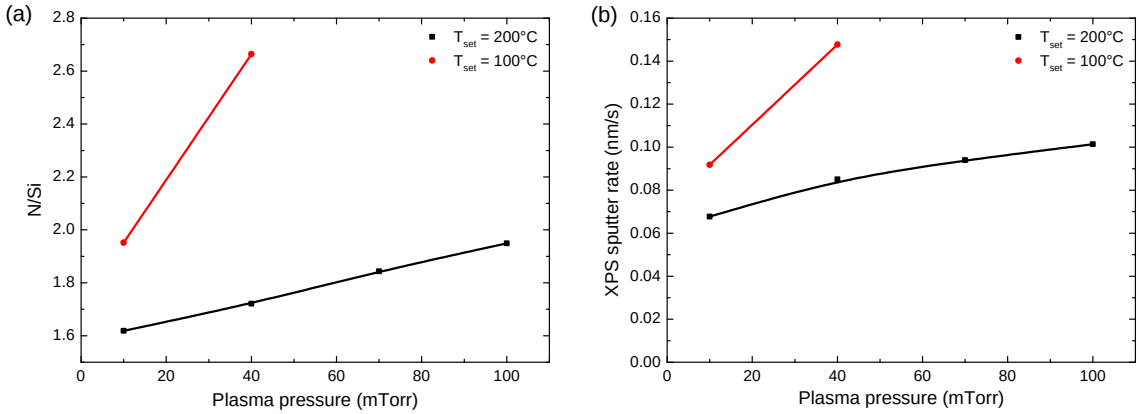

Figure 4.17: (a) The N/Si ratio as determined by XPS. (b) The XPS sputter rate as a function of plasma pressure. The lines serve as a guide to the eye.

t-butylamine ligand removal at these conditions. The shift towards lower binding energies, which indicates material improvement, was observed for decreasing plasma pressure.

4.2.4 Stability

For some films the XPS composition and the refractive index did not seem to correspond, e.g., the film deposited with a plasma exposure time of 1 second, which could indicate that post-oxidation occurred in these films. Post-oxidation would mainly affect the *ex situ* SE measurements, because these measurements were done approximately half an hour after the sample was removed from the reactor, while the sample was transferred to the XPS within a few minutes. The GPC and XPS sputter rate of films that oxidized relatively fast were also influenced, because they were determined by dividing the thickness that was measured with *ex situ* SE by the total number of deposition cycles or the sputter time. This thickness sometimes increased due to oxidation and oxidized films were sputtered faster than non-oxidized films.

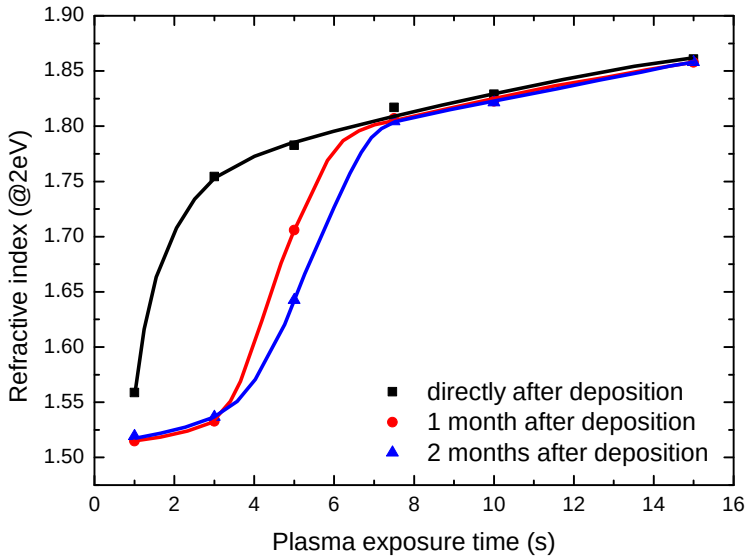

Figure 4.18: The refractive index as a function of plasma exposure time for as-deposited films compared to those of the same films 1 month and 2 months after deposition.

To investigate the (long-term) stability of the films they were measured again with *ex situ* SE, 1 month and 2 months after deposition. The refractive index of a film could already indicate whether the film had changed or not, because oxidation of the film would lead to a decrease in refractive index towards ~ 1.46 for SiO_2 [16]. Some of the films were also measured again with XPS to see whether the composition had changed.

The XPS depth profile of the film deposited with a plasma exposure time of 1 second (see appendix C.1) already shows a higher oxygen content at the surface than the other films in the same series, indicating that post-oxidation occurred in a relatively short time after removal from the reactor, explaining the low refractive index for the film shown in figure 4.5b. To investigate whether post-oxidation occurred, the refractive indices after 1 month and 2 months after deposition were compared to the refractive indices directly after the deposition for the plasma exposure time series in figure 4.18. The films deposited with plasma exposure times up to 5 seconds show a decrease in refractive index over time, indicating that post-oxidation occurred, while the longer plasma exposure times resulted in stable films. To confirm the change in composition, the XPS depth profiles measured directly after deposition and 1 month later for a 3 second and a 15 second plasma are shown in figure 4.19. For a 3 second plasma exposure an increase in oxygen content was clearly seen, while for a plasma of 15 seconds there was only a slight increase in oxygen concentration at the surface of the film.

In the temperature series the film deposited at 100°C was the only film that oxidized directly after deposition. The corresponding XPS depth profile (appendix C.2) shows an oxidation front directly after deposition. The refractive indices for all films in figure 4.20 only show a slight decrease, which was probably caused by a little surface oxidation.

The refractive indices of the plasma pressure series (figure 4.15b) show no fast post-oxidation except for the film deposited at 100°C and 40 mTorr, which is the same film as in the temperature series. Figure 4.21 shows that the films deposited at 70 mTorr and 100 mTorr at 200°C oxidized within a month after deposition, while the films at 10 mTorr and

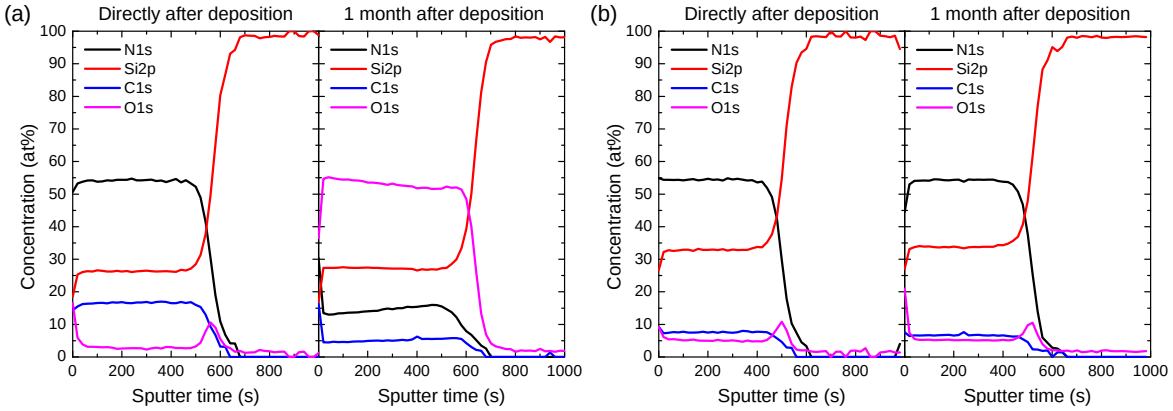

Figure 4.19: The XPS depth profiles measured directly after deposition and 1 month after deposition for a film deposited with a plasma exposure time of (a) 3 seconds and (b) 15 seconds.

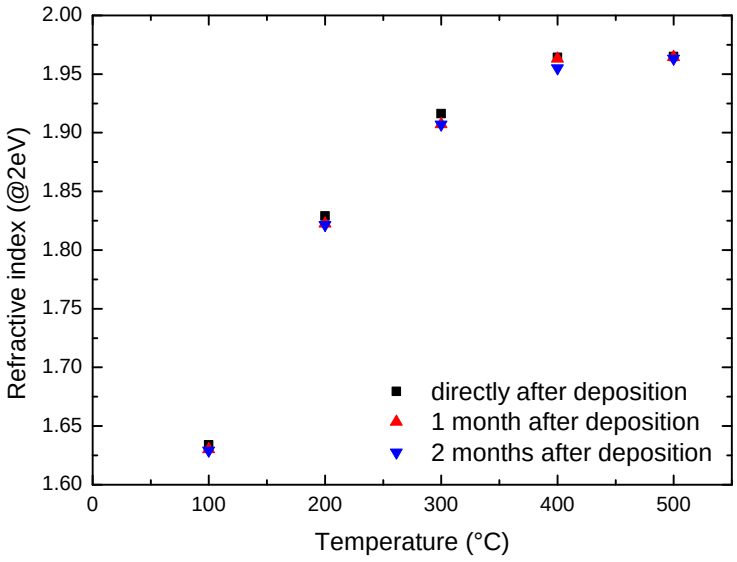

Figure 4.20: The refractive index as a function of setpoint temperature for as-deposited films compared to those of the same films 1 month and 2 months after deposition.

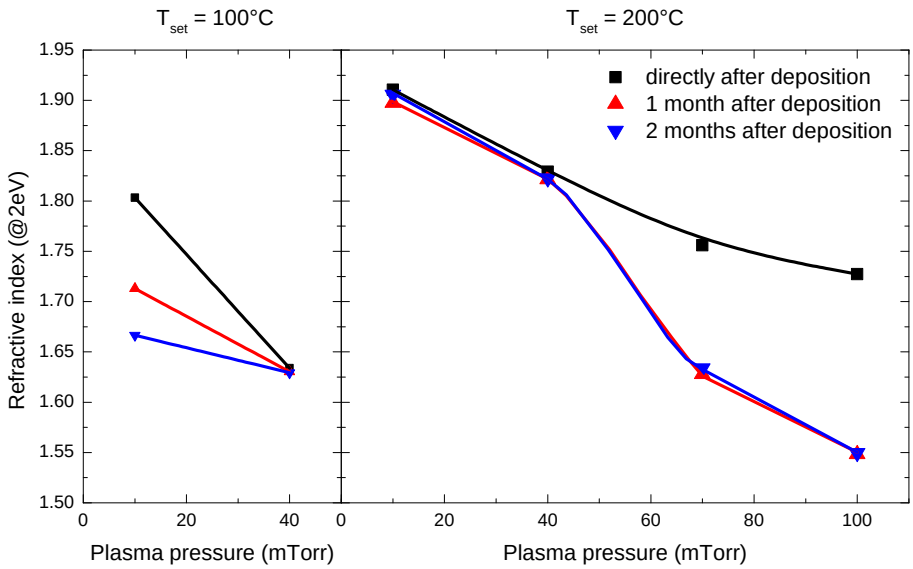

Figure 4.21: The refractive index as a function of plasma pressure for as-deposited films compared to those of the same films 1 month and 2 months after deposition. All lines serve as a guide to the eye.

40 mTorr hardly oxidized. The films deposited at 100°C both oxidized after deposition, the film deposited at 40 mTorr very rapidly, because it already had a low refractive index directly after deposition, while the film deposited at 10 mTorr oxidized slowly after deposition and its refractive index decreased slower than the unstable films deposited at 200°C. In appendix C.3 the development of an oxidation front is shown.

In conclusion, the films with low carbon content and a N/Si ratio close to stoichiometric Si_3N_4 also resulted in the most stable films and the stability could be determined by *ex situ* SE measurements of the refractive index. Also, stable films showed some oxidation of the surface, but no increased amount of oxygen in the bulk of the film.

4.2.5 Uniformity of thickness and refractive index

The uniformity of the thickness and refractive index of the films was determined with SE mapping software on half 4-inch wafers. Figure 4.22 shows the film thickness across the wafer deposited with a plasma exposure time of 10 and 15 seconds. The non-uniformity is mentioned in the upper left corner of each plot and is defined as

$$\text{Non-uniformity} = \frac{\sigma}{\text{average thickness}} \cdot 100\%, \tag{4.1}$$

where σ is the standard deviation. At each data point the measured thickness was divided by the average film thickness. The thickness uniformity of both films was excellent and for long plasma exposure times the uniformity was stable.

The thickness uniformity of the films deposited at different temperatures is shown in figure 4.23. For all but the film deposited at 100°C the non-uniformities were good. At low temperatures a longer plasma exposure time was needed to achieve saturation, which explains why the film at 100°C was less uniform. Furthermore, because the film deposited at 100°C was already oxidized and since the model used was a model for SiN_x, the modelling was not accurate for this film, because it contained so much oxygen that it was more like

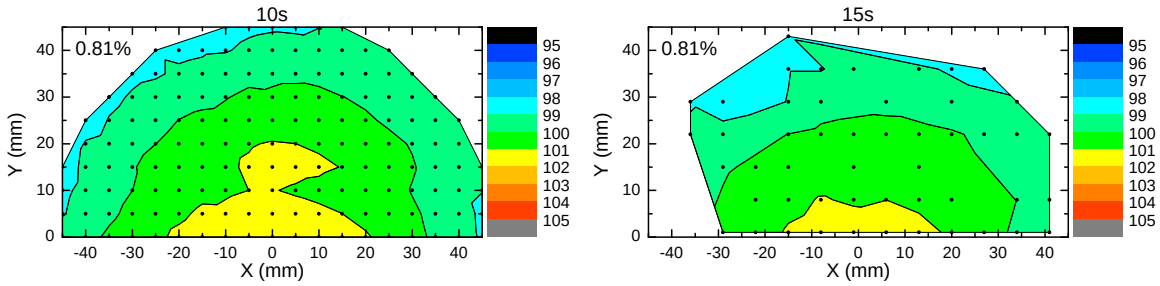

Figure 4.22: The film thickness across the wafer relative to its average thickness for films deposited with 10 second and 15 second plasma exposures. The black dots indicate the data points and the percentages in the graphs are the non-uniformities.

SiO_2, resulting in high modelling errors. The non-uniformities are plotted as a function of deposition temperature in figure 4.24, which shows an improvement in the uniformity for increasing deposition temperature. The only film that did not fit into this trend was the film deposited at 200°C. However, this film was deposited in a different run, 1 month before the other films in this series. A different batch of BTBAS was used and the reactor conditions could have been different. The thickness uniformity might thus be sensitive to the reactor conditions. Therefore, the thickness uniformity at 200°C was considered a 'bad' data point in the uniformity of the temperature series and an interpolated non-uniformity data point was added in the graph for this temperature. This effect was only visible in the uniformity, while for other trends (e.g., GPC, refractive index and composition) this film followed the trend of the other samples. This interpolated value for the non-uniformity was also used to make a fair comparison with the uniformities of the films deposited at different plasma pressures, because these were deposited in the same run as the temperature series.

The non-uniformity of the film thickness across the wafer deposited at 200°C with a plasma pressure of 10 mTorr was 0.84% (see appendix D.1 for the thickness across the wafer), which was less than the interpolated non-uniformity of 2.44% at 40 mTorr. Apparently, decreasing the plasma pressure resulted in better thickness uniformity.

The thickness uniformities of all films show a circular symmetry, with only a small difference in thickness between the center and the edge of the wafer. This difference is probably due to small deviations in the plasma properties across the wafer area and/or a temperature difference between the center and the edges of the wafer. The thickness uniformity does not depend on the position the precursor enters the reactor chamber, because the uniformity would not be expected to show circular symmetry in that case. The conditions that show an improved material quality also result in a better thickness uniformity.

For the refractive index uniformities the average thickness in equation 4.1 was replaced by the average refractive index. The same plots as for the thickness uniformity were made and these plots can be found in appendix D.2. The non-uniformity of the refractive index of the films deposited with a plasma exposure time of 10 and 15 seconds was 0.24% for both films. They showed an excellent and stable uniformity for long plasma exposures. For the temperature series the non-uniformities are shown in figure 4.25, indicating a very uniform refractive index across the wafers. At first, the non-uniformities did not seem to follow a temperature-dependent trend. However, since the sample deposited at 200°C was considered to be a bad data point for the refractive index as well, the 'expected' non-uniformity would therefore in this series be higher as well. The film deposited at 500°C could only be measured with relatively high modelling errors compared to the other temperatures and might be a bad

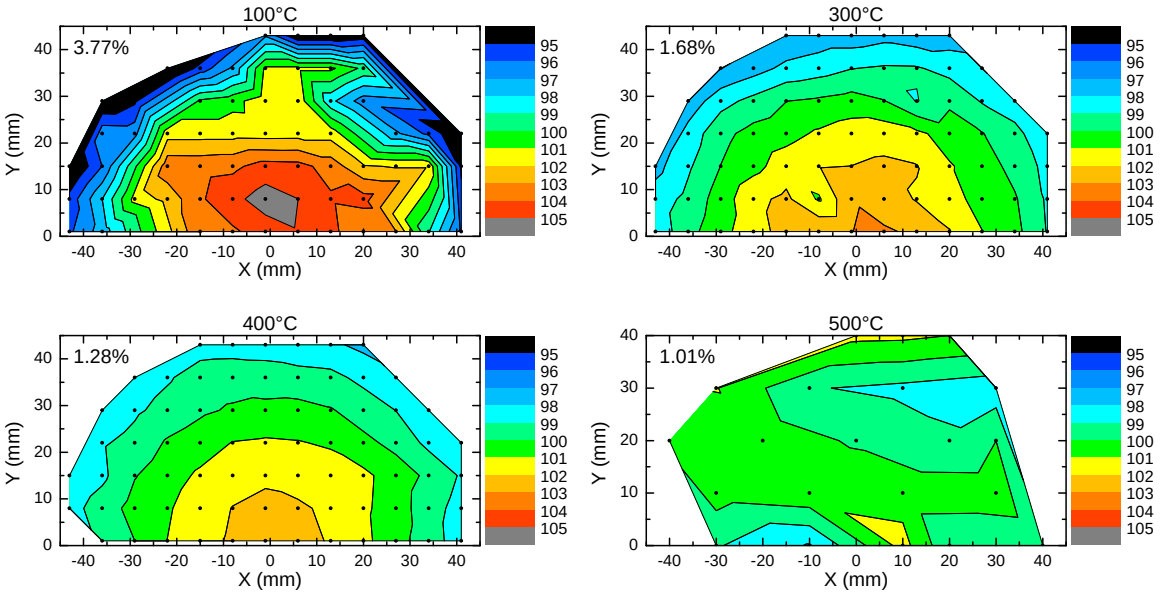

Figure 4.23: The film thickness across the wafer relative to its average thickness is plotted for films deposited at temperatures of 100°C and ranging from 300°C to 500°C. The black dots indicate the data points and the percentages in the graphs are the non-uniformities.

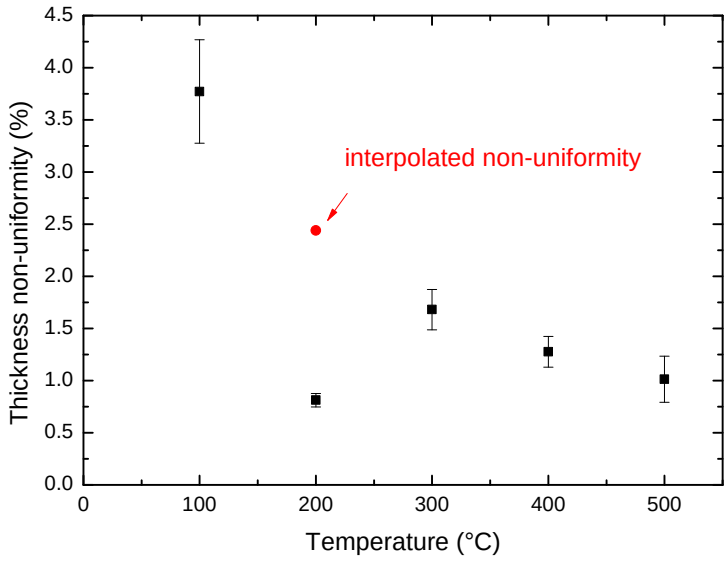

Figure 4.24: The non-uniformity of the thickness as a function of setpoint temperature. Because the film deposited at 200°C was deposited in a different run than the other films, this non-uniformity deviated from the trend. Therefore, an interpolated non-uniformity is included for this temperature, which value was also used for comparison in the plasma pressure series.

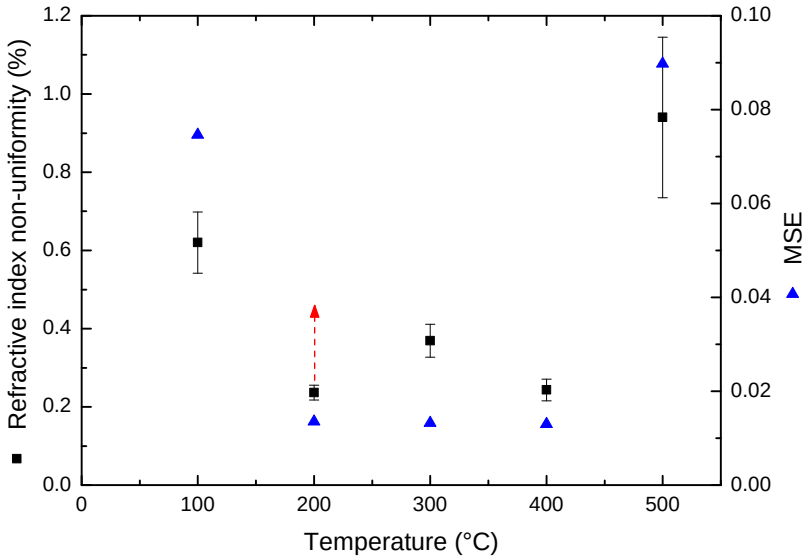

Figure 4.25: The non-uniformity of the refractive index and the MSE as a function of temperature. The red arrow indicates the direction in which the data point at 200°C probably would move when deposited in the same run as the other films.

refractive index uniformity data point as well. Therefore, an improvement of refractive index uniformity with temperature could be possible. At a pressure of 40 mTorr the non-uniformity of the refractive index was 0.24% (but deposited in a different run) and for 10 mTorr it was 0.19%. Therefore, a decrease in plasma pressure resulted in an improved uniformity of the refractive index.

The non-uniformity of the refractive index was less than 1% for all films, so for all conditions the refractive index was very uniform.

4.3 Discussion and comparison with literature

In the first section of this chapter the saturation curves of the developed process confirmed the ALD behavior of the process. The self-limiting reactions were observed for a setpoint temperature range between 100°C and 500°C, which corresponded to a wafer temperature between 100°C and approximately 350°C. The films deposited at 100°C were not stable, but their oxidation can be avoided by capping the layer with Al_2O_3 before removing them from the reactor, as was shown in a related project at room temperature [40].

The film quality was analyzed for varying plasma exposure time, deposition temperature and plasma pressure. The contamination with carbon decreased for increasing plasma exposure time and temperature and for decreasing plasma pressure. At the same time the N/Si ratio, the uniformity and the stability of the films improved, but the GPC decreased. Therefore, compromises between deposition time and film quality need to be made.

Good quality was obtained for plasma exposures longer than 7.5 seconds, temperatures of 200°C-500°C and pressures of 40 mTorr and below. In this parameter range typical GPCs were 0.14-0.32 Å and refractive indices ranged between 1.8 and 2.0. For temperatures below 200°C, low pressure plasmas could be used to improve the material properties as well.

Temperature windows reported for other ALD processes are 225°C-650°C for metal halide silicon precursors and NH_3 (gas or plasma) or N_2H_4 gas [3, 10–13, 43–46], which is generally higher than the temperatures reported in this work. The film characteristics of the good quality films in this work are compared to the material properties reported for other ALD processes in table 4.3. The GPCs reported are higher for the metal halide precursors [3, 10–13, 43], but the precursor exposure times that are reported are 15 seconds for Si_2Cl_6 [43] and 60-90 seconds for SiH_2Cl_2 [12, 13], which is 100 to 600 times longer than the 150 ms used in this work, resulting in a very long cycle time. The GPCs reported for other metalorganic precursors are comparable to the GPCs reported in this work, but precursor dosing times of one second or longer were needed. Fang *et al.* also reported silicon nitride growth with BTBAS as a precursor, but no self-limiting growth was obtained [18]. The refractive indices reported in this work for temperatures between 200°C and 500°C were higher than reported for other metalorganic precursors and comparable to those reported for the metal halide precursors [3, 10, 12, 18, 43]. The refractive indices for the metalorganic precursors reported by Fang *et al.* are relatively low due to post-oxidation (as is the case for the low temperature ALD process in this work), but they reported that *in situ* measurements resulted in a refractive index of 1.950 for 3DMAS, which is comparable to the refractive indices reported in this work [18]. The films reported in this work were nitrogen rich compared to the films reported for metal halide precursos, which are closer to stoichiometric Si_3N_4 or even silicon rich [3, 10–13, 43]. The high nitrogen contents observed in this work might be due to the structure of BTBAS. The relatively low N/Si ratio of the 3DMEAS film reported by Fang *et al.* [18] does not correspond to the refractive index measured, because a silicon-rich film should lead to a high refractive index. Compared to the other ALD processes, BTBAS resulted in average oxygen and hydrogen contents and mass densities closer to that of stoichiometric Si_3N_4, which is 3.1 g/cm^3 [16]. The exact temperatures at which these properties were determined have not been reported for the metal halide precursors and therefore it cannot be excluded that these properties vary across the temperature ranges investigated.

A more common deposition technique for silicon nitride is plasma enhanced chemical vapor deposition (PECVD). This technique requires temperatures between 200°C and 400°C [7], which is comparable to the temperatures reported in this work. However, films deposited with PECVD contain a substantially larger amount of hydrogen (up to 30 at%) and can contain some oxygen (1-4 at%) [7, 9, 47]. The amount of hydrogen in the films with the ALD process developed in this work was much lower and the oxygen content was comparable. The N/Si ratio for PECVD films is between 1.2 and 1.4 [7, 47], which is closer to stoichiometric Si_3N_4 than the N/Si ratios of the ALD films. PECVD films are thus more likely to be silicon rich, while ALD films are nitrogen rich. The refractive index for PECVD films is 1.99, within the range of the refractive indices of the good quality ALD films [7, 47].

Generally, LPCVD processes for silicon nitride require deposition temperatures of 700°C and higher [4], but for the combination of BTBAS as the precursor and NH_3 as the reactant, deposition temperatures between 550°C and 600°C are reported [5, 14]. This temperature range is still well above the temperature window reported in this work. The carbon contents for these LPCVD films are 5-7 at%, which is comparable to the values reported in this work for the high temperature process [5, 14]. The hydrogen contents reported in this work were lower than those for the LPCVD films with BTBAS, which were 10-16 at%, but with SiH_2Cl_2 (700°C-800°C) hydrogen contents of 3.6 at% were reported [5, 14].

In summary, the silicon nitride ALD process developed in this work resulted in high quality films in a wide temperature window. This temperature window might even be extended towards room temperature when the process is optimized further. The films showed almost

no post-oxidation unlike processes with other metalorganic precursors. The GPC of the developed process was relatively low compared to processes with metal halide precursors, but relatively short cycle times, mitigating the effect of a low GPC in terms of thickness increase per unit of time, and high uniformity could be achieved in a wide temperature window.

Table 4.3: Summary of the comparison between various reported silicon nitride ALD processes [3, 4, 10–13, 15, 18, 43]. When there are no values mentioned, the corresponding properties have not been reported.

	Metalorganic precursor					Metal hydride precursor	Metal halide precursor			
Precursor	BTBAS	BTBAS	2DEAS	3DMAS	4DMAS	SiH_4	$SiCl_4$	SiH_2Cl_2	Si_2Cl_6	Si_2Cl_6
Reactant	N_2	N_2	H_2-N_2	H_2-N_2		N_2	NH_3	NH_3	NH_3	N_2H_4
Temperature (°C)	100	200-500	300	350	300	250-400	225-625	250-500	515-573	525-650
GPC (Å)	1.1-1.3	0.14-0.32	0.37	0.40	0.20	0.25-2	2.45	0.9	2.4-2.7	2.3
n	1.6-1.7	1.8-2.0	1.775	1.750	1.700	1.7-1.85	2.01	1.6-1.9	1.7-1.8	1.8-2.1
N/Si	2.66-3.13	1.48-1.72		0.71		1.2	1.35	0.9-1.1	1	1.39
[O] (at%)		2.9-4.7 ±1.3		2				6.3, 0.5, <2	7-8	4
[H] (at%)		5.0-10.9 ±0.5						13		<1
[Cl] (at%)							0.4	0.5		
Mass density (g/cm^3)		2.2-2.9 ±0.2				2.5-2.9		2.6		
Reference	This work	This work	[18]	[18]	[18]	[15]	[10]	[4, 11–13]	[3]	[43]

Chapter 5

On the growth mechanism of plasma-assisted atomic layer deposition of silicon nitride

This chapter deals with the results of a study on the growth mechanism of silicon nitride when prepared by ALD. In order to actually determine the growth process, specific information is required about the reaction products during the precursor dosing and the plasma step, and the surface groups before and after these steps. Quadrupole mass spectrometry (QMS) and optical emission spectroscopy (OES) can give information about the reaction products, but not directly about the surface groups. Knowledge of the surface groups is needed for conclusive determination of a growth mechanism and *in situ* infrared spectroscopy could provide this information directly, but since this diagnostic was not available, assumptions had to be made. Where possible, the experimental results will be used to support these assumptions.

The process was thus investigated with QMS and OES. In the first section the determination of the reaction products with QMS will be discussed. The second section will address the proposed reaction mechanism for the standard process and this mechanism will be used to explain the trends observed in the previous chapter. It was shown before (figure 4.1c) that hydrogen-containing plasmas resulted in relatively low GPCs compared to pure N_2 plasmas at 350°C. A similar effect was observed at 200°C, as will be shown in section 5.3. In the same section the influence of hydrogen, when added to the plasma, will be shown using data obtained with OES. The mechanism leading to the reduced GPC for hydrogen-containing plasmas will be discussed in this section as well. In the last section a short summary of the observations in this chapter will be given.

5.1 Determination of reaction products

During the precursor dosing and the plasma exposure, surface reactions occur. Gas phase reaction products can be formed, which can be detected by QMS measurements. When a systematic approach is used, reaction products during the precursor dosing and plasma step can be determined. This approach will be addressed first, followed by the determination of the reaction products. Note that reactions at all surfaces in the reactor contribute to the QMS signal (not only those at the surface of the substrate) and that some of these surfaces have a relatively low temperature compared to the substrate temperature. The GPC at

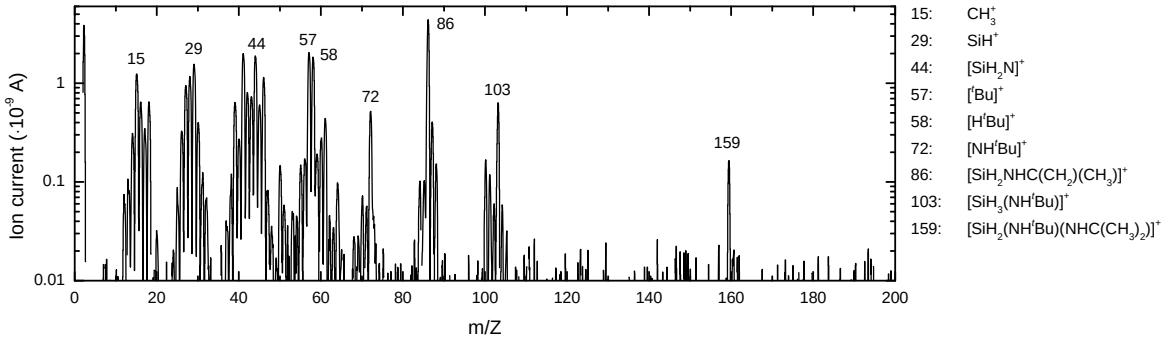

Figure 5.1: The cracking pattern of BTBAS ($SiH_2(NH^tBu)_2$), determined at 200°C. The list on the right shows the most probable assignments for some peaks. Note that due to recombination in the mass spectrometer other assignments are possible as well (see text).

these low-temperature surfaces is higher than the GPC on the substrate. Combined with the differences in *t*-butylamine ligand removal in the plasma step at different temperatures (as shown by the difference in carbon and hydrogen impurities in the films in section 4.2.2), this leads to a large impact on the measured QMS signal.

5.1.1 Procedure

In this work the quadropole mass spectrometer was used to measure both with a low and a high temporal resolution. The measurements with low temporal resolution consisted of several scans in which a wide range of m/Z values was measured per scan. This method was used to determine the cracking pattern of BTBAS, which is shown in figure 5.1. There is no peak observed at $m/Z = 174$, which would correspond to ionized BTBAS. This suggests that the BTBAS molecules fragmented when ionized. Other peaks are observed for ligand fragments, e.g., $m/Z = 72$ ($[NH^tBu]^+$). Some signals could not directly be ascribed to ligand fragments, but were a result of recombination. This could be recombination of ligand fragments (e.g., $[SiH_2NHC(CH_2)(CH_3)]^+$at $m/Z = 86$) or recombination of ligand fragments with hydrogen that was adsorbed on the walls of the mass spectrometer, as was suggested before [48]. $m/Z = 58$ ($[H^tBu]^+$) and $m/Z = 103$ ($[SiH_3(NH^tBu)]^+$) are examples of cases where an additional hydrogen atom bonded to the ligand fragments. McElwee-White showed that mass spectrometry can be used to identify which bonds in a precursor are most likely to break during deposition, since they also easily break in the mass spectrometer [49]. The peak at $m/Z = 103$ suggests that one Si−N bond is relatively easy to break, while the second bond is much more stable.

The reaction products were determined by measurements of the m/Z values 2 and 7-60 as a function of time. In order to obtain a high temporal resolution, only 4 m/Z values were measured in the same run. In every run, one of these values was $m/Z = 40$, which represents argon and was used as a reference signal to synchronize the data. There were three different cycle modes and comparing these modes in a systematic way gave information about the reaction products. The three cycle modes were:

- *ALD*: this mode consisted of regular ALD cycles. During the precursor step cracking of BTBAS, reaction products and background signals contributed to the measured signal. Stable plasma species, reaction products and background signals determined the QMS signal during the plasma step.

- *Precursor only*: this mode consisted of cycles in which there was no plasma. To keep all other conditions the same, this was achieved by setting the plasma power to 0 W. In this mode there were BTBAS cracking products and background signal, but there were no reaction products, as no ALD reactions took place.

- *Plasma only*: this mode consisted of cycles in which there was no precursor dosing. This was done by keeping the bubbler valve closed. In this mode there were no reaction products, only gas phase species and background signal.

For each group of 4 m/Z values, 10 deposition cycles of each mode were run. The data was then synchronized and normalized to the argon signal and all but the first cycle of each run were averaged to reduce the noise. The first cycle was not used, since it might have been influenced by the conditions of the previous run. The procedure, synchronization and normalization of the data is explained in more detail in references [23, 50]. An example of the resulting data is shown in figure 5.2 for 4 m/Z values measured in the ALD mode. $m/Z = 27$ can be assigned to HCN during the plasma exposure, which was a reaction product (as will be shown later), $m/Z = 28$ corresponds mostly to N_2, $m/Z = 40$ is the argon reference signal and $m/Z = 57$ is *t*-butyl, one of the lines in the spectrum of the precursor. The cycle steps are indicated in figure 5.2 as well. The cycle was extended with a post-plasma step compared to the normal ALD cycle used in the previous chapter. The pre-dose, precursor purge and pre-plasma step were longer than in the normal ALD cycle to better visualize the influence of each step. Since the precursor dosing time (2) was very short (200 ms in this case), the influence of the dosing was seen in the consecutive reaction step (3) by the increase in the intensity of the $m/Z = 57$ line. In the pre-plasma (5) the N_2 flow was turned on (increasing $m/Z = 28$), so that it was stable when the plasma was ignited.

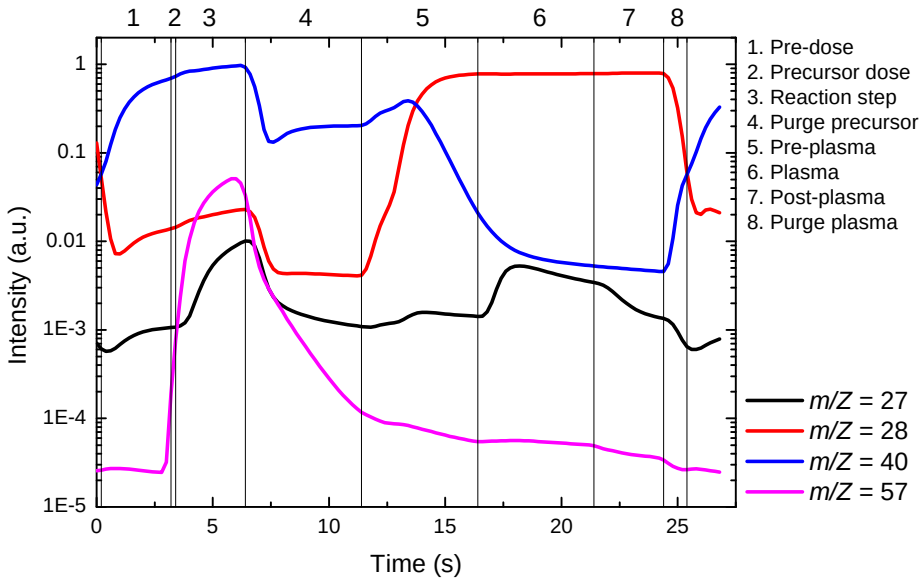

Figure 5.2: An example of the synchronized, normalized and averaged QMS signals for the ALD mode for $m/Z = 27$, 28, 40 and 57. The cycle steps are indicated. During step 1-4 and 8 the argon flow was used to purge the precursor delivery lines and entered the reaction chamber, while during the other steps it was diverted directly to the exhaust.

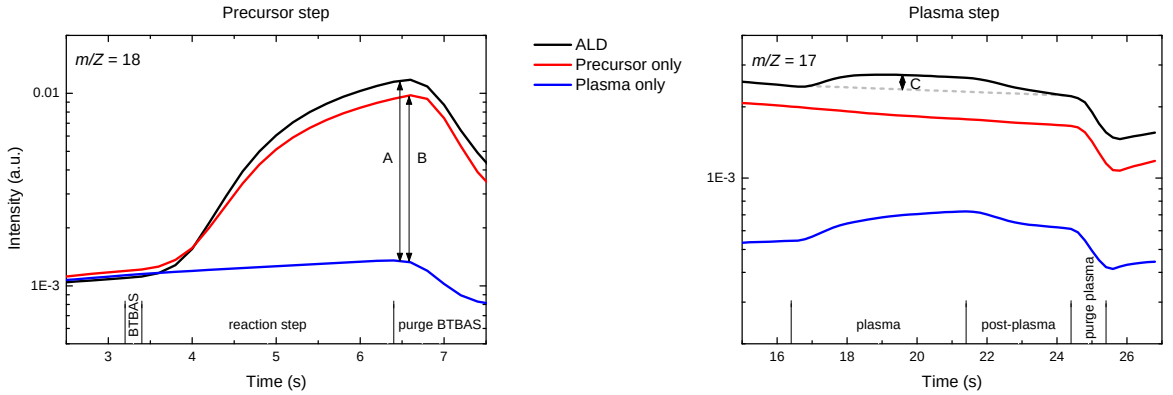

Figure 5.3: An example of the 3 cycle modes for $m/Z = 18$ for the precursor step (left) and for $m/Z = 17$ in the plasma step (right). The grey line indicates the expected background signal in the plasma step.

5.1.2 Reaction products

By subtracting the different modes from each other the reaction products could be quantified. As an example the three modes are plotted for $m/Z = 18$ for the precursor step and for $m/Z = 17$ in the plasma step in figure 5.3. Note that in the ideal case all three modes should show the same background. In figure 5.3 this is approximately the case for $m/Z = 18$ in the precursor step. However, the background of the plasma only and precursor only modes were different than that of the ALD mode (indicated by the grey line) for the plasma step of $m/Z = 17$. Therefore, for some m/Z values an offset was added to these two signals to serve as a good background.

Comparing the ALD and plasma only modes (A), the contribution of the reaction products in the precursor step and cracking of the precursor can be determined. The cracking products of BTBAS can be determined by comparing the precursor and plasma only signals in the precursor step (B).

In the ideal case the reaction products in the plasma can be determined by subtracting the plasma only mode from the ALD mode. However, even with the correction for the background, the plasma only signal did not overlap with the expected background of the ALD mode in the plasma step. The difference in background between the plasma only mode and the ALD mode is probably caused by the absence of precursor in the background of the QMS signal for the plasma only mode. Therefore, instead of the rescaled plasma only mode, the rescaled precursor only mode was subtracted from the ALD mode to determine the reaction products in the plasma step (C in figure 5.3).

When this procedure is used for the whole range of m/Z values, mass spectra of the reaction products can be obtained and compared to spectra in the NIST database to identify the reaction products [24]. The spectra in the NIST database were obtained on a different spectrometer, which will account for slight differences between the spectra in the NIST database and the spectra in this work.

The spectrum for the reaction products in the precursor step and cracking of the precursor (signal A) is shown in figure 5.4a. Figure 5.4b shows the cracking pattern of BTBAS (signal B). Figure 5.4a and b show good correspondence, indicating a large contribution of the BTBAS cracking products in the signals in figure 5.4a. When the cracking pattern is subtracted from the spectrum in figure 5.4a the reaction products in the precursor step re-

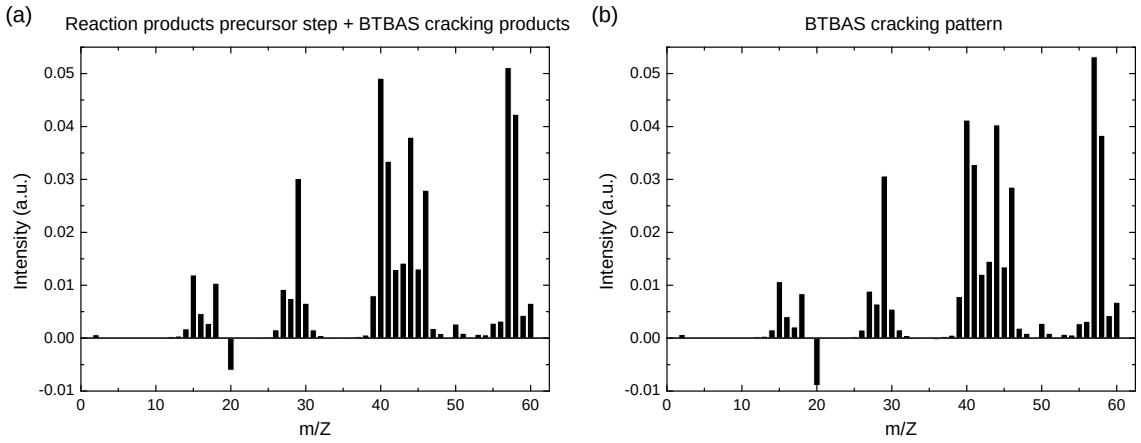

Figure 5.4: (a) The reaction products and BTBAS cracking products in the precursor step during the normal ALD cycle and (b) the cracking pattern of BTBAS during the precursor only cycle.

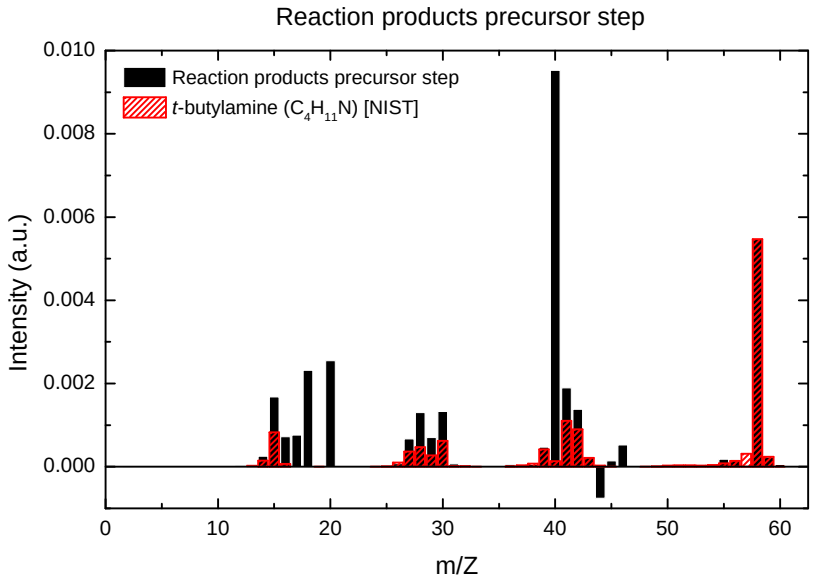

Figure 5.5: The reaction products in the precursor step compared to the mass spectrum of *t*-butylamine ($C_4H_{11}N$) [24].

main. These reaction products are shown in figure 5.5 and compared to the spectrum of *t*-butylamine (H_2N^tBu, one ligand of BTBAS with an additional hydrogen atom) that is taken from the NIST database [24]. There is good overlap between the two spectra. This strongly suggests that *t*-butylamine was the main reaction product during precursor dosing. Some of the other lines can (partly) be explained by fluctuations in the argon (m/Z = 20 and 40) and water (m/Z = 16-18) levels.

The reaction products in the plasma step are shown in figure 5.6 for a temperature of 350°C and in figure 5.7 for a temperature of 200°C. For 200°C only a few representative m/Z values have been measured. A comparison with molecules in the NIST database is made [24]. Cyanogen (C_2N_2), ammonia (NH_3), hydrogen (H_2) and the ligand fragments propane (C_3H_8) and hydrogen cyanide (HCN) were detected as reaction products. Nitrogen was consumed during the plasma exposure and there was a high background level of water in the reactor. The presence of argon explains the signals at m/Z = 20 (Ar^{2+}) and 40 (Ar^+). Since the cracking pattern of the *t*-butylamine ligand is also observed, there were still *t*-butylamine ligands at the surface before the plasma was ignited. Some *t*-butylamine ligands were thus removed completely (i.e., not in fragments) during the plasma step. At 200°C some BTBAS was left in reactor regions that were difficult to purge in the precursor only mode. The relatively high signal at m/Z = 14 is somewhat unexpected. Since there is no high (positive) signal at m/Z = 28, it cannot be ascribed to N_2. It could be due to oxygen contamination in the reactor or in the processing gases, which could lead to formation of N_xO_x species, which would also (partly) explain the signal at m/Z = 30. The high signal at m/Z = 14 might also be explained by a long lifetime of nitrogen radicals, which are a result of the reaction $e^- + N_2 \rightarrow 2N + e^-$, as suggested by the lifetimes reported by Wróbel *et al.* [51]. Note that other reaction products (e.g., ethane (C_2H_6)) might have been present, but that their contribution was relatively low. To determine whether other reaction products, like isopropylamine, acetonitrile, propylamine, isobutene and ethylamine, were present or not, the spectrum should have been measured in a wider m/Z range.

Although at both temperatures the same reaction products were measured, there was a difference in their ratios: at 200°C there was relatively more hydrogen and propane present compared to HCN than at 350°C. Note that the films deposited at 200°C contained more carbon and hydrogen than the films deposited at higher temperatures. The observation of more hydrogen and carbon in the plasma and higher contaminations in the resulting films suggests that redeposition of these species caused the impurities in the film (i.e., reaction products interact with the plasma forming new species that can be deposited on the surface [23]).

5.2 Proposed growth mechanism

In this section a growth mechanism will be proposed. The trends that were observed in the previous chapter will be explained with the proposed growth mechanism.

5.2.1 Precursor adsorption

In section 5.1.2 it was observed that the BTBAS ligand with one additional hydrogen atom (*t*-butylamine) was the main reaction product in the precursor step. There were also intact *t*-butylamine ligands present before the plasma was ignited, since complete *t*-butylamine ligands were detected as reaction products in the plasma exposure step. Therefore, the simplest assumption, that only one *t*-butylamine ligand was removed during the adsorption

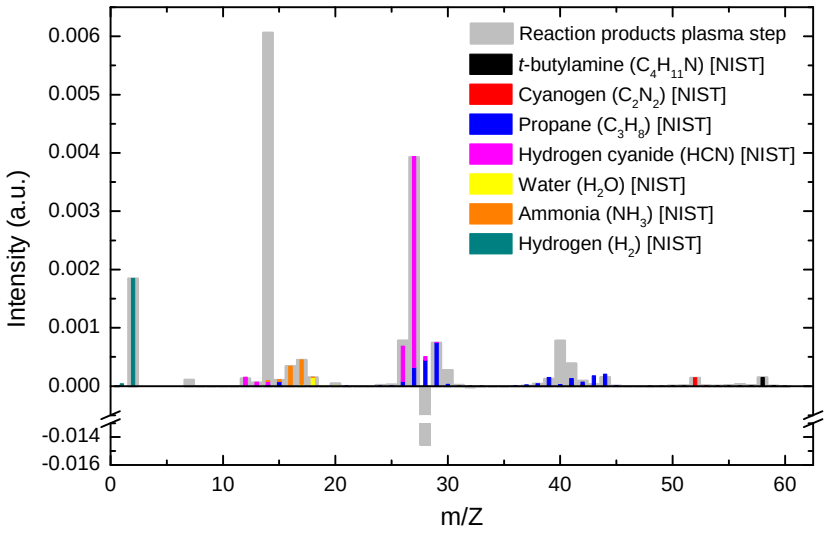

Figure 5.6: The reaction products in the plasma step compared with possible reaction products for a temperature of 350°C [24]. Note that the molecules in the legend are listed in order of decreasing m/Z values.

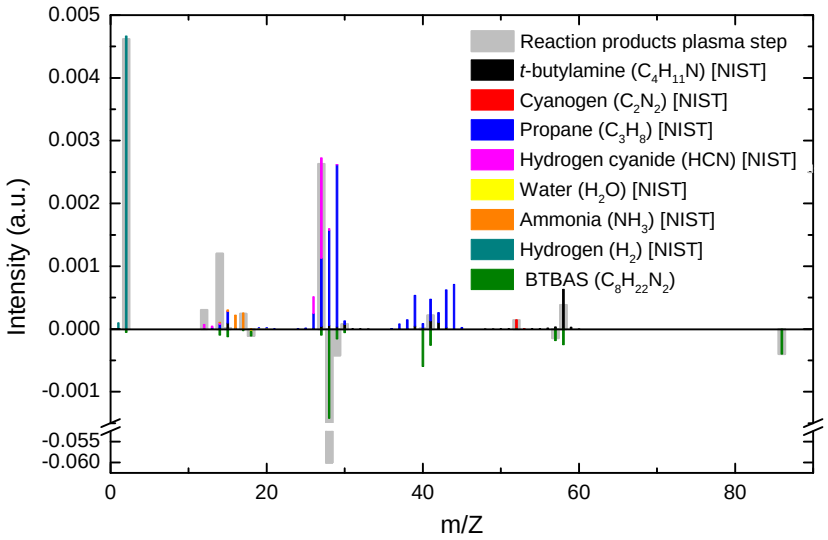

Figure 5.7: The reaction products in the plasma step compared with possible reaction products for a temperature of 200°C [24].

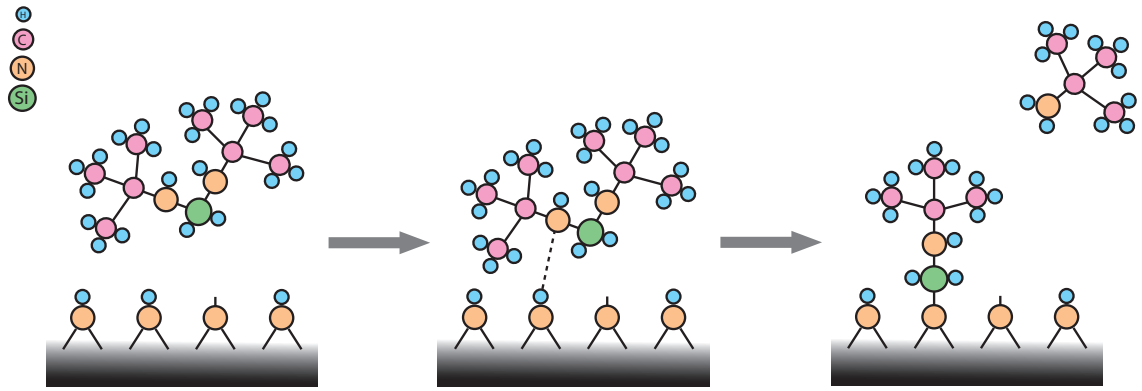

Figure 5.8: The proposed adsorption mechanism of BTBAS molecules: a strong hydrogen bond between a nitrogen atom of the precursor and a hydrogen atom at the surface eventually leads to migration of the surface hydrogen atom to the nitrogen atom of the precursor, resulting in the release of a *t*-butylamine ligand and the adsorption of $H_2SiNHC(CH_3)_3$.

of the precursor and that the other *t*-butylamine ligand was removed by the plasma, is made. This also corresponds to dissociation of precursor molecules in CVD, where splitting off one amine ligand strengthens the bond with the other amine ligand, as suggested by McElwee-White [49], and the BTBAS cracking pattern in figure 5.1.

Figure 5.8 shows the proposed adsorption mechanism of BTBAS molecules on the surface. The adsorption is assumed to occur due to a strong hydrogen bond between a nitrogen atom of the precursor and a hydrogen atom at the surface, as is the case in ALD of SiO_2 using BTBAS [52]. Migration of the surface hydrogen atom to the nitrogen atom of the precursor leads to dissociation of the BTBAS molecule resulting in the adsorption of $H_2SiNHC(CH_3)_3$ and the release of a *t*-butylamine molecule into the gas phase [52].

A rough calculation in the ChemBio3D Ultra program results in a BTBAS radius of approximately 5 Å. The number of BTBAS molecules (and thus silicon atoms) that would fit on 1 nm^2 is then approximately 1.27, which is roughly one order of magnitude higher than the values determined by RBS (0.5-0.7 atoms/nm^2/cycle), as shown in figure 5.9. This indicates that steric hindrance is not the limiting factor, since less BTBAS molecules adsorb on the surface than would spatially fit. Therefore, it is assumed that the surface is not fully covered with active surface groups.

As mentioned before, there was no direct information available on the surface groups and therefore it was assumed that the nitrogen plasma formed a surface with $-NH_x$ groups (x = 0, 1, 2). According to Perrine *et al.* the number x is determined by the temperature [53]. For increasing temperatures the $-NH_2$ surface groups are converted into =NH surface groups between 227°C and 377°C and further into =N− surface groups after 527°C [53], as is illustrated in figure 5.10. The dangling bonds can react with the surface to form ≡N bonds. Although the actual temperature range in this work would allow for the presence of $-NH_2$ and =NH surface groups, it is assumed that a plasma enhances the dehydrogenation process, because it was shown before that the exposure of a silicon nitride film to a nitrogen plasma results in reduction of the hydrogen content in the film [39] and the ERD data in the previous chapter showed decreasing hydrogen concentrations for increasing temperatures. This suggests that there were mainly =NH and =N− or ≡N surface groups. Furthermore, other experiments suggested that it is unlikely that $-NH_2$ surface groups were the reactive surface groups, as will be shown in section 5.3.

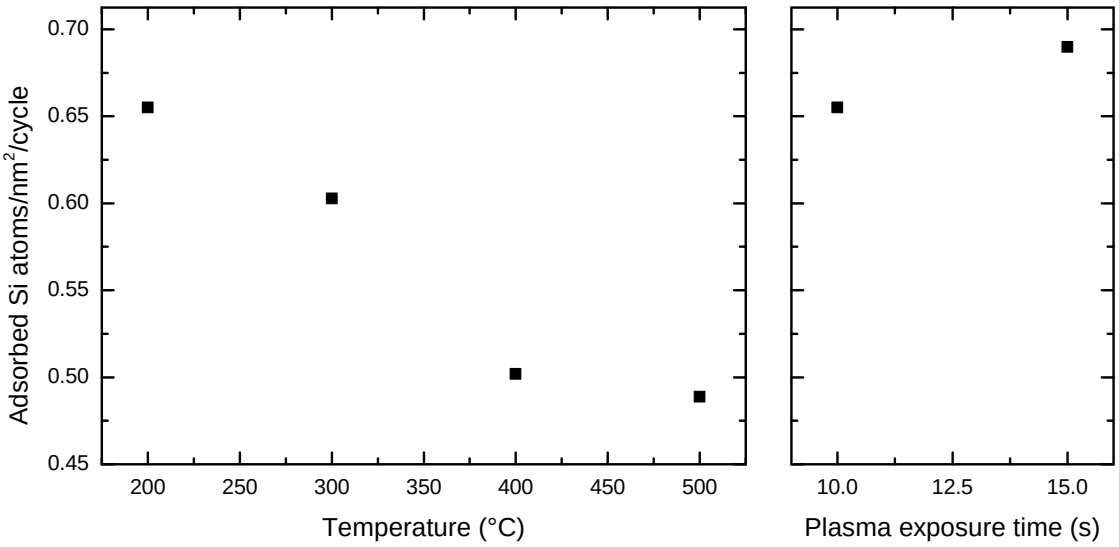

Figure 5.9: The number of adsorbed silicon atoms per nm² per cycle (determined by RBS) as a function of temperature (left) and plasma exposure time (right). In the left figure the plasma exposure time is 10 seconds, in the right figure the temperature is 200°C.

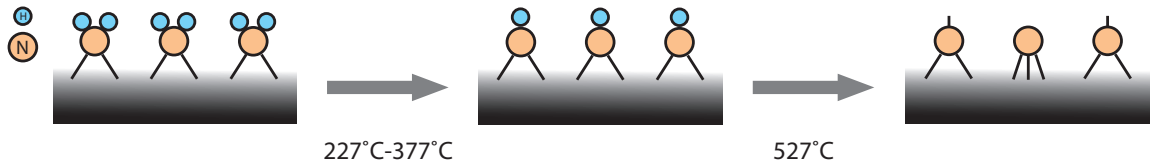

Figure 5.10: A schematic representation of the conversion of -NH_x surface groups as a function of temperature as suggested by Perrine *et al.* [53].

Since steric hindrance was not the limiting factor for the BTBAS adsorption, it was suggested that the surface was not fully covered with active surface groups (i.e., not all $-NH_x$ surface groups were considered to be reactive) and therefore another assumption was made: BTBAS only adsorbs on =NH surface groups. Since an increase in temperature resulted in a decreasing GPC (figure 4.10) and a decreasing number of adsorbed silicon atoms per nm² (figure 5.9), but also in dehydrogenation [53], this suggests that =N− or ≡N surface groups are not reactive. For a temperature of 200°C an increasing plasma exposure time resulted in an increasing number of adsorbed silicon atoms (figure 5.9), which could suggest that more $-NH_2$ surface groups were dehydrogenated by longer plasma exposures, leading to more reactive =NH surface groups. Longer plasma exposure times also resulted in more carbon removal (as shown in the previous chapter), which could make more incorporated nitrogen atoms (bonded to hydrogen) accessible for BTBAS to adsorb on.

5.2.2 Plasma exposure

The reaction products during the plasma step have been determined to be *t*-butylamine, cyanogen, propane, hydrogen cyanide, ammonia, and hydrogen (see section 5.1.2). Depending on the plasma conditions the *t*-butylamine ligands, that remained at the surface after precursor adsorption, were removed by the plasma. The fragments that were removed could

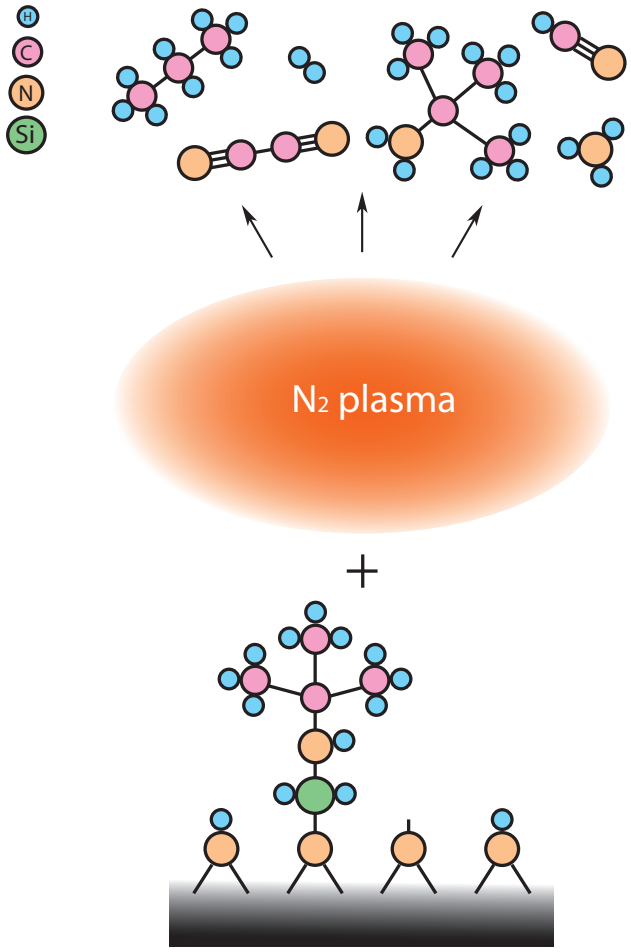

Figure 5.11: The proposed reaction mechanism during the plasma step. The nitrogen plasma removes (part of) the ligands and these ligand fragments can react in the plasma to form the detected reaction products.

interact with each other or with the plasma species and form new species, which might lead to redeposition on the surface [23]. The redeposited species could be removed again by the plasma. The reaction products measured in section 5.1.2 could originate from any of these processes. This is schematically drawn in figure 5.11. In the ideal ALD cycle all ligands would be removed, but even in the best quality films some ligands were only partly removed by the plasma, since it was observed that there was still carbon and hydrogen left in the films. Furthermore, XPS data shows silicon-carbon bonds, which suggests redeposition of reaction products, since this type of bond is not present in the precursor molecule. The presence of these bonds in the film shows that the redeposited species have not been removed completely by the plasma. During the plasma step Si−N and Si−Si bonds at the surface of the film could be broken and formed, such that the material reorganized towards a stoichiometric Si_3N_4 configuration. In literature it is suggested that the N_2^+ ions and/or the reactive dangling bonds are responsible for this reorganisation [15, 39].

5.3 Growth inhibition with hydrogen-containing plasmas (NH_3 and H_2-N_2)

Figure 4.1c showed that hydrogen-containing plasmas resulted in GPCs that were significantly lower than for a N_2 plasma. In this section the mechanism leading to this reduced growth will be investigated. OES is a useful tool for identifying *t*-butylamine ligand removal, as will be shown for the normal ALD cycle. It will be shown how OES data can be used to explain the reduction of carbon content for low pressure plasmas and the limitations of OES will be addressed with data from the temperature series. Since OES can provide information about *t*-butylamine ligand removal, an OES study was performed for the hydrogen-containing plasmas. Two types of tests were used to investigate the limited growth with hydrogen-containing plasmas and the results of these tests led to insight into the reaction mechanism, which will be explained in the last part of this section. Since there was almost no growth, no significant signal of reaction products was expected and therefore QMS measurements were not performed.

5.3.1 Identifying ligand removal

OES is a diagnostic tool that can be used to study the reaction mechanism. Even though it can only obtain information during the plasma step, it can provide information about the precursor step as well. For this study, only the time-dependent acquisition mode was used. The five wavelengths that were measured are intense lines in the spectra of NH, CN, H and CH, since they could be related to the reaction products, and one wavelength where N_2 emission is expected [54, 55]. Compared to QMS, OES data needed little processing to get useful information, as is shown in figure 5.12. In this figure the N_2 plasma only (a) and ALD mode (b), as defined in section 5.1.1, are plotted for a cycle with a N_2 plasma. The signal in the plasma only mode (a) was caused by the emission of the N_2 plasma at these wavelengths and can be considered as a background signal for the ALD mode. The difference between the two spectra in figure 5.12 is mainly seen in the CN signals, which is thus a strong indicator for *t*-butylamine ligand removal. Therefore, the CN emission will be used to obtain information about the mechanism leading to the reduced GPC for hydrogen-containing plasmas. The NH and H emission also show a small increase in emission in the ALD mode compared to the plasma only mode. The CH signal was very low, probably due to the great number of collisions the reaction products (e.g., propane) need before excited CH can be formed. The small peaks in the first half-second after the plasma was ignited, were caused by changes

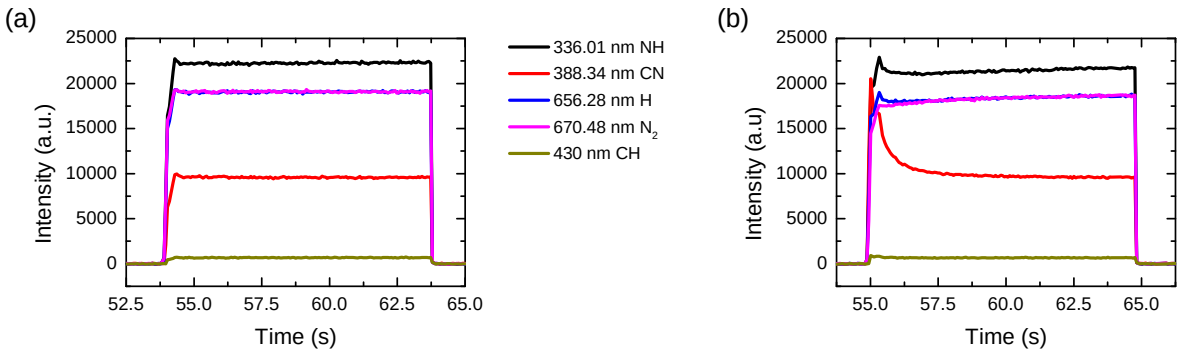

Figure 5.12: The OES spectra for a N_2 plasma in a cycle without precursor dosing (plasma only mode) (a) and with precursor dosing (ALD mode) (b).

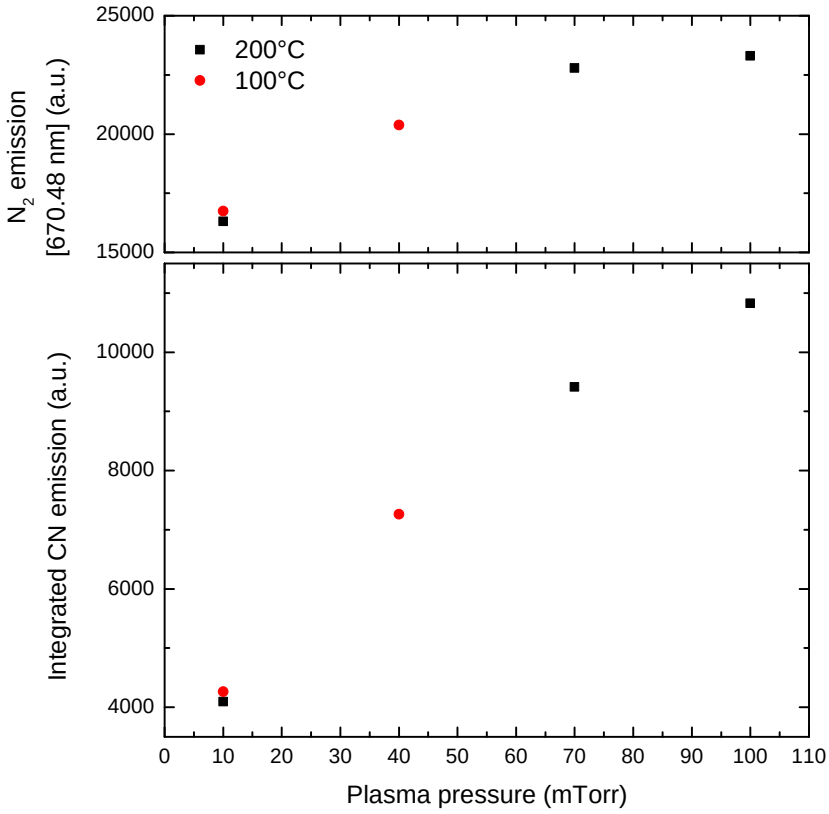

Figure 5.13: The integrated intensity of the CN emission (after subtraction of background emission) as a function of plasma pressure. The emission of the N_2 plasma at 670.48 nm is plotted as a reference.

in the matching network for optimized power coupling of the ICP. As soon as the matching network stabilized, the OES signal stabilized as well, as can be seen in figure 5.12a. This effect is also visible in the CN peak in figure 5.12b, which shows a small peak on top of the main peak.

First, the increase of the carbon content as a result of increasing plasma pressure (see section 4.2.3) will be explained with the OES data of the same series. Because the CN emission is a strong indicator for ligand removal, the integrated intensity (after subtraction of the background) provides information about the amount of CN in the reactor. Figure 5.13 shows that there was more CN detected in the reactor for increasing plasma pressures, while the N_2 emission showed an increase that was less strong. The increase of CN emission for increasing plasma pressure can be explained by the fact that the butterfly valve was opened less for high pressures, resulting in a longer residence time and higher CN concentration in the plasma. Due to the longer residence time, there was more chance of redeposition and therefore there were more carbon impurities in the films deposited with high pressure plasmas, as shown by XPS.

For the temperature series the amount of CN in the reactor was approximately constant, as is shown in figure 5.14, while the XPS data showed that the ligand removal improved for increasing temperature. The temperature of the walls is important in this case. OES (and QMS as well) does not only measure products from the surface reactions at the substrate, but also species coming from other reactor surfaces. The deposition on the wall can therefore

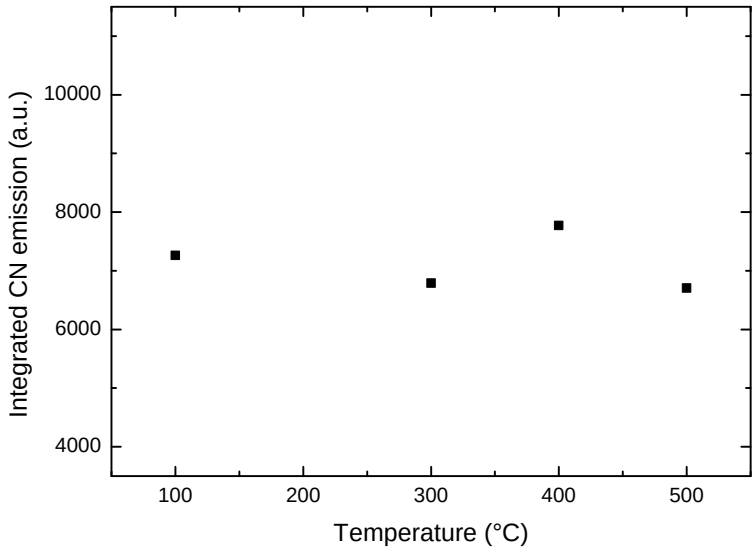

Figure 5.14: The integrated intensity of the CN emission (after subtraction of background emission) as a function of deposition temperature.

contribute significantly to the signal. For temperatures below 150°C, the wall temperature was the same as the temperature of the wafer table. For temperatures higher than 150°C the wall temperature was 150°C. Due to this difference in temperature for high setpoint temperatures, there was more deposition on the walls than on the substrate. The plasma also interacted with the deposition on the walls, which led to ligand removal there as well. Because the wall surface is relatively large, the OES and QMS signals are mainly determined by the low temperature reactions and a temperature dependent trend will be obscured. Such trend might only be observed when the wall temperature can be set to the same value as the temperature of the wafer table, which limits the possibilities of OES and QMS to observe temperature dependent trends.

5.3.2 Different plasmas and multiple plasmas in different sequences

The GPCs for hydrogen-containing plasmas were much lower than those for pure N_2 plasmas. To understand why the GPCs were lower, three questions were investigated:

1. How much hydrogen must be added to a nitrogen plasma to reduce the GPC?
2. Is it possible for a hydrogen-containing plasma to remove the *t*-butylamine ligands?
3. Is there no or less BTBAS adsorption due to the hydrogen-containing plasmas?

In order to answer these questions and to investigate the influence of hydrogen on the reaction mechanism two types of experiments were performed. The first test was the addition of an increasing amount of hydrogen to a nitrogen plasma, to see for which plasma composition the hydrogen became the limiting factor. In the second experiment an extra plasma step was added to the regular ALD cycle. By combining a nitrogen plasma and a hydrogen-containing plasma in one cycle in a systematic way, insight into the reaction mechanism could be gained.

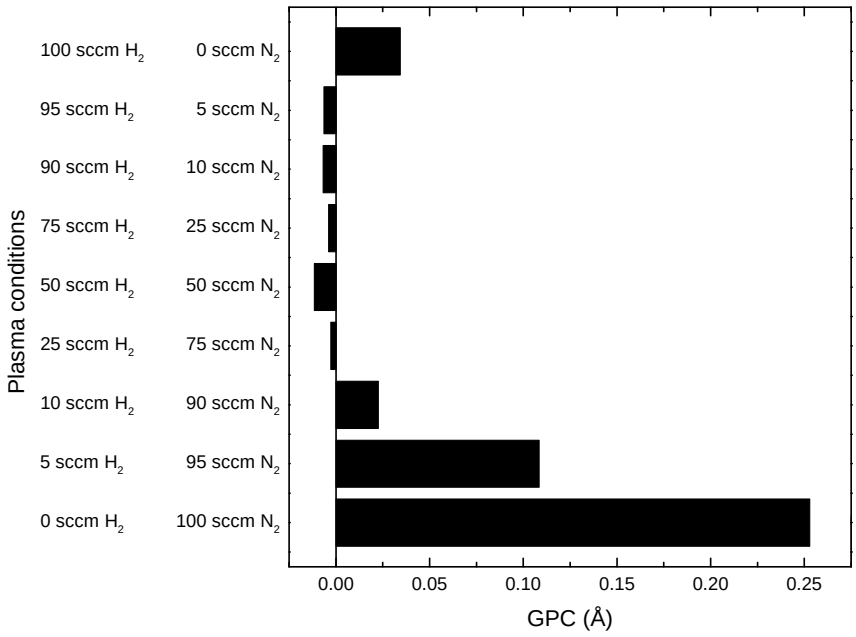

Figure 5.15: The GPC as a function of the amount of hydrogen that was added to a nitrogen plasma. The total flow rate was constant. The deposition temperature was 200°C.

For both tests the experiments with hydrogen-containing plasmas (50 cycles) were separated by 30 normal ALD cycles with a pure N_2 plasma to ensure a 'reactive' surface for each experiment as was also the case during a regular ALD cycle for silicon nitride.

The influence of the addition of hydrogen to a nitrogen plasma is shown in figure 5.15. The addition of a small amount of hydrogen already resulted in a GPC that was less than 50% of the GPC when a pure nitrogen plasma was used. The negative GPCs at higher H_2 flows might be due to densification of the already deposited material (as a result of carbon removal in the silicon nitride film that was deposited in the 30 normal ALD cycles before the experiment with a hydrogen-containing plasma). The OES data for different plasma compositions is shown in figure 5.16. For an added hydrogen flow of 5 sccm there was still some *t*-butylamine ligand removal in the second and third cycle, but for higher hydrogen flows, there was only a peak in the CN emission during the first cycle, which was expected, because the first cycle was started on a 'reactive' surface, while the following cycles were not. For hydrogen flows up to 10 sccm the OES data shows that the first seconds of the plasma step the hydrogen-containing plasma had the same emission as a pure nitrogen plasma and then suddenly changed. In these first seconds the hydrogen was probably adsorbed at the walls and when the walls were saturated, the hydrogen remained in the plasma, which led to the formation of NH_3, as shown in the increase of NH emission. Because of the formation of ammonia, the background emission changed as well, explaining the peaks observed in the CN emission (e.g., at 17.5 s for the addition of 10 sccm H_2). When more than 10 sccm of hydrogen was added to the plasma, the ammonia formation started directly when the plasma was ignited.

It is thus shown that the addition of the smallest amount of hydrogen resulted in a reduced GPC. To investigate why the GPC was reduced when a hydrogen-containing plasma was used, the ALD cycle was extended with another plasma step. One of the plasmas was a hydrogen-containing plasma (NH_3 or H_2-N_2), the other plasma was a pure nitrogen plasma.

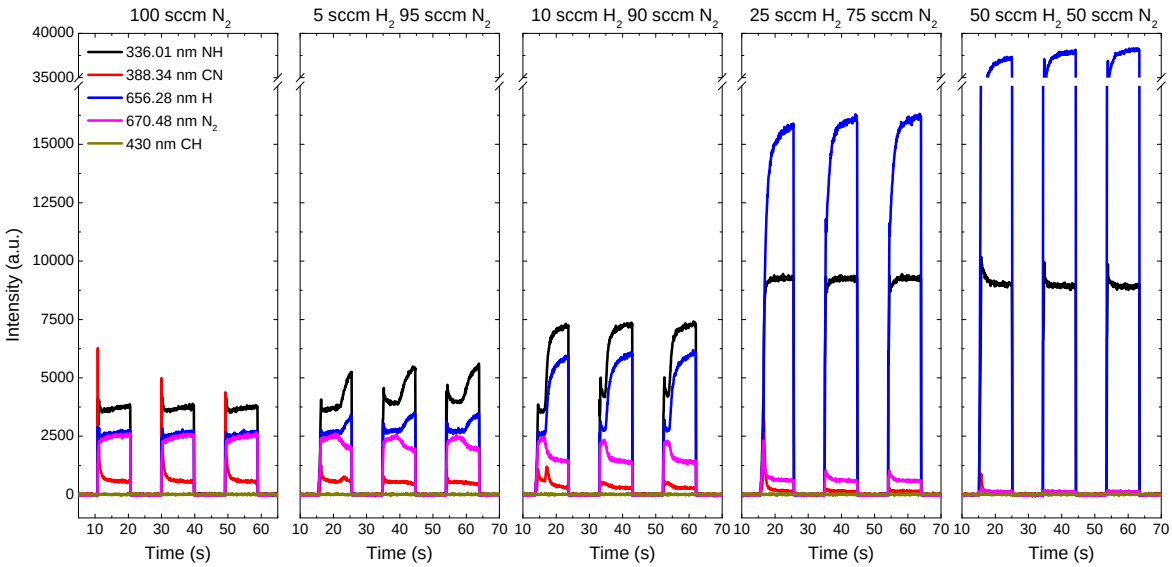

Figure 5.16: The time-dependent OES measurements of the first three cycles for different plasma compositions at 200°C.

The GPCs for these processes are shown in figure 5.17. As a reference the GPC for a pure N_2 plasma is shown as well. There was no growth when the nitrogen plasma was the first plasma after BTBAS dosing and the H_2-N_2 plasma was the last plasma in the cycle. A H_2-N_2 plasma in a cycle without a nitrogen plasma did also not result in growth. When the N_2 plasma was the last plasma in the cycle after a H_2-N_2 plasma, there was growth and the GPC increased when the N_2 plasma exposure time was increased. However, even for a N_2 plasma of 40 seconds after a H_2-N_2 plasma, the GPC was only half that of a regular ALD cycle with a pure N_2 plasma. For an ammonia plasma instead of a H_2-N_2 plasma the same trends were observed: hardly any growth when a nitrogen plasma was used before the NH_3 plasma or when only a NH_3 plasma was used in the cycle and an increasing GPC for increasing N_2 plasma exposure times after an NH_3 plasma. Also for N_2 plasmas after NH_3 plasmas the GPC of a regular ALD cycle with a pure N_2 plasma was never achieved. These observations were used to answer question 2 and 3.

If a hydrogen-containing plasma cannot remove *t*-butylamine ligands, the plasma does not create reactive surface groups, which would prevent BTBAS from adsorbing during the next precursor dosing step. However, this was not the case, as is shown in figure 5.18. When the hydrogen-containing plasma was the first plasma after BTBAS dosing, there was a peak in the CN emission, indicating that hydrogen-containing plasmas can remove the *t*-butylamine ligands of BTBAS. The consecutive nitrogen plasma showed no peak in the CN emission, suggesting that the hydrogen-containing plasma removed all the *t*-butylamine ligands.

The third question can be answered with the CN emission of two plasmas in one cycle, where the nitrogen plasma was the first plasma after the precursor dosing, as shown in figure 5.19. In the first cycle both plasmas showed a peak in CN emission, indicating that the nitrogen plasma did not remove all ligands, and that the hydrogen-containing plasma removed the remaining ligand fragments. In the second cycle there were no peaks in CN emission anymore, which leads to the conclusion that the hydrogen-containing plasma poisoned the surface somehow. This poisoning deactivated the surface groups, preventing BTBAS adsorption in the next cycle. Therefore, there is hardly any growth observed in figure 5.17 when

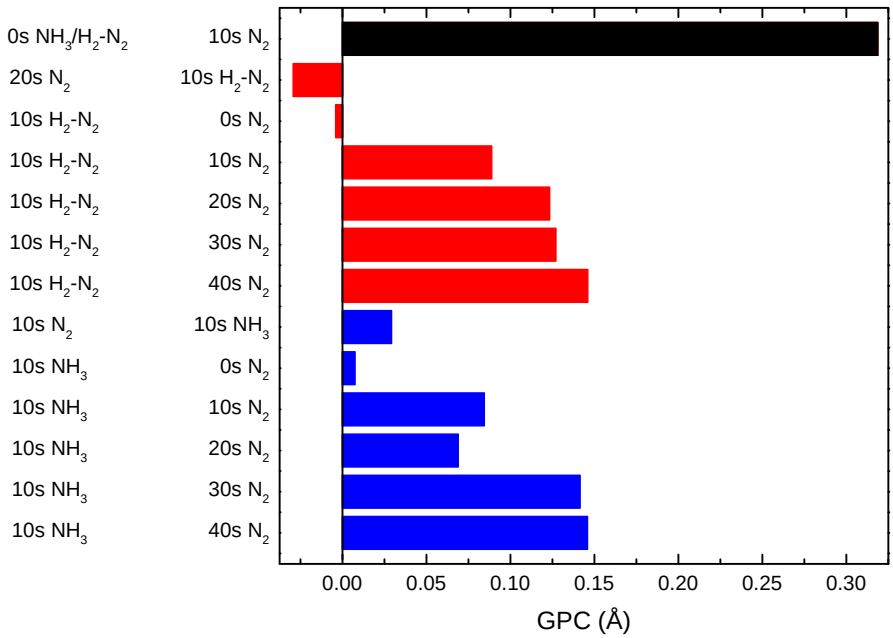

Figure 5.17: The GPC for ALD cycles that include 2 plasma steps: one with a pure N_2 plasma and one with a NH_3 or H_2-N_2 plasma. The plasma exposure time of the 2 plasmas was varied as well. The deposition temperature was 200°C.

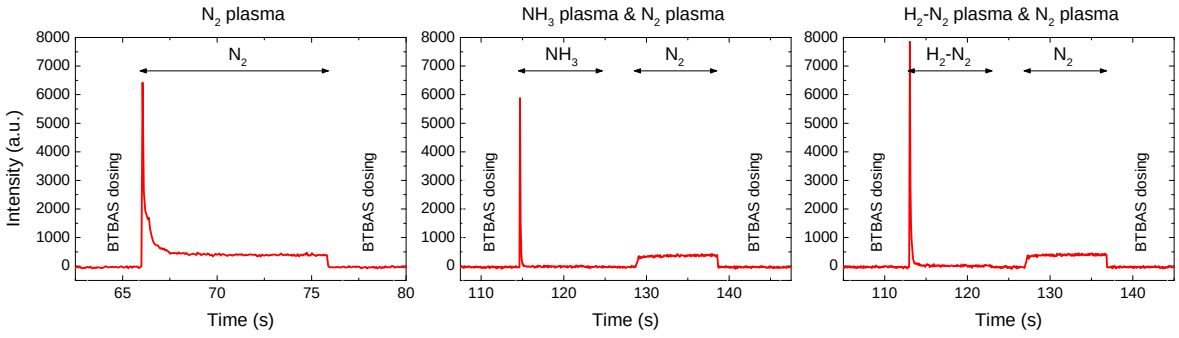

Figure 5.18: The CN emission for ALD cycles with a N_2 plasma (left), the combination of an NH_3 and a N_2 plasma (center) and the combination of a H_2-N_2 and a N_2 plasma (right).

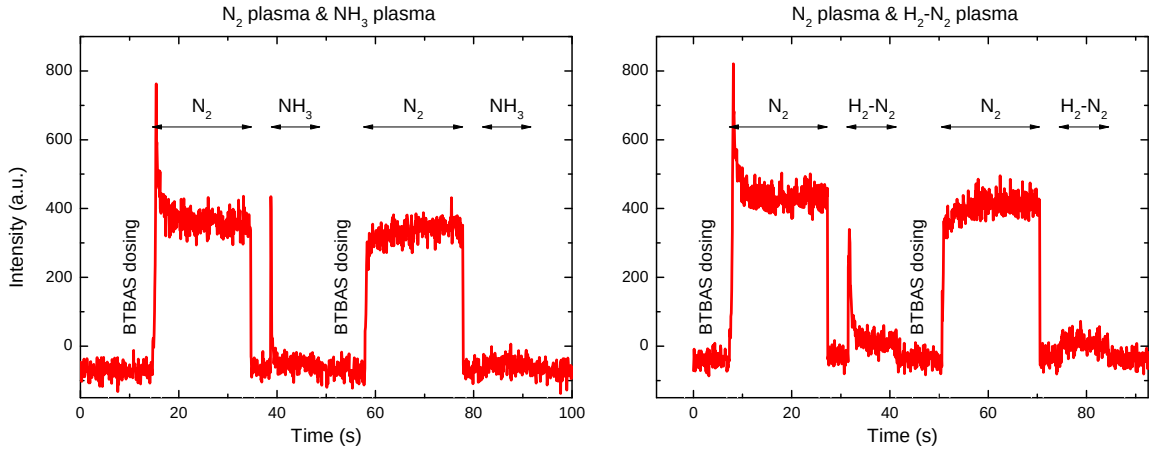

Figure 5.19: The CN emission for the first two ALD cycles with a nitrogen plasma after the BTBAS dosing, followed by a hydrogen-containing plasma.

the hydrogen-containing plasma was the last plasma in a 2 plasma cycle.

When the nitrogen plasma was the last plasma, there was growth, indicating that the nitrogen plasma could partly undo the surface poisoning induced by the hydrogen-containing plasmas. An increasing N_2 plasma exposure time led to an increasing GPC, as shown in figure 5.17 and the integrated intensity of the CN emission in figure 5.20 shows an increase for increasing N_2 plasma exposure time. The longer the exposure time of the N_2 plasma, the more surface poisoning was removed, leading to an increased number of reactive surface groups, which resulted in more BTBAS adsorption and higher GPCs. For a N_2 plasma of 40 seconds after an NH_3 plasma at 200°C the GPC was comparable to the GPC of the high temperature ALD process with only a N_2 plasma. The quality of the resulting films might also be better, because the hydrogen-containing plasmas might be more capable of *t*-butylamine ligand removal than a N_2 plasma, since the hydrogen-containing plasmas removed the ligands left on the surface by the N_2 plasma, while there were no ligands removed by the N_2 plasma after the hydrogen-containing plasmas, as suggested by comparison of figures 5.18 and 5.19. However, the cycle time for the process with two plasmas was considerably longer.

5.3.3 Mechanisms for growth inhibition

It was shown that hydrogen-containing plasmas prevented precursor adsorption, for which three possible scenarios will be described. For each scenario the reactive surface and the inhibited surface are illustrated in figure 5.21.

In the first scenario it is assumed that BTBAS only adsorbs on =NH surface groups, as in the proposed growth mechanism, but that too many =NH surface groups result in a reduction of the GPC. When these =NH groups are too densely packed, they can be deactivated by hydrogen bonding as shown in scenario 1 in figure 5.21. This is comparable to the adsorption mechanism for a metalorganic silicon precursor on −OH terminated surfaces, where the precursor mainly adsorbs on reactive −OH groups and not on hydrogen bonded −OH groups [56, 57]. The reactive −OH groups can either be isolated −OH groups or terminal −OH groups, as shown in figure 5.22 for the adsorption of a silicon precursor on an −OH terminated surface, where the latter are considered to be more reactive [56]. This scenario's main element is that isolated or terminal =NH groups are needed for a reactive surface. The N_2 plasma removes hydrogen from the surface, reducing the hydrogen bonding

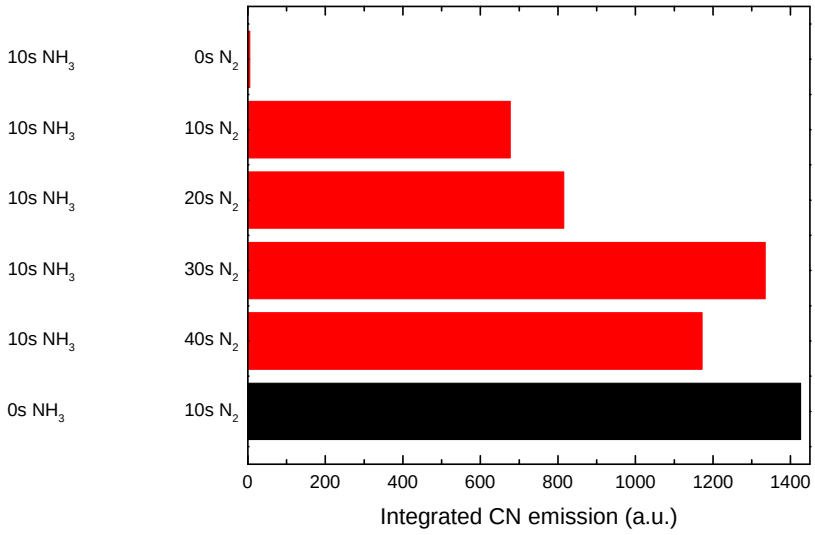

Figure 5.20: The integrated CN emission during an NH_3 plasma (red) and a N_2 plasma (black). During the cycles with two plasmas, an NH_3 plasma first and a N_2 plasma last, there was only CN emission during the NH_3 plasma.

component and therefore creating reactive =NH groups. This scenario also explains why the number of adsorbed silicon atoms is less than the number of BTBAS molecules that would fit on the surface (section 5.2), because the presence of reactive surface groups is low due to hydrogen bonding.

A second possibility is inspired by the data in figure 5.23, where the GPC is plotted as a function of plasma purge time for an NH_3 plasma. The increasing GPC as a function of purge time suggests that purging can remove the surface poisoning. Adsorption of NH_3 at the surface, presumably through hydrogen bonding, would block the adsorption sites, as shown in scenario 2 in figure 5.21, and longer purge times would remove the physisorbed NH_3 species, which leads to an increase in available reactive surface groups. Note that NH_3 is also formed in H_2-N_2 plasmas [23]. In case of a N_2 plasma after a hydrogen-containing plasma, the N_2 plasma step can serve as an additional (plasma-assisted) purging step and remove the adsorbed NH_3 molecules. The longer the surface is exposed to the N_2 plasma, the more reactive the surface becomes.

A third scenario is suggested by King, who proposed a growth mechanism where the N_2 plasma creates a nitrogen terminated surface with dangling bonds and where SiH_4 only adsorbs on nitrogen dangling bonds and not on =NH or $-NH_2$ surface groups [15]. In this scenario the presence of hydrogen in the plasma decreases the number of reactive surface groups, due to the formation of =NH (and $-NH_2$) surface groups (shown as scenario 3 in figure 5.21). A nitrogen plasma can remove the poisonous hydrogen atoms, reactivating the surface again. This scenario can fully explain the trends observed for the GPC, but it cannot explain the observed decrease in the number of adsorbed silicon atoms per cycle for an increasing temperature (figure 5.9), because more dangling bonds would be created due to dehydrogenation for an increasing temperature [53] and therefore more adsorbed silicon atoms would be expected for this scenario. For BTBAS, the adsorption on dangling bonds

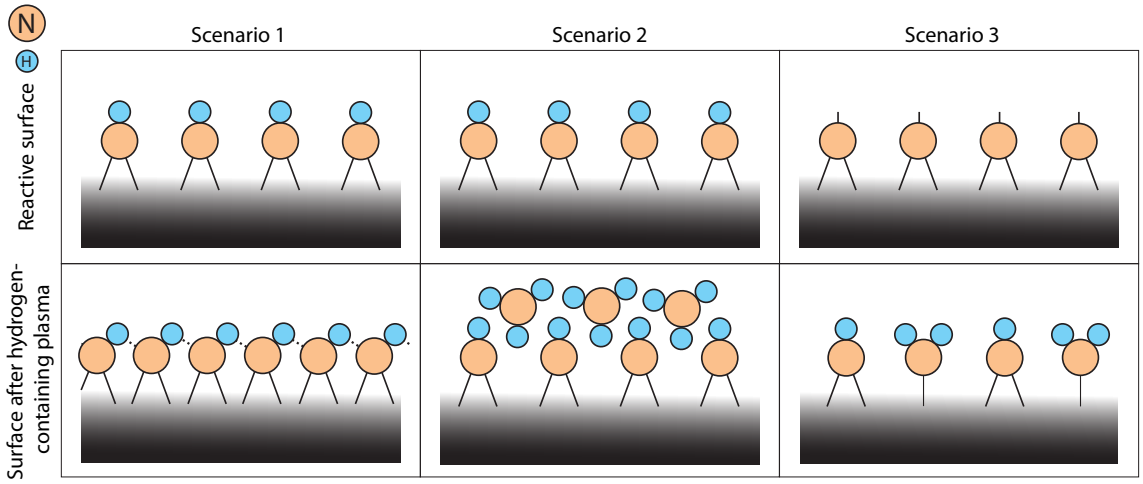

Figure 5.21: Three scenarios that could explain the blocking mechanism of hydrogen-containing plasmas, showing the main reactive surface groups in a regular ALD cycle after a pure N_2 plasma and the surface after a hydrogen-containing plasma. Scenario 1 is hydrogen bonding of the surface groups, deactivating the surface groups. Scenario 2 is the adsorption of NH_3, blocking the adsorption sites. Scenario 3 is the scenario proposed by King, who deposited silicon nitride with silane (SiH_4) and an NH_3 plasma and assumed that SiH_4 can only adsorb on dangling bonds [15].

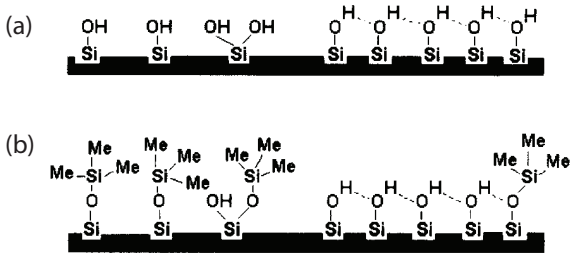

Figure 5.22: A schematic picture showing the difference between isolated hydroxyl groups (left) and a terminal hydroxyl group (right). (a) Shows the surface before precursor adsorption and (b) shows the surface after precursor adsorption [57].

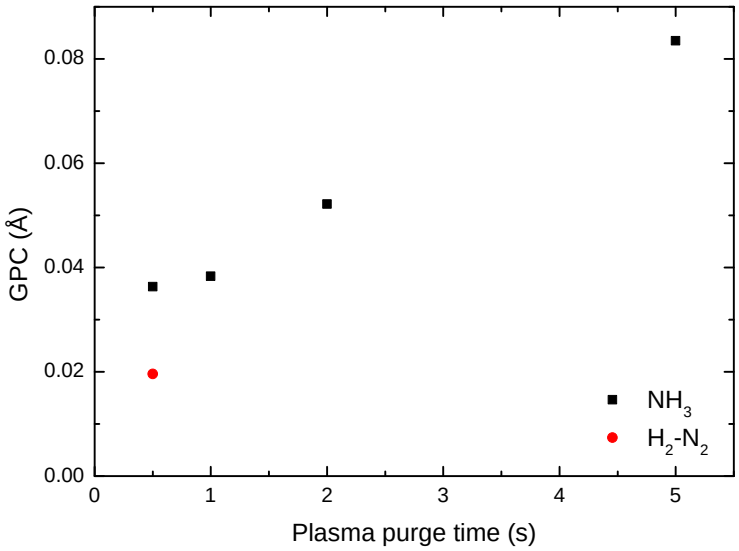

Figure 5.23: The GPC as a function of plasma purge time for an NH_3 plasma. The GPC of a H_2-N_2 plasma is added as well. The setpoint temperature is 350°C.

is less likely due to its polarity and the strong Si−H bonds in the precursor.

The first two scenarios are deemed most likely to describe the poisoning of the surface. To confirm which scenario describes the actual mechanism, more research is needed. It is important to determine the surface groups present during regular processing and during processing with hydrogen-containing plasmas to evaluate scenario 1. Scenario 2 can be investigated by adding an additional step in the normal ALD cycle. If scenario 2 is correct, the GPC should also decrease due to NH_3 adsorption when an NH_3 gas step is included after the N_2 plasma step. When the GPC is not influenced, scenario 2 can not be correct.

5.4 Summary

In this chapter the growth mechanism for the plasma-assisted ALD process for silicon nitride was investigated. The most important observations in this chapter are:

- The main reaction product during the precursor step is *t*-butylamine ($C_4H_{11}N$).
- Steric hindrance is not the limiting factor for precursor adsorption.
- Among the main reaction products during the N_2 plasma exposure are propane (C_3H_8), hydrogen cyanide (HCN), cyanogen (C_2N_2), ammonia (NH_3) and hydrogen (H_2).
- High carbon and hydrogen contents in the plasma and deposited films suggest redeposition.
- Hydrogen-containing plasmas (NH_3 and H_2-N_2) result in reduced GPCs compared to pure N_2 plasmas.
- N_2, NH_3 and H_2-N_2 plasmas can remove *t*-butylamine ligands.

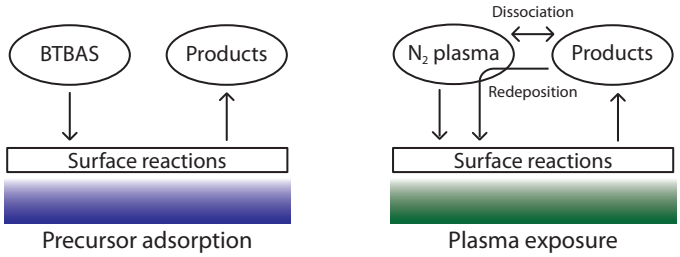

Figure 5.24: A schematic overview of the processes that are relevant for the reaction mechanism for the precursor step and the plasma step.

- Hydrogen-containing plasmas (NH_3 and H_2-N_2) poison the surface, reducing BTBAS adsorption in the next cycle.
- Nitrogen plasmas can partly undo the surface poisoning induced by NH_3 and H_2-N_2 plasmas.

The most important processes are summarized in the schematic overview in figure 5.24. In this figure the exact surface groups are unknown, because they could not be determined by the diagnostic techniques available on FlexAL2. Therefore, the exact surface reactions could not be presented, but a combination of systematic QMS and OES experiments were performed to get more insight into the surface groups and their influence on the reaction mechanism.

During the precursor adsorption, BTBAS reacts with the surface and *t*-butylamine is the only reaction product that is observed with QMS. In the plasma step there are more processes playing a role. The reactive species in the nitrogen plasma remove (parts of the) BTBAS ligands (*t*-butylamine and hydrogen) that remain on the surface after the precursor adsorption. These reaction products can be dissociated in the plasma to form new species (molecules, radicals and ions). These species can redeposit on the surface, which was suggested by the presence of Si−C bonds in the XPS data and the increase of CN emission for increasing plasma pressure. The redeposited species can be removed again during the remaining plasma exposure time. The products detected during the plasma step can result from any of these processes. Reaction products that are detected with QMS are *t*-butylamine, cyanogen, propane, hydrogen cyanide, ammonia and hydrogen.

Using hydrogen-containing plasmas (NH_3 or H_2-N_2) results in reduced GPCs, even though these plasmas might remove more *t*-butylamine ligands than nitrogen plasmas do. It is shown that these plasmas poison the surface, preventing BTBAS adsorption in the next cycle. A nitrogen plasma can undo this poisoning partly. Three scenarios were described that could explain the nature of the poisoning mechanism and provide insight in the surface groups that can be present. To determine the exact surface groups, these scenarios need to be investigated further.

Chapter 6

Conclusions & outlook

6.1 Conclusions

The main goal of this work was the deposition of silicon nitride with a plasma-assisted atomic layer deposition process in a wide temperature window. A plasma-assisted ALD process with reasonable growth per cycle (GPC) was developed with the metalorganic precursor BTBAS and a N_2 plasma, since the hydrogen-containing plasmas NH_3 and H_2-N_2 resulted in very low GPCs. The key feature of ALD, two self-limiting half-reactions, was investigated by the determination of the GPC as a function of precursor dosing, precursor purge, plasma exposure and plasma purge time and these curves confirmed the saturation behavior. The initial growth did not show any delay but a small growth enhancement for the first cycles. A standard recipe was proposed and the composition of the resulting film was measured by XPS. The N/Si ratio was relatively high, as was the carbon content. After the development of the process, the research focused on answering the research questions concerning the temperature window, the material properties and the growth mechanism.

Due to the importance of the deposition temperature, the relation between setpoint temperature and wafer temperature was investigated. It was shown that in general the temperature of the wafer in vacuum systems was lower than the setpoint temperature of the reactor. The thermal contact could be enhanced with a helium backflow or by an increase of the reactor pressure. At FlexAL2, the deposition tool for the silicon nitride ALD process, there was no helium backflow available. Since the maximum allowed wall temperature was 150°C, the substrate temperature deviated significantly from the setpoint temperature for high temperatures. The difference between wafer temperature and setpoint temperature depended on the processing gases, their flow rates and the pressure. A calibration with *in situ* SE is needed to determine the relation between these parameters for experiments without the possibility of *in situ* SE measurements. In this work no calibration was used because *in situ* SE measurements were used to control the substrate temperature.

The temperature window that resulted in films with good quality was 200°C-500°C (setpoint temperature), where LPCVD generally requires temperatures above 700°C. ALD behavior was also obtained for a temperature of 100°C, but the resulting film oxidized rapidly after removal from the reactor. Optimization of the low-temperature process parameters might improve the material quality further. Compared to other silicon nitride ALD processes reported in literature, the temperature window for ALD of silicon nitride was extended further towards lower temperatures in this work. This is important for applications where a low thermal budget is required.

The film quality was investigated as a function of the process parameters plasma exposure

time, deposition temperature and plasma pressure. The material properties improved for increasing plasma exposure time, increasing temperature and decreasing pressure, while the GPC decreased at the same time. The refractive index, N/Si ratio and mass density reached values close to those of stoichiometric Si_3N_4 and the carbon and hydrogen contents decreased. The uniformity of thickness and refractive index improved with increasing temperature as well. Also, the long-term stability of the films improved and for plasma exposure times ≥ 7.5 seconds, temperatures ≥ 200°C and pressures ≤ 40 mTorr the films did hardly show any signs of oxidation two months after they were deposited. Films deposited at 100°C and a pressure of 10 mTorr showed improved properties compared to the films deposited at 40 mTorr at the same temperature. Variation of other process parameters (e.g., plasma exposure time) might improve the low-temperature film properties even further.

Compared to silicon nitride ALD processes with metal halide precursors reported in literature, the GPC in this work was relatively low ($\approx$10 times less than for metal halide precursors), but the cycle times were considerably shorter ($\approx$100-600 times). Furthermore, the hydrogen content in the deposited films in this work was lower than that reported for the metal halide precursors or for PECVD processes, providing films that would likely cause less device degradation in microelectronics. ALD processes reported in literature for metalorganic or metal hydride precursors resulted in films with a relatively low refractive index, which could suggest oxidation of the films. In this work, it was shown that post-oxidation could be avoided when appropriate deposition parameters were used.

The reaction products were determined by combination of QMS signals and compared with listed mass spectra to provide insight into the reaction mechanisms. The main reaction product during the precursor step was the *t*-butylamine ligand of BTBAS and it was found that the adsorption of BTBAS was not limited by steric hindrance. During the N_2 plasma exposure step the reaction products released from the surface could interact with the plasma, resulting in new plasma species and redeposition. The main products detected were cyanogen, propane, hydrogen cyanide, ammonia and hydrogen. Since the reaction products in the plasma exposure step contained *t*-butylamine ligand fragments, it was assumed that BTBAS adsorbed monofunctionally during the precursor step and that the other *t*-butylamine ligand was removed by the nitrogen plasma.

The hydrogen-containing plasmas NH_3 and H_2-N_2 resulted in reduced GPCs compared to a N_2 plasma. The effects of hydrogen, when added to the plasma, were investigated with OES by performing a set of experiments with plasmas with different hydrogen to nitrogen ratios and consecutive plasma steps in one ALD cycle. The hydrogen-containing plasmas were able to remove *t*-butylamine ligands, but poisoned the surface, which limited precursor adsorption in the next cycle. N_2 plasmas could remove the poisoning partly. Three reaction mechanisms that could explain the poisoning mechanism were described.

6.2 Outlook

A few recommendations for future research to further improve the material properties and to obtain a better insight into the reaction mechanisms will be given in this section.

As already mentioned in chapter 4, the material properties for the low-temperature process could be optimized further. This can be done by a combination of longer plasma exposure times and using a lower plasma pressure, and might result in an extension of the temperature window towards lower deposition temperatures. Also, capping the low-temperature silicon nitride layer could be studied further to investigate whether the capping layer can avoid post-oxidation of the silicon nitride layer.

Since the maximum allowed wall temperature of the reactor is 150°C, the actual wafer temperature is well below the setpoint temperature for setpoint temperatures above 150°C. Therefore, the high-temperature process should be investigated with wall temperatures equal to the setpoint temperatures, such that the process can be investigated at wafer temperatures up to 500°C. This could also be important in relation to the redeposition processes, since the deposition on the low-temperature walls results in more carbon and hydrogen in the plasma, which enhances redeposition. For QMS measurements a wall temperature corresponding to the setpoint temperature would lead to better insight into the surface reactions at the substrate, since the deposition at surfaces with the same temperature will be alike.

The material properties of the silicon nitride films deposited in this work provide potential for application in microelectronics. Therefore, conformality in 3D structures should be investigated. For some applications it is important that etching in 3D structures only removes the silicon nitride film at the bottom of the structures, while the film deposited on the walls is not removed. Low isotropic etch rates are then desired to limit etching of the film on the walls. This can be achieved with a plasma etch, where the directionality of the ions in the plasma leads to anisotropic etching, mainly removing the film at the bottom of the trench. The etch-resistance of the material can be investigated with wet etch tests (in 3D structures). The conformality and the wet etch rate are already under investigation in a follow-up project.

Although a large amount of information on surface processes can be deduced from experiments using QMS and OES, gaining more insight in the reaction mechanism can be achieved by studying the surface groups with *in situ* FTIR spectroscopy. Using FTIR spectroscopy, surface groups can be studied directly, for both the normal ALD cycle and the ALD cycles with hydrogen-containing plasmas (in combination with a nitrogen plasma). The influence of ammonia can also be further investigated by incorporation of an NH_3 gas step in the normal ALD cycle and investigating the effect on the GPC.

Appendix A

Plasma-assisted atomic layer deposition of silicon dioxide

As a first test a plasma-assisted ALD process for silicon dioxide (SiO_2), with BTBAS as the precursor and O_2 as the reactant, was investigated. The saturation curves were determined by SE thickness measurements. The SiO_2 layer was modelled with a Cauchy model. The deposition conditions for the determination of the saturation curves are listed in table A.1 and the resulting saturation curves are shown in figure A.1.

Table A.1: The deposition conditions for the determination of the saturation curves for the plasma-assisted ALD process of SiO_2.

	Saturation curve for:			
Deposition parameter	BTBAS dose time	Precursor purge time	Plasma time	Plasma purge time
Temperature (°C)	250	250	250	250
BTBAS dose time (ms)	varied	100	100	100
Reaction step (s)	1	1	1	1
Precursor purge time (s)	2.5	varied	0.1	0.1
Plasma exposure time (s)	5	5	varied	5
O_2 plasma flow (sccm)	100	100	100	100
Plasma pressure (mTorr)	25	25	25	25
Plasma power (W)	200	200	200	200
Plasma purge time (s)	1	1	0.5	varied

The GPC as a function of BTBAS dose time (figure A.1a) showed an ALD and a small CVD component, which might be due to too short purge times for longer dose times. GPCs up to 1.2 Å were determined, compared to the 1.37 Å reported by Fang *et al.* [18]. For precursor purge times $\geq$ 250 ms the GPC saturated, as shown in figure A.1b. Figure A.1c shows that the GPC saturated for plasma exposure times $\geq$ 750 ms and even seemed to decrease a little for longer plasma exposure times. Plasma purge times longer than 100 ms did not influence the GPC, as is shown in figure A.1d. The deposition process could be optimized and investigated further for other deposition parameters (e.g., temperature, plasma power, flow rates and plasma pressure).

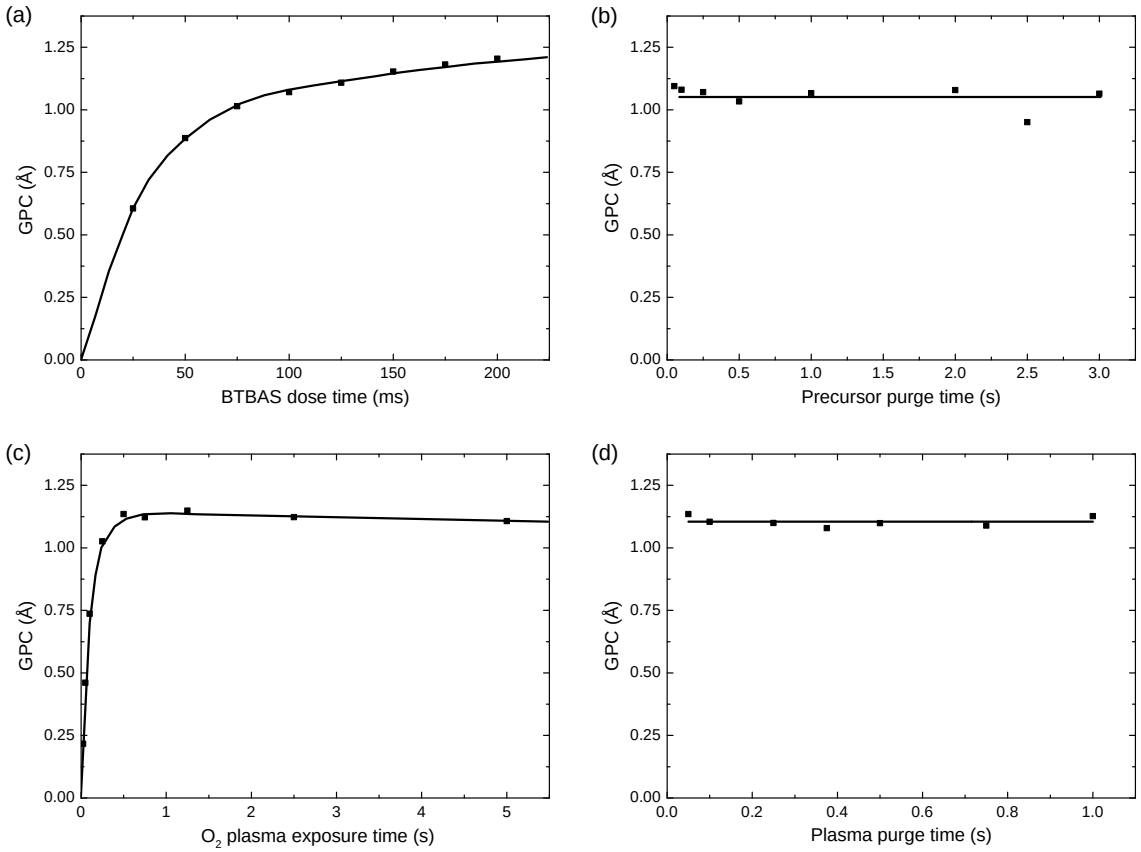

Figure A.1: The saturation curves for the SiO_2 process, showing the GPC as a function of (a) BTBAS dose time, (b) precursor purge time, (c) plasma exposure time and (d) plasma purge time. All lines serve as a guide to the eye.

Appendix B

Plasma-assisted atomic layer deposition of silicon nitride on HF-dipped wafers

The initial growth on HF-dipped wafers was investigated for the standard condition listed in table 4.2, with exception of the plasma exposure time, which was set to 10 seconds. Due to the HF dip, the XPS depth profile of the film did not show a native oxide layer (i.e., an increase of oxygen concentration on top of the silicon substrate), as shown in figure B.1.

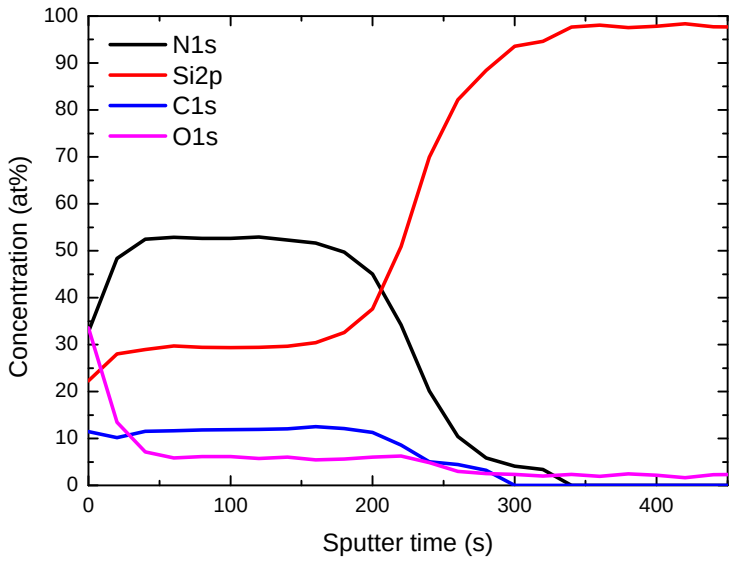

Figure B.1: The XPS depth profile for a silicon nitride film deposited on an HF-dipped wafer at 200°C.

Figure B.2 shows the thickness as a function of the number of deposition cycles. It can be seen that the growth started immediately and that there was an enhancement of the growth in the first cycles, as indicated by the intercept with the y-axis. This enhancement is expected to be nitridation of the substrate, which adds to the total thickness of the silicon nitride film.

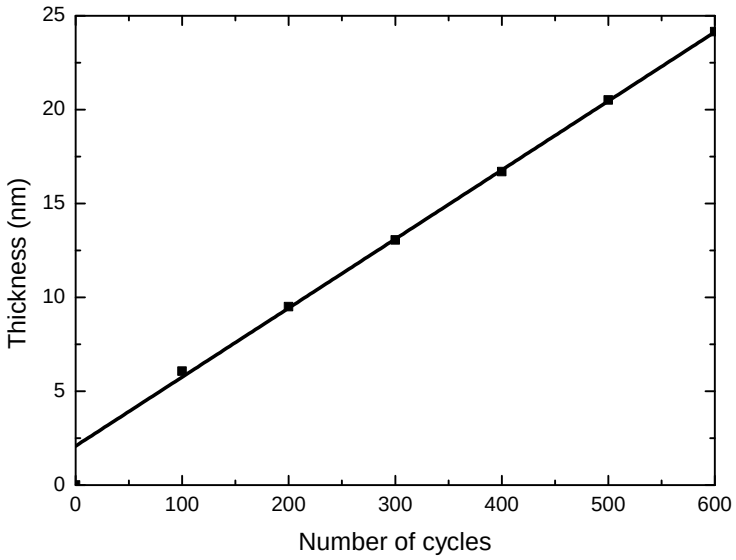

Figure B.2: The thickness as a function of the number of deposition cycles for a silicon nitride film deposited on an HF-dipped wafer. The black line is an extrapolated fit of the linear part of the data.

Appendix C

XPS analysis

This appendix shows the XPS data that was used to obtain the concentrations of the elements nitrogen, silicon, carbon and oxygen for the variation of the process parameters plasma exposure time, deposition temperature and plasma pressure. Also, the binding energies for these elements will be compared to the NIST X-ray Photoelectron Spectroscopy database [25]. The peak areas of the deconvoluted peaks will be shown as well.

C.1 Plasma exposure time series

The XPS depth profiles for an increasing plasma exposure time are shown in figure C.1. For the determination of the concentrations only the bulk of the film was taken into account. It can be seen that the nitrogen content was approximately constant for all plasma exposure times, but that the silicon content increased for increasing plasma exposure time. The carbon content decreased for increasing plasma exposure time, while the oxygen content slightly increased.

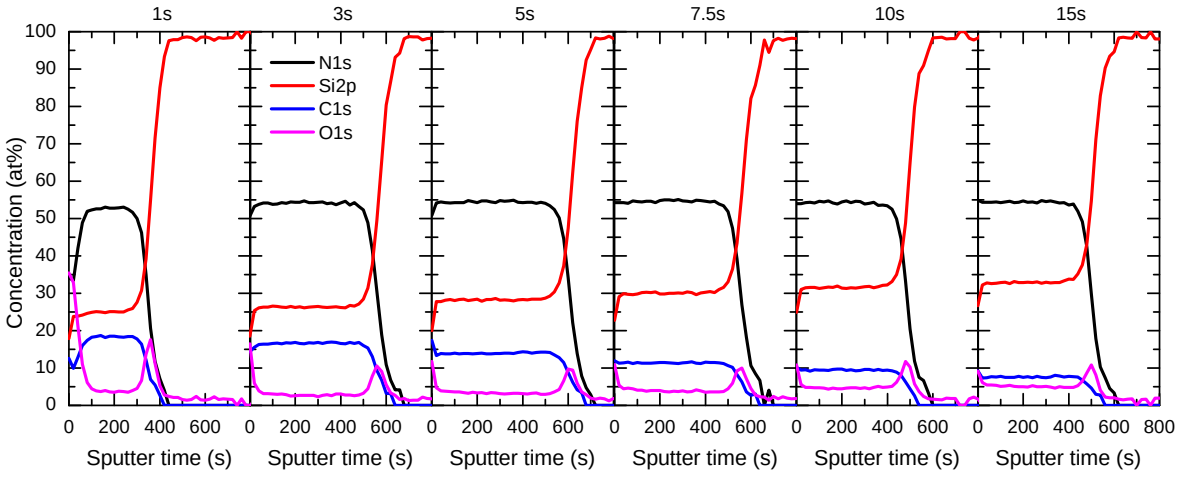

Figure C.1: The XPS depth profiles for the elements nitrogen, silicon, carbon and oxygen for a variation of plasma exposure time.

For the plasma exposure time series the binding energies were already plotted in figure 4.8. The areas of the deconvoluted peaks are shown in figure C.2. The number of silicon-nitride bonds increased for increasing plasma exposure time, as did the hydroxide bonds. All carbon

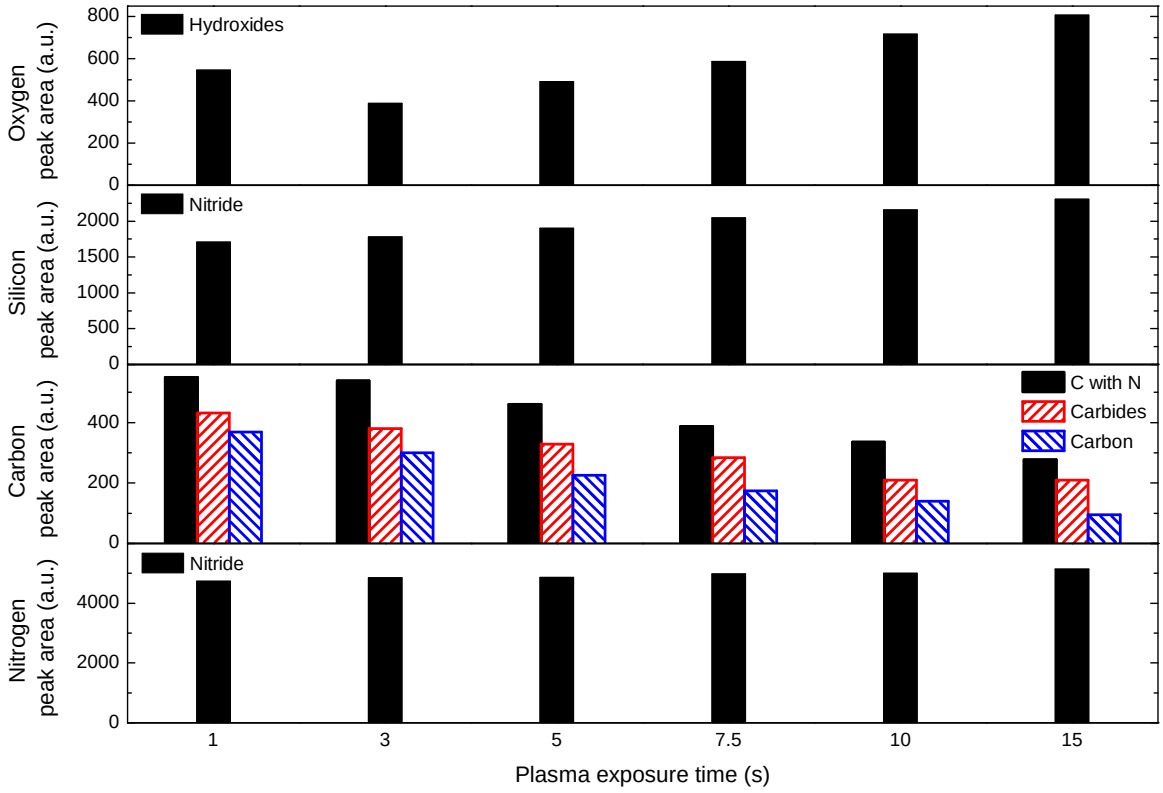

Figure C.2: The peak areas of the deconvoluted peaks for the plasma time series.

bonds decreased in number for increasing plasma exposure time, but the carbon-carbon bond density decreased the most.

C.2 Temperature series

Figure C.3 shows the depth profiles for a varying deposition temperature. The nitrogen and oxygen contents were approximately constant, while the silicon content increased for increasing deposition temperature. The carbon content decreased for increasing temperature. Surface oxidation of the films was reduced for increasing temperature.

The binding energies for the four measured elements are shown in figure C.4 and compared to the values in the NIST X-ray Photonelectron Spectroscopy database [25]. Silicon and nitrogen were mainly bonded to each other and the oxygen was incorporated due to impurities in the reactor and the gases. At temperatures $\leq 200°C$ carbon could be bonded to silicon, nitrogen and carbon, but for higher temperatures the carbon-carbon bond disappeared. The reduction of carbon content for increasing temperatures was also observed in the areas of the deconvoluted peaks, as was the increase in silicon-nitride bonds, as shown in figure C.5. Due to a reduction in carbon content and an increase in silicon content, the environment became less electronegative for increasing temperatures, resulting in a shift towards lower binding energies for increasing deposition temperatures in figure C.4.

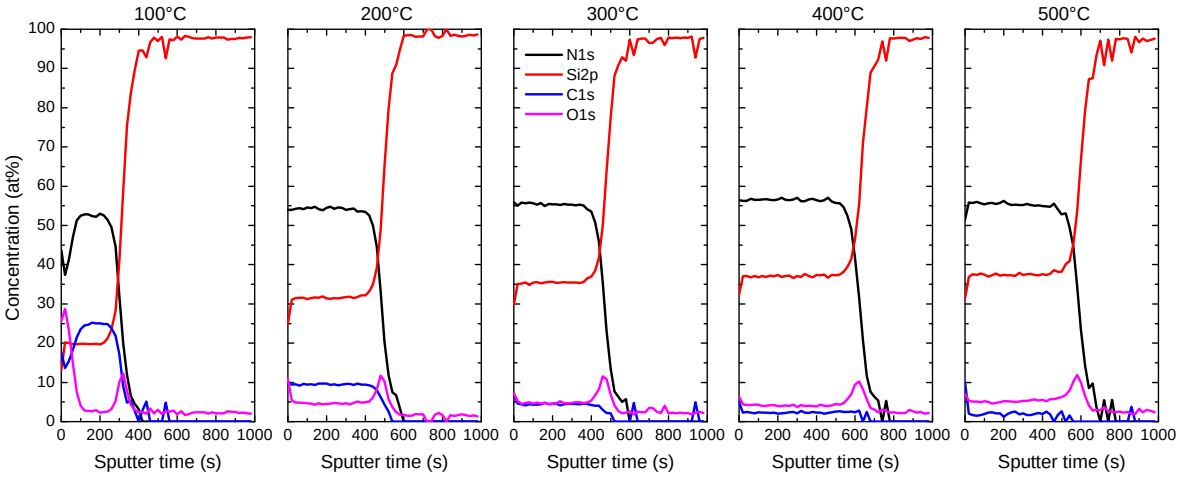

Figure C.3: The XPS depth profiles for the elements nitrogen, silicon, carbon and oxygen for a variation of deposition temperature.

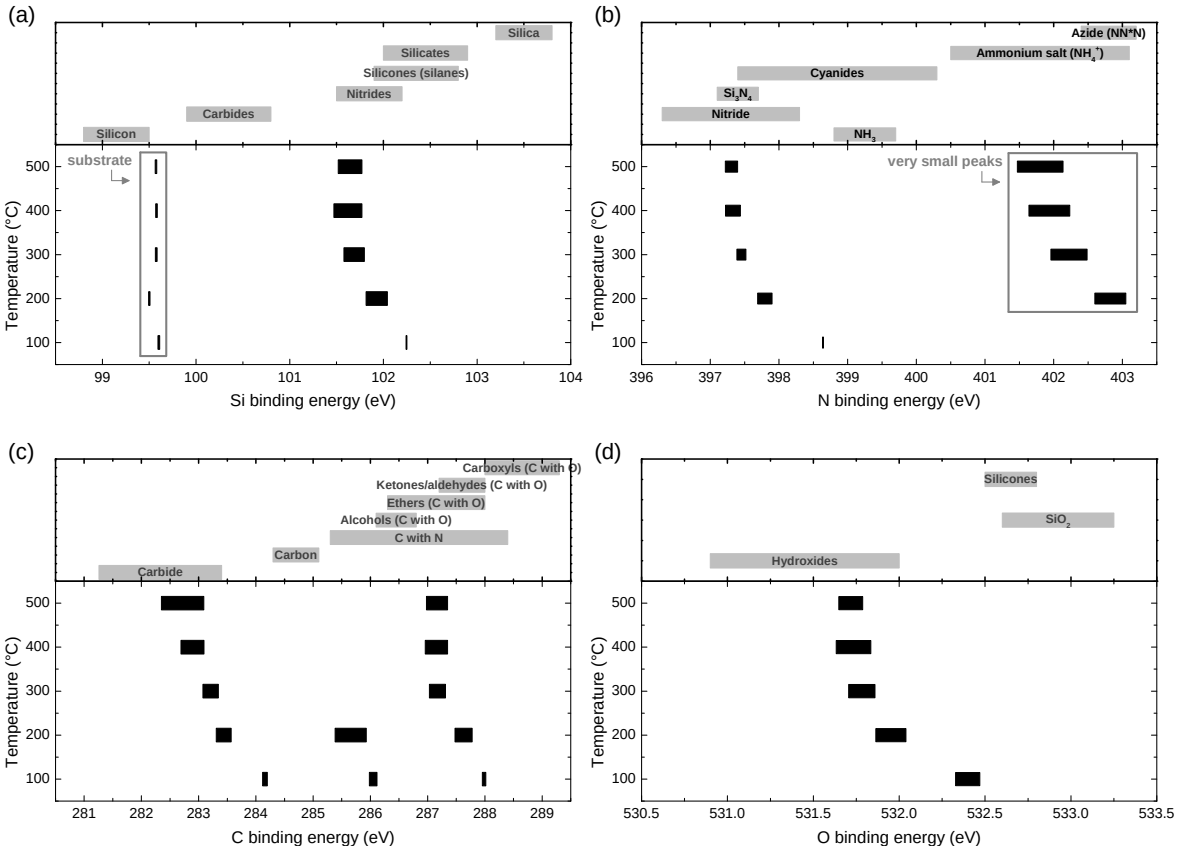

Figure C.4: The binding energies for the elements (a) silicon, (b) nitrogen, (c) carbon and (d) oxygen for a variation of temperature and the reference values for the investigated ranges from the NIST X-ray Photoelectron Spectroscopy database [25]. The width of the bars indicates the range in which the binding energy for a specific peak can occur.

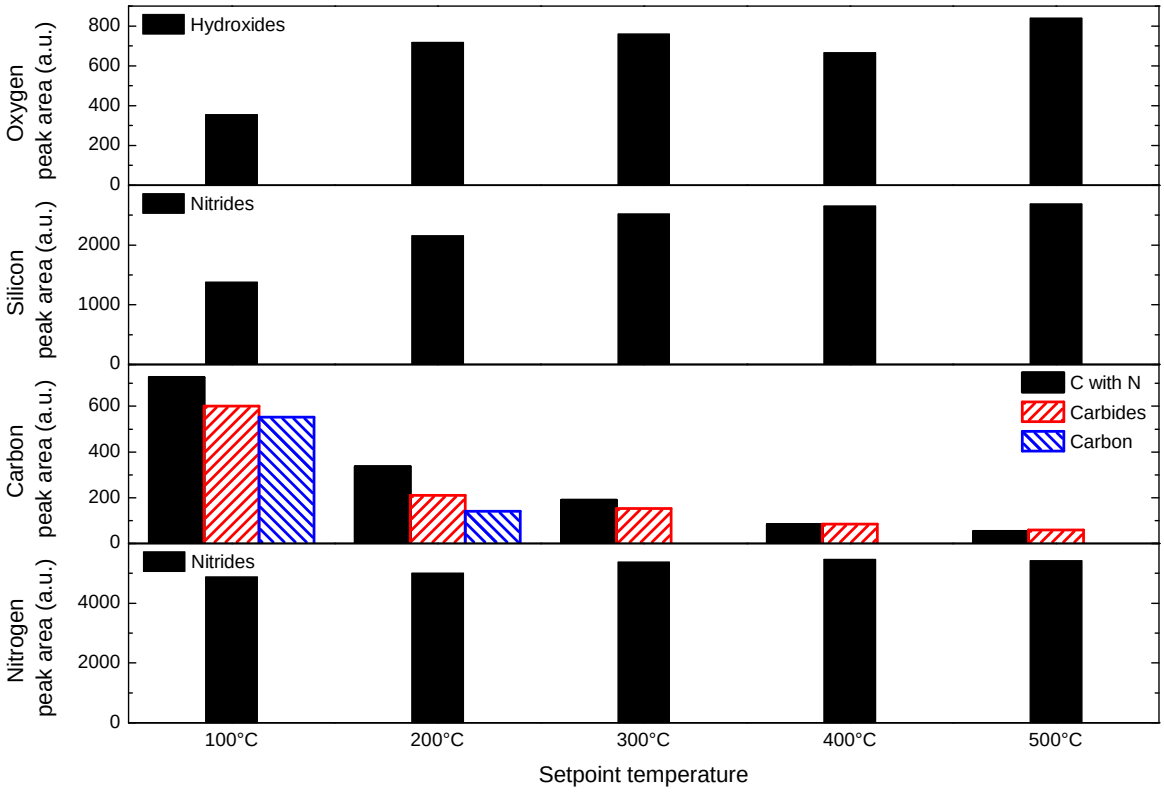

Figure C.5: The peak areas of the deconvoluted peaks for the variation of deposition temperature.

C.3 Plasma pressure series

The XPS depth profiles for the pressure series are shown in figure C.6 for a deposition temperature of 100°C and 200°C. The silicon and nitrogen content decreased for increasing pressure, while the carbon content increased. At 100°C the changes were more significant than at 200°C.

The binding energies as a function of plasma pressure are shown in figure C.7 and C.8 for a deposition temperature of 200°C and 100°C respectively. The areas of the corresponding deconvoluted peaks are shown in figure C.9 for both deposition temperatures. They show that silicon and nitrogen were mainly bonded to each other and that carbon was bonded to nitrogen, silicon and carbon. The number of carbon-carbon bonds decreased for decreasing plasma pressure and for a temperature of 200°C they disappeared completely for a pressure of 10 mTorr. The silicon-nitrogen bond density increased for decreasing pressure. For decreasing plasma pressures the binding energies shifted towards lower binding energies.

For the film deposited at a temperature of 200°C and a pressure of 70 mTorr, the XPS depth profiles directly after deposition and one month after deposition are shown in figure C.10. They show the penetration of oxygen in the film over time and the resulting oxidation front was responsible for the decrease in refractive index, as shown in figure 4.21.

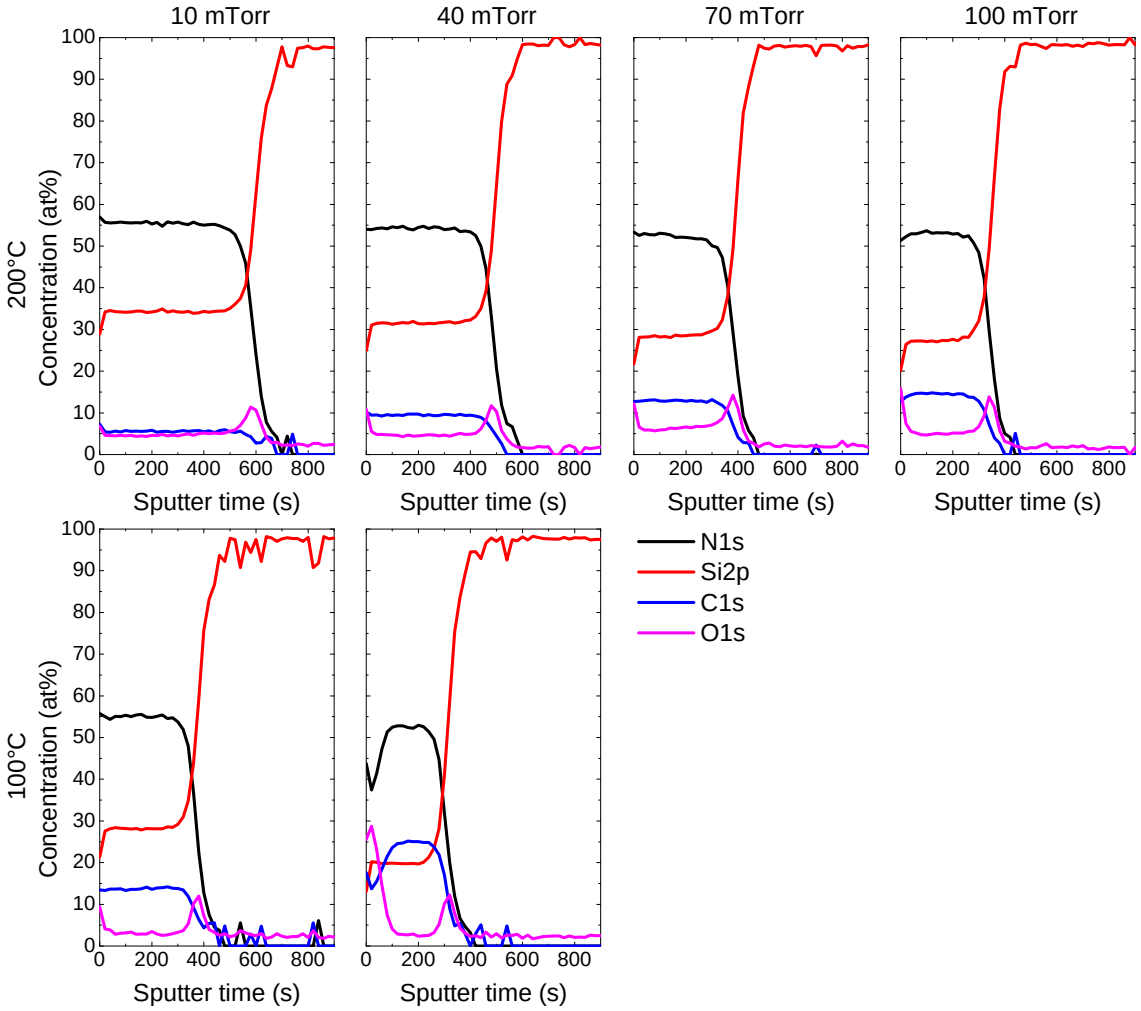

Figure C.6: The depth profiles for varying plasma pressure for a temperature of 200°C (top) and 100°C (bottom).

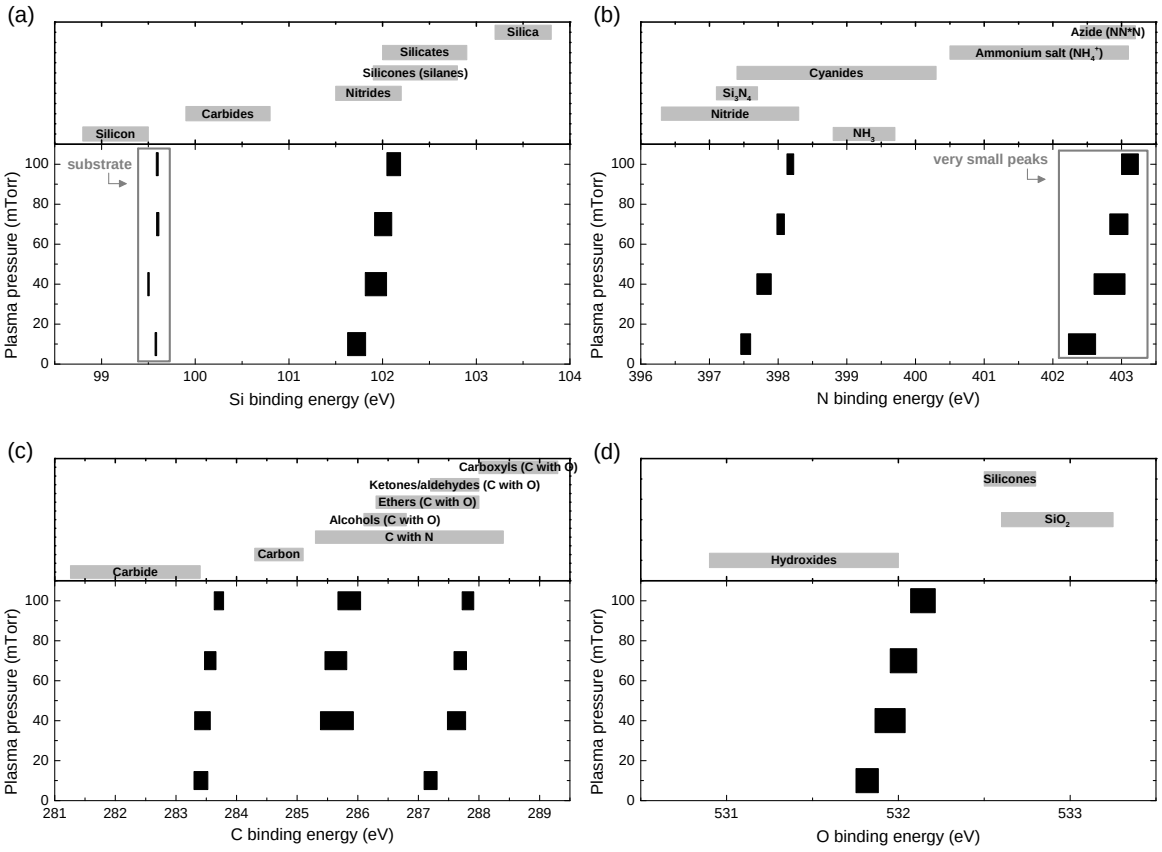

Figure C.7: The binding energies for the elements (a) silicon, (b) nitrogen, (c) carbon and (d) oxygen for a variation of plasma pressure at 200°C and the reference values for the investigated ranges from the NIST X-ray Photoelectron Spectroscopy database [25]. The width of the bars indicates the range in which the binding energy for a specific peak can occur.

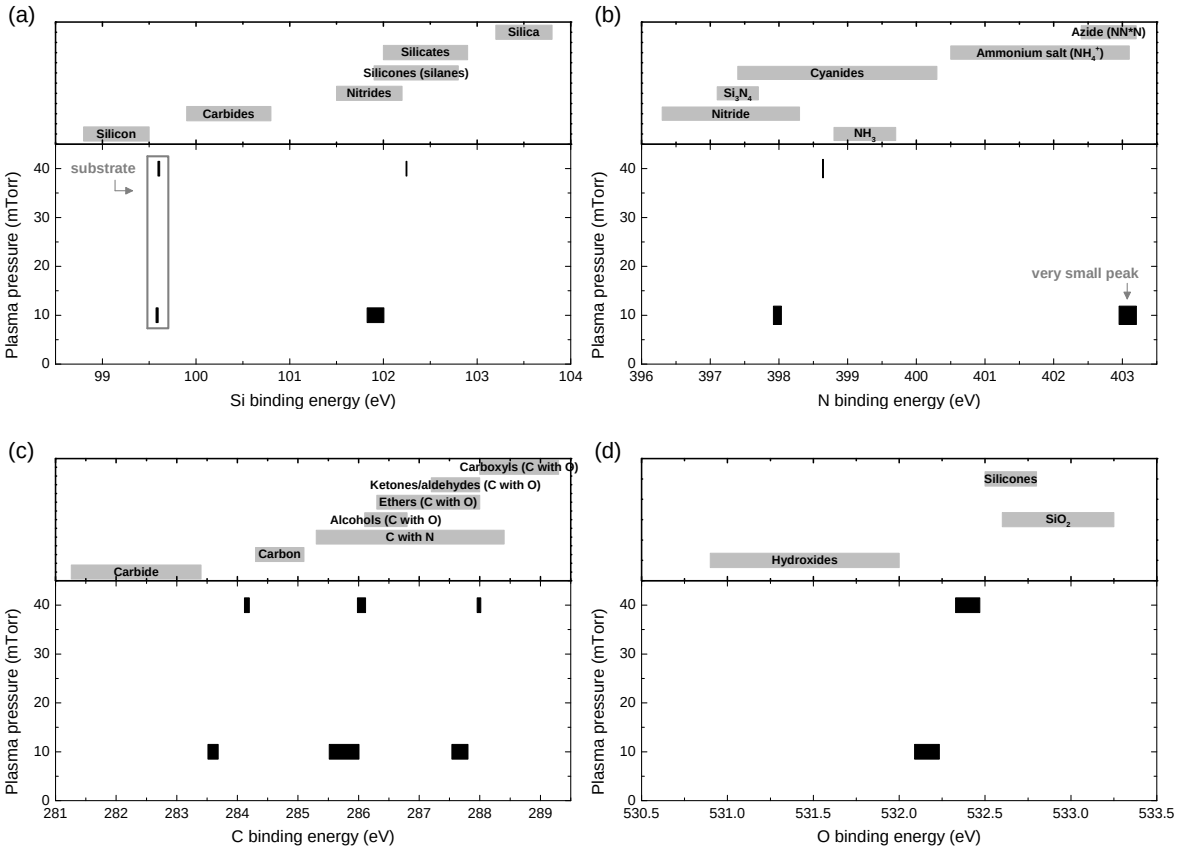

Figure C.8: The binding energies for the elements (a) silicon, (b) nitrogen, (c) carbon and (d) oxygen for a variation of plasma pressure at 100°C and the reference values for the investigated ranges from the NIST X-ray Photoelectron Spectroscopy database [25]. The width of the bars indicates the range in which the binding energy for a specific peak can occur.

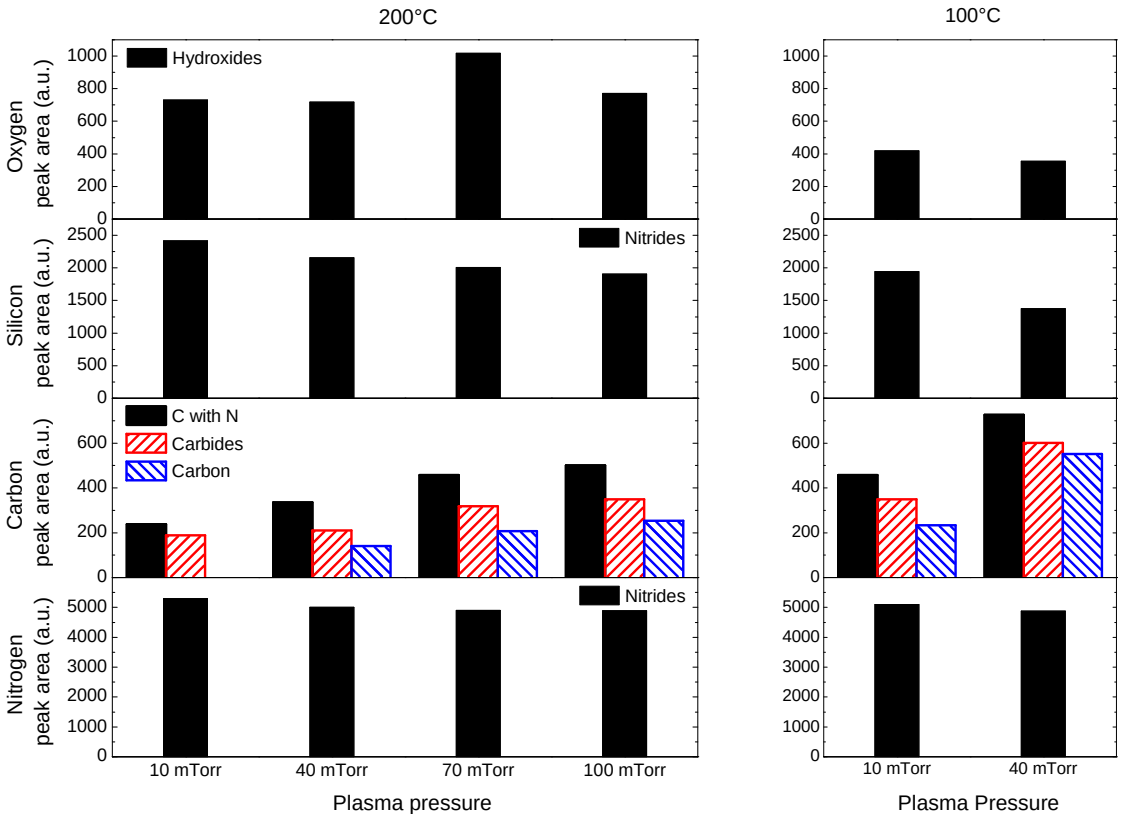

Figure C.9: The peak areas of the deconvoluted peaks for a variation of plasma pressure for temperatures of 200°C (left) and 100°C (right).

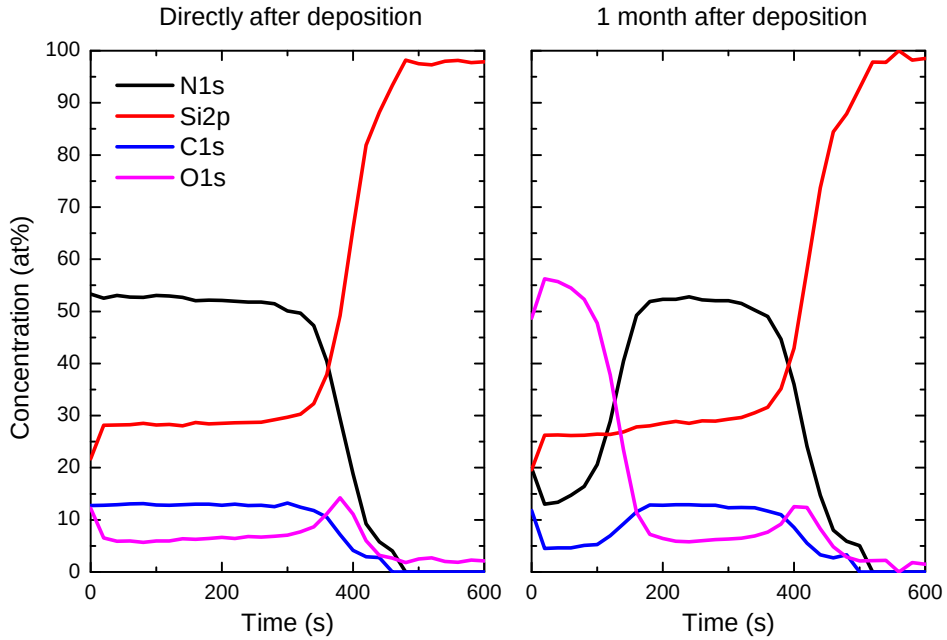

Figure C.10: The XPS depth profiles for the film deposited at 200°C and 70 mTorr directly after deposition (left) and one month later (right). The formation of an oxidation front can be seen.

Appendix D

Uniformity

D.1 Thickness uniformity for a low-pressure plasma

The thickness uniformity of the film deposited at 200°C and 10 mTorr is shown in figure D.1. The film thickness was very uniform.

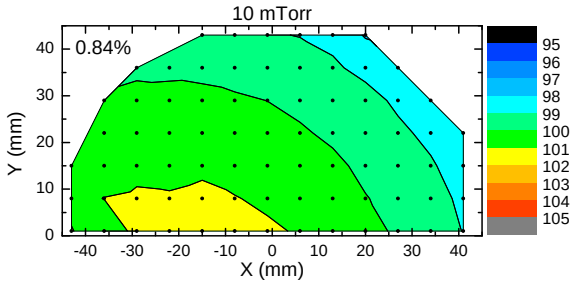

Figure D.1: The film thickness across the wafer relative to its average thickness for the film deposited at a temperature of 200°C and plasma pressure of 10 mTorr. The black dots indicate the data points and the percentage in the graph is the non-uniformity.

D.2 Uniformity of refractive index

Figure D.2 shows the uniformity of the refractive index for films deposited with 10 and 15 seconds plasma exposure times. The uniformity for both films was excellent.

The uniformity of the refractive index for films deposited at temperatures of 100°C and 300°C-500°C are shown in figure D.3. These plots show a very uniform refractive index with non-uniformities less than 1%.

For the film deposited at 200°C and a pressure of 10 mTorr the uniformity of the refractive index is shown in figure D.4, showing an excellent uniformity.

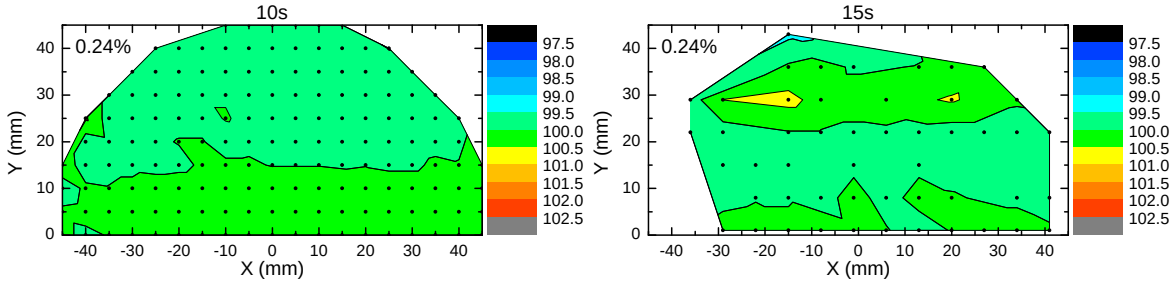

Figure D.2: The refractive index relative to the average refractive index for films deposited at 200°C and a plasma exposure times of 10 and 15 seconds. The black dots indicate the data points and the percentage in the graph is the non-uniformity.

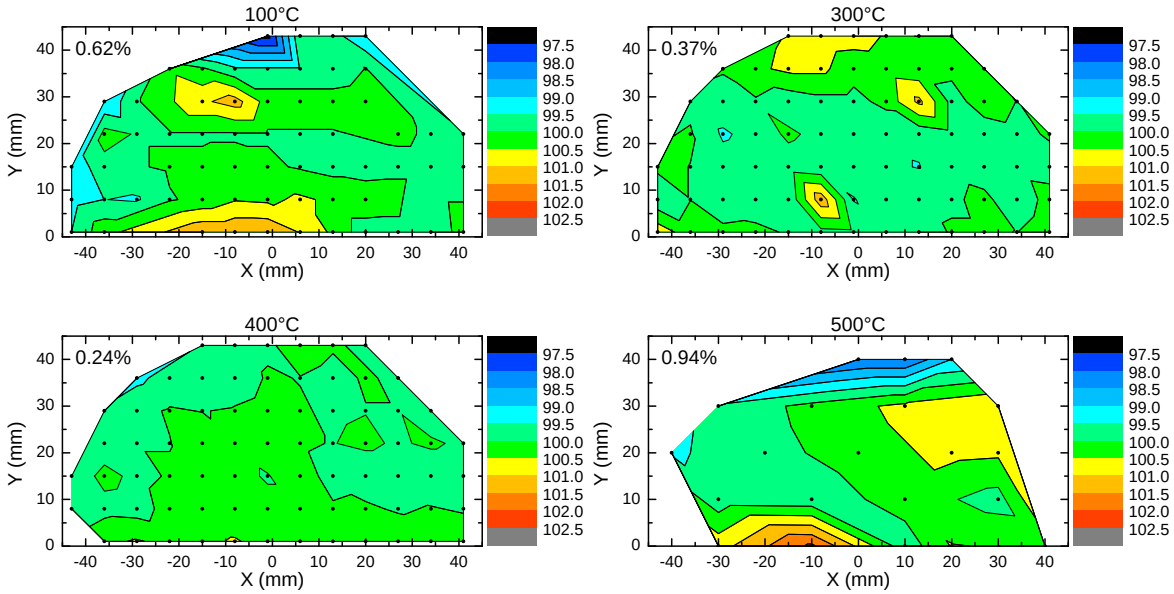

Figure D.3: The refractive index relative to the average refractive index for films deposited at 100°C and 300°C-500°C. The black dots indicate the data points and the percentages in the graphs are the non-uniformities.

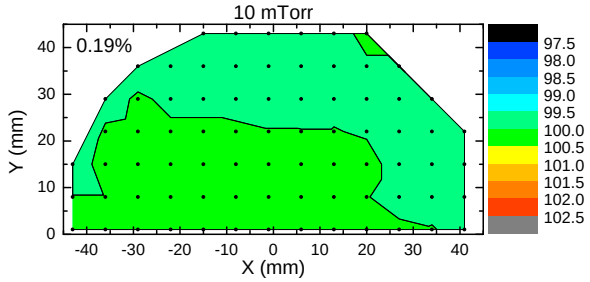

Figure D.4: The refractive index across the wafer relative to the average refractive index for the film deposited at a temperature of 200°C and plasma pressure of 10 mTorr. The black dots indicate the data points and the percentage in the graph is the non-uniformity.

Bibliography

[1] W. M. M. Kessels, J. Hong, F. J. H. van Assche, J. D. Moschner, T. Lauinger, W. J. Soppe, A. W. Weeber, D. C. Schram, and M. C. M. van de Sanden, *High-rate deposition of a-SiN_x:H for photovoltaic applications by the expanding thermal plasma*, Journal of Vacuum Science & Technology A: Vacuum, Surfaces, and Films **20** (5), 1704-1715 (2002).

[2] H. Cho, P. Kapur, P. Kalavade, and K. Saraswat, *A Novel Spacer Process for Sub-10-nm-Thick Vertical MOS and Its Integration With Planar MOS Device*, IEEE Transactions on Nanotechnology **5** (5), 554-563 (2006).

[3] K. Park, W.-D. Yun, B.-J. Choi, H.-D. Kim, W.-J. Lee, S.-K. Rha, and C. O. Park, *Growth studies and characterization of silicon nitride thin films deposited by alternating exposures to Si_2Cl_6 and NH_3*, Thin Solid Films **517** (14), 3975-3978 (2009).

[4] F. Koehler, D. H. Triyoso, I. Hussain, S. Mutas, and H. Bernhardt, *Atomic Layer Deposition of SiN for spacer applications in high-end logic devices*, IOP Conference Series: Materials Science and Engineering **41** (1), 012006 (2012).

[5] J. Gumpher, W. Bather, N. Mehta, and D. Wedel, *Characterization of Low-Temperature Silicon Nitride LPCVD from Bis(tertiary-butylamino)silane and Ammonia*, Journal of The Electrochemical Society **151** (5), G353-G359 (2004).

[6] H. B. Profijt, S. E. Potts, M. C. M. van de Sanden, and W. M. M. Kessels, *Plasma-Assisted Atomic Layer Deposition: Basics, Opportunities, and Challenges*, Journal of Vacuum Science & Technology A: Vacuum, Surfaces, and Films **29** (5), 050801 (2011).

[7] J. Yota, J. Hander, and A. A. Saleh, *A comparative study on inductively-coupled plasma high-density plasma, plasma-enhanced, and low pressure chemical vapor deposition silicon nitride films*, Journal of Vacuum Science & Technology A: Vacuum, Surfaces, and Films **18** (2), 372-376 (2000).

[8] S.-S. Han, B.-H. Jun, K. No, and B.-S. Bae, *Preparation of a-SiN_x Thin Film with Low Hydrogen Content by Inductively Coupled Plasma Enhanced Chemical Vapor Deposition*, Journal of The Electrochemical Society **145** (2), 652-658 (1998).

[9] C. Di Franco, N. Cioffi, N. Ditaranto, M. Vitiello, M. Sibilano, L. Torsi, and G. Scamarcio, *Plasma treatment effects on Si and Si/dielectric film heterostructures*, Journal of Materials Processing Technology **206** (13), 462-466 (2008).

[10] J. Klaus, A. Ott, A. Dillon, and S. George, *Atomic layer controlled growth of Si_3N_4 films using sequential surface reactions*, Surface Science **418** (1), L14-L19 (1998).

[11] S. Yokoyama, H. Goto, T. Miyamoto, N. Ikeda, and K. Shibahara, *Atomic layer controlled deposition of silicon nitride and in situ growth observation by infrared reflection absorption spectroscopy*, Applied Surface Science **112** (0), 75-81 (1997).

[12] S. Yokoyama, N. Ikeda, K. Kajikawa, and Y. Nakashima, *Atomic-layer selective deposition of silicon nitride on hydrogen-terminated Si surfaces*, Applied Surface Science **130-132**, 352-256 (1998).

[13] H. Goto, K. Shibahara, and S. Yokoyama, *Atomic layer controlled deposition of silicon nitride with self-limiting mechanism*, Applied Physics Letters **68** (23), 3257-3259 (1996).

[14] R. K. Laxman, T. D. Anderson, and J. A. Mestemacher, *Materials: A low-temperature solution for silicon nitride deposition*, Solid State Technology **43** (4) (2000).

[15] S. W. King, *Plasma enhanced atomic layer deposition of SiN_x:H and SiO_2*, Journal of Vacuum Science & Technology A: Vacuum, Surfaces, and Films **29** (4), 041501 (2011).

[16] S. Sze and K. K. Ng, *Physics of Semiconductor Devices*, 3rd ed., John Wiley & Sons (2007).

[17] H.-J. Wang and Y. Fu, *Designing new free-radical reducing reagents: Theoretical study on SiH bond dissociation energies of organic silanes*, Journal of Molecular Structure: THEOCHEM **893** (13), 67-72 (2009).

[18] Q. Fang, T. Sharp, C. Hodson, and A. Peter, *Remote Plasma ALD Growth of SiO_2 and SiN_x films using four aminosilane precursors*, Poster presentation at AVS ALD conference Dresden (2012).

[19] E. Langereis, S. B. S. Heil, H. C. M. Knoops, W. Keuning, M. C. M. van de Sanden, and W. M. M. Kessels, *In situ spectroscopic ellipsometry as a versatile tool for studying atomic layer deposition*, Journal of Physics D: Applied Physics **42** (7), 073001 (2009).

[20] H. Fujiwara, *Spectroscopic Ellipsometry: Principles and Applications*, John Wiley & Sons (2007).

[21] G. E. Jellison Jr. and F. A. Modine, *Parameterization of the optical functions of amorphous materials in the interband region*, Applied Physics Letters **69** (3), 371-373 (1996).

[22] G. E. Jellison Jr. and F. A. Modine, *Erratum: "Parameterization of the optical functions of amorphous materials in the interband region" [Appl. Phys. Lett. **69**, 371 (1996)]*, Applied Physics Letters **69** (14), 2137-2137 (1996).

[23] H. C. M. Knoops, E. Langereis, M. C. M. van de Sanden, and W. M. M. Kessels, *Reaction mechanisms of atomic layer deposition of TaN_x from $Ta(NMe_2)_5$ precursor and H_2-based plasmas*, Journal of Vacuum Science & Technology A: Vacuum, Surfaces, and Films **30** (1), 01A101 (2012).

[24] NIST Chemistry WebBook, http://webbook.nist.gov/chemistry/.

[25] NIST X-ray Photoelectron Spectroscopy Database, http://srdata.nist.gov/xps/.

[26] AccTec B.V., http://www.acctec.nl/.

[27] P. Vandenabeele and K. Maex, *Influence of temperature and backside roughness on the emissivity of Si wafers during rapid thermal processing*, Journal of Applied Physics **72** (12), 5867-5875 (1992).

[28] P. J. Timans, *Emissivity of silicon at elevated temperatures*, Journal of Applied Physics **74** (10), 6353-6364 (1993).

[29] B. Sopori, W. Chen, J. Madjdpour, and N. Ravindra, *Calculation of emissivity of Si wafers*, Journal of Electronic Materials **28** (12), 1385-1389 (1999).

[30] C. M. Herzinger, B. Johs, W. A. McGahan, J. A. Woollam, and W. Paulson, *Ellipsometric determination of optical constants for silicon and thermally grown silicon dioxide via a multi-sample, multi-wavelength, multi-angle investigation*, Journal of Applied Physics **83** (6), 3323-3336 (1998).

[31] G. E. Jellison Jr. and F. A. Modine, *Optical functions of silicon at elevated temperatures*, Journal of Applied Physics **76** (6), 3758-3761 (1994).

[32] P. Lautenschlager, M. Garriga, L. Vina, and M. Cardona, *Temperature dependence of the dielectric function and interband critical points in silicon*, Phys. Rev. B **36** (9), 4821–4830 (1987).

[33] W. C. Dash and R. Newman, *Intrinsic Optical Absorption in Single-Crystal Germanium and Silicon at 77°K and 300°K*, Phys. Rev. **99** (4), 1151–1155 (1955).

[34] H. R. Philipp and E. A. Taft, *Optical Constants of Silicon in the Region 1 to 10 ev*, Phys. Rev. **120** (1), 37–38 (1960).

[35] W. M. M. Kessels, *The influence of the substrate conditions on plasma beam deposited a-C:H-films*, MA thesis, Eindhoven University of Technology (1996).

[36] E. Bich, J. Millat, and E. Vogel, *The viscosity and thermal conductivity of pure monatomic gases from their normal boiling point up to 5000 K in the limit of zero density and at 0.101325 MPa*, Journal of Physical and Chemical Reference Data **19** (6), 1289-1305 (1990).

[37] CRC Handbook of Chemistry and Physics, http://www.hbcpnetbase.com/ (2013-2014).

[38] V. S. Bakardjieva, Z. I. Alexieva, G. D. Beshkov, and E. S. Mateev, *Plasma nitridation of silicon by N_2 and NH_3 in PECVD reactor*, Journal of Physics: Conference Series **223** (1), 012010 (2010).

[39] P. Morin, G. Raymond, D. Benoit, D. Guiheux, R. Pantel, F. Volpi, and M. Braccini, *Study of stress in tensile nitrogen-plasma-treated multilayer silicon nitride films*, Journal of Vacuum Science & Technology A: Vacuum, Surfaces, and Films **29** (4), 041513 (2011).

[40] S. E. Potts, *Private communication.*

[41] M. L. O'Neill, H. R. Bowen, A. Derecskei-Kovacs, K. S. Cuthill, B. Han, and M. Xiao, *Impact of Aminosilane Precursor Structure on Silicon Oxides by Atomic Layer Deposition*, The Electrochemical Society's Interface **20** (4), 33-37 (2011).

[42] Air Products, Material Safety Data Sheet 300000005202 4.0 (2010).

[43] S. Morishita, S. Sugahara, and M. Matsumura, *Atomic-layer chemical-vapor-deposition of silicon-nitride*, Applied Surface Science **112**, 198-204 (1997).

[44] W. Hansch, A. Nakajima, and S. Yokoyama, *Characterization of silicon/oxide/nitride layers by x-ray photoelectron spectroscopy*, Applied Physics Letters **75** (11), 1535-1537 (1999).

[45] A. Nakajima, T. Yoshimoto, T. Kidera, and S. Yokoyama, *Low-temperature formation of silicon nitride gate dielectrics by atomic-layer deposition*, Applied Physics Letters **79** (5), 665-667 (2001).

[46] A. Nakajima, Q. D. M. Khosru, T. Yoshimoto, T. Kidera, and S. Yokoyama, *NH_3-annealed atomic-layer-deposited silicon nitride as a high-k gate dielectric with high reliability*, Applied Physics Letters **80** (7), 1252-1254 (2002).

[47] H. Zhou, K. Elgaid, C. Wilkinson, and I. Thayne, *Low-Hydrogen-Content Silicon Nitride Deposited at Room Temperature by Inductively Coupled Plasma Deposition*, Japanese Journal of Applied Physics **45** (10B), 8388-8392 (2006).

[48] P. Violet, I. Nuta, C. Chatillon, and E. Blanquet, *Cracking study of pentakis(dimethylamino)tantalum vapors by Knudsen cell mass spectrometry*, Rapid Communications in Mass Spectrometry **24** (20), 2949–2956 (2010).

[49] L. McElwee-White, *Design of precursors for the CVD of inorganic thin films*, Dalton Transactions (45), 5327-5333 (2006).

[50] I. J. M. Erkens, A. J. M. Mackus, H. C. M. Knoops, P. Smits, T. H. M. van de Ven, F. Roozeboom, and W. M. M. Kessels, *Mass Spectrometry Study of the Temperature Dependence of Pt Film Growth by Atomic Layer Deposition*, ECS Journal of Solid State Science and Technology **1** (6), P255-P262 (2012).

[51] A. M. Wrobel, I. Blaszczyk, A. Walkiewicz-Pietrzykowska, A. Tracz, J. E. Klemberg-Sapieha, T. Aoki, and Y. Hatanaka, *Remote hydrogen-nitrogen plasma chemical vapor deposition from a tetramethyldisilazane source. Part 1. Mechanism of the process, structure and surface morphology of deposited amorphous hydrogenated silicon carbonitride films*, J. Mater. Chem. **13**, 731-737 (4 2003).

[52] B. Han, Q. Zhang, J. Wu, B. Han, E. J. Karwacki, A. Derecskei, M. Xiao, X. Lei, M. L. ONeill, and H. Cheng, *On the Mechanisms of SiO_2 Thin-Film Growth by the Full Atomic Layer Deposition Process Using Bis(t-butylamino)silane on the Hydroxylated SiO_2(001) Surface*, The Journal of Physical Chemistry C **116** (1), 947-952 (2012).

[53] K. A. Perrine and A. V. Teplyakov, *Reactivity of selectively terminated single crystal silicon surfaces*, Chem. Soc. Rev. **39**, 3256-3274 (8 2010).

[54] A. J. M. Mackus, S. B. S. Heil, E. Langereis, H. C. M. Knoops, M. C. M. van de Sanden, and W. M. M. Kessels, *Optical emission spectroscopy as a tool for studying, optimizing, and monitoring plasma-assisted atomic layer deposition processes*, Journal of Vacuum Science & Technology A: Vacuum, Surfaces, and Films **28** (1), 77-87 (2010).

[55] K. J. Clay, S. P. Speakman, G. A. J. Amaratunga, and S. R. P. Silva, *Characterization of a-C:H:N deposition from CH_4/N_2 rf plasmas using optical emission spectroscopy*, Journal of Applied Physics **79** (9), 7227-7233 (1996).

[56] S. Haukka and A. Root, *The reaction of hexamethyldisilazane and subsequent oxidation of trimethylsilyl groups on silica studied by solid-state NMR and FTIR*, The Journal of Physical Chemistry **98** (6), 1695-1703 (1994).

[57] S. Haukka, E.-L. Lakomaa, and T. Suntola, *Surface coverage of ALE precursors on oxides*, Applied Surface Science **82-83**, 548-552 (1994).